1-1-2013

Mechanics of Micro-Structured Soft Materials and Their Applications in Adhesion and Wetting

Chi-Mon Chen
University of Pennsylvania, chiche@seas.upenn.edu

Mechanics of Micro-Structured Soft Materials and Their Applications in Adhesion and Wetting

Abstract
Mechanical instability and large deformation are pervasive occurrences on stressed soft material surface patterns, which are normally detrimental to device performance. In this dissertation we show that these phenomena can be harnessed on structured polymeric thin films for surface patterning, strong dry adhesion and guided wettability. On dyed SU-8 photoresist films with graded depth-wise crosslinking density, we study the swelling-induced wrinkling. We demonstrate that isotropic surface wrinkles can be aligned with low aspect ratio 1-D channel-type pre-patterns. By varying the pitch and height ratios, defined as the pre-pattern pitch and height of the channels to the wrinkle wavelength and amplitude, respectively, we construct a morphological diagram of the confined wrinkles. For pitch ratios much larger than 1, the wrinkle morphology is predominantly isotropic. As pitch ratio decreases to ~ 1, the wrinkles arrange to out-of-phase 1-D bumps along the mountain regions of the channels. For pitch ratio much smaller than 1, the wrinkles evolve from in-phase perpendicular (to the channels) wrinkles, coexisting perpendicular wrinkles and localized patterns back to isotropic wrinkles in the order of decreasing height ratios.

In a separate material system, we utilize the buckling of high aspect ratio shape memory polymer (SMP) pillars to develop a strong interlocking dry adhesive. We engage the two identical pillar arrays together above the glass transition temperature of SMP (80 Â°C), where the SMP modulus drops by 3 orders of magnitude, leading to mutual buckling and deformation of the pillars when interlocked. Our finite element analysis and comparison of the calculated adhesion versus experimental data suggest that the adhesion force originates primarily from the pillar interweaving and secondarily from pillar indentation. The resultant pillar-to-pillar adhesion forces in normal (~ 54 N/cm^2) and shear (~ 72 N/cm^2) direction are found much larger than the pillar-to-flat (~ 12 N/cm^2 in normal and ~ 15 N/cm^2 in shear) and flat-to-flat contacts (~ 7 N/cm^2 in normal and ~ 16 N/cm^2 in shear). We further tune the adhesion anisotropy, designated by the ratio of shear to normal adhesion, by changing the pillar spacing. In spite of the strong adhesion, we show that the engaged adhesive can be easily separate on demand by heating to 80 Â°C.

Using similar SMP pillars, we design a reconfigurable surface to control surface wettability. Specifically, we report that the water droplets convert from low adhesion Cassie state on the original (or recovered) straight pillars to fully pinned Wenzel state on deformed pillars. Potentially, surface with both straight and deformed pillars can be utilized as a reprogrammable water collecting surface. Employing the deformed pillars, we present an advanced patterning method based on the deformed SMP pillars to transfer nanoparticle assemblies from donor substrates onto selected locations of pillars. Finally, we show a new approach to precisely control the tilting angle of the SMP pillars by coating the deformed pillars with a layer of metal, which hinders the full recovery of SMP pillars. On the composite surface, we observe strong anisotropic liquid spreading behavior, where the liquid propagates predominantly in the opposite direction of the pillar tilting.

Degree Type
Dissertation

Degree Name
Doctor of Philosophy (PhD)

MECHANICS OF MICRO-STRUCTURED SOFT MATERIALS AND THEIR APPLICATIONS IN ADHESION AND WETTING

Chi-Mon Chen

A DISSERTATION

in

Materials Science and Engineering

Presented to the Faculties of the University of Pennsylvania

in

Partial Fulfillment of the Requirements for the

Degree of Doctor of Philosophy

2013

Supervisor of Dissertation

_____

Shu Yang, Professor, Materials Science and Engineering

Graduate Group Chairperson

_____

Shu Yang, Professor, Materials Science and Engineering

Dissertation Committee

John L. Bassani, Professor, Mechanical Engineering and Applied Mechanics

Robert W. Carpick, Professor, Mechanical Engineering and Applied Mechanics

Anand Jagota, Professor, Chemical Engineering at Lehigh University

ACKNOWLEDGEMENT

Through the five year journey of my graduate study, I am so blessed to be surrounded by so many outstanding people without whom this dissertation cannot be presented. It is my great pleasure to acknowledge all of them.

The first person that I would like to express deepest appreciation to is definitely my thesis advisor, Professor Shu Yang. She has devoted tremendous amount of time to interact with us, improving our scientific reasoning, writing and presentation skills. Her mentorship, encouragement and creative thinking have been invaluable throughout my graduate career.

I am genuinely grateful for Professor John Bassani, Professor Robert Carpick and Professor Anand Jagota for being my committee members, monitoring my reports and thesis proposal and providing key advices and suggestions to my research. I would like to acknowledgement Professor Tao Xie at Zhejiang University for providing material formulations and characterizing important material properties that were being used repeatedly in my study. I also like to thank Professor Tobias Baumgart and his student Wan-Ting Hsieh (now at JHL Biotech, Inc.) and Professor Yaling Liu and his student Antony Thomas for offering exciting collaborative projects.

I appreciate Professor Zahra Fakhraai and her student Yi-Chih Lin in Department of Chemistry, Professor Daeyeon Lee and his student Iris Shangchun Yi in Department of Chemical and Biomolecular Engineering, Dr. Matthew Brukman, Iulian Codreanu (now at University of Delaware), Dr. Jamie Ford, Kyle Keenan, Dr. Alex Radin, Steve

Szewczyk, Hiromichi Yamamoto, and Dr. Douglas Yates for the training and helps on instrumentation and characterization.

I thank all the present and past Yang group members who have guided or assisted me for all of my research projects, including Dr. Dinesh Chandra, Elaine Lee, Jie Li, Dr. Yudi Rahmanwan, Gaoxiang Wu, Yu Xia, Dr. Yongan Xu, Dr. Xuelian Zhu, Chang-Lung Chiang, Xiao Ciao, Chien-Lin Lai, Issei Suzuki, Hunter van Adelsberg, Kelvin Wong, Chen Zheng, to name a few.

I would also like to express my gratitude toward Irene Clements, Raymond Hsiao, Fred Hellmig, Vicky Lee, Patricia Overend, and Enrique Vargas who have made my life in the Materials Science and Engineering department a colorful and enjoyable one. I am extremely lucky to have acquainted with Ying Bai at Lehigh University, Matthew Caporizzo, Dr. Tevis Jacobs, Dr. Rose Mutiso, Soong Ju Oh, Matthew Puster, Wei-Shao Tung, private cross-department study group members and many other friends with whom we have shared a great time.

Lastly, I would like to devote this thesis to my dear wife Yu-Fen Hsieh, my son Alvin Chen, my parents, my brother and all other family members, their happy smiles and everlasting love are the strongest propellant keeping me going forward.

ABSTRACT

MECHANICS OF MICRO-STRUCTURED SOFT MATERIALS AND THEIR APPLICATIONS IN ADHESION AND WETTING

Chi-Mon Chen

Shu Yang

Mechanical instability and large deformation are pervasive occurrences on stressed soft material surface patterns, which are normally detrimental to device performance. In this dissertation we show that these phenomena can be harnessed on structured polymeric thin films for surface patterning, strong dry adhesion and guided wettability. On dyed SU-8 photoresist films with graded depth-wise crosslinking density, we study the swelling-induced wrinkling. We demonstrate that isotropic surface wrinkles can be aligned with low aspect ratio 1-D channel-type pre-patterns. By varying the pitch and height ratios, defined as the pre-pattern pitch and height of the channels to the wrinkle wavelength and amplitude, respectively, we construct a morphological diagram of the confined wrinkles. For pitch ratios much larger than 1, the wrinkle morphology is predominantly isotropic. As pitch ratio decreases to ~ 1, the wrinkles arrange to out-of-phase 1-D bumps along the mountain regions of the channels. For pitch ratio much smaller than 1, the wrinkles evolve from in-phase perpendicular (to the channels) wrinkles, coexisting perpendicular wrinkles and localized patterns back to isotropic wrinkles in the order of decreasing height ratios.

In a separate material system, we utilize the buckling of high aspect ratio shape memory polymer (SMP) pillars to develop a strong interlocking dry adhesive. We engage

the two identical pillar arrays together above the glass transition temperature of SMP (80 °C), where the SMP modulus drops by 3 orders of magnitude, leading to mutual buckling and deformation of the pillars when interlocked. Our finite element analysis and comparison of the calculated adhesion versus experimental data suggest that the adhesion force originates primarily from the pillar interweaving and secondarily from pillar indentation. The resultant pillar-to-pillar adhesion forces in normal (~ 54 N/cm^2) and shear (~ 72 N/cm^2) direction are found much larger than the pillar-to-flat (~ 12 N/cm^2 in normal and ~ 15 N/cm^2 in shear) and flat-to-flat contacts (~ 7 N/cm^2 in normal and ~ 16 N/cm^2 in shear). We further tune the adhesion anisotropy, designated by the ratio of shear to normal adhesion, by changing the pillar spacing. In spite of the strong adhesion, we show that the engaged adhesive can be easily separate on demand by heating to 80 °C.

Using similar SMP pillars, we design a reconfigurable surface to control surface wettability. Specifically, we report that the water droplets convert from low adhesion Cassie state on the original (or recovered) straight pillars to fully pinned Wenzel state on deformed pillars. Potentially, surface with both straight and deformed pillars can be utilized as a reprogrammable water collecting surface. Employing the deformed pillars, we present an advanced patterning method based on the deformed SMP pillars to transfer nanoparticle assemblies from donor substrates onto selected locations of pillars. Finally, we show a new approach to precisely control the tilting angle of the SMP pillars by coating the deformed pillars with a layer of metal, which hinders the full recovery of SMP pillars. On the composite surface, we observe strong anisotropic liquid spreading behavior, where the liquid propagates predominantly in the opposite direction of the pillar tilting.

TABLE OF CONTENTS

LIST OF TABLES

LIST OF FIGURES

Chapter 1

Mechanical instability of soft materials for adhesion and wetting

1.1 Introduction

Mechanical instability has long been considered as undesirable phenomena in materials and device applications..[1] Nature, on the other hand, has demonstrated that mechanical instabilities play key roles in numerous biological and geological phenomena, including wrinkling of the skin[2, 3], regulating shapes of vital organs[4, 5], morphologies of leaves[6, 7], appearances on fruits[8, 9] and the formation of mountain ranges[10]. In the last decade, there have been increasing interests in controlling and harnessing the mechanical instabilities of soft materials, including wrinkling[3, 11, 12], creasing[13-18], delamination[19-23], folding[24, 25], pattern transformation[26, 27] and collapsing.[28-31] The intriguing surface patterns have led to discovery of novel mechanical behaviors for a wide range of potential applications, including flexible electronics[32-34], thin film metrologies[35-39], optical, photonic or phononic devices[40-46], microfluidic channels[19, 47-49], platform for cell studies[50-52] and auxetic materials.[53]

For thin film systems the mechanical instabilities can be categorized as: 1) Instabilities occur on the flat[3, 12] or curved surface[9] due to internal stress or mechanical stress from external stimuli above the critical threshold in the film. This type of instabilities causes undulations on the surface that is governed by the film properties, boundary conditions, and the stress states. Depending on the deformation characteristics, the instabilities are wrinkles with uniform dimensions or more localized ones such as

creasing, delamination, and folding. 2) Instabilities of surface patterns or structures, originating from the competition between the elasticity of the pattern with an external force. For a porous medium, the compressive external force can cause the pores buckled, triggering pattern transformation while the final morphology depends on the complexity of the original geometry. For surface patterns with a high aspect ratio (HAR) in which the height scale is greatly larger than the lateral dimension, buckling can be easily provoked by an external load owing to the high structural effective compliance. Such surface patterns are also susceptible to lateral collapse and ground collapse at small scale where the adhesion energy is able to overcome the bulk elastic properties.

Surface structures are also known to have deep impact on the adhesion properties and wettability. One of the most eminent examples is the gecko toe pad which consists of millions of HAR fibrillar setae made out of stiff β-keratin, allowing gecko to cling to almost any surface with ease. This ability is endowed by contact splitting,[29, 54, 55] dividing a single contact into multiple, hierarchical setae structure in the toe pad that is able to make conformal contact to the surface. In fact, this sort of split contact adhesion mechanism has been found in many kinds of insects, which helps them to survive in harsh environment around the world. The Sacred Lotus leaf is another clever example of nature utilizing surface structures. The delicate dual scale micro-/nano-structures offer the extraordinary water repellency that water droplet can easily roll away from the leaf. This rolling action of the droplet adheres to the pathogens and air-borne dusts and removes them on its path. Removal of these substances keeps the plant from infections and avoids dust isolation for effective photosynthesis. Most of the synthetic systems

mimicking such properties, however, often give in to robustness and are vulnerable to mechanical instabilities or large deformations.

In this chapter, we review the recent progress on the mechanical instabilities of polymer thin films and their implications in adhesion and wetting. We begin with the overview of mechanical instabilities on both featureless and patterned thin film in section 1.2 and 1.3, respectively. In the subsequent section 1.4, the adhesion and wettability of surface patterns and their challenges are discussed, focusing particularly on how mechanical instability affects these surface properties. We conclude this Chapter by providing a thesis outline in section 1.5.

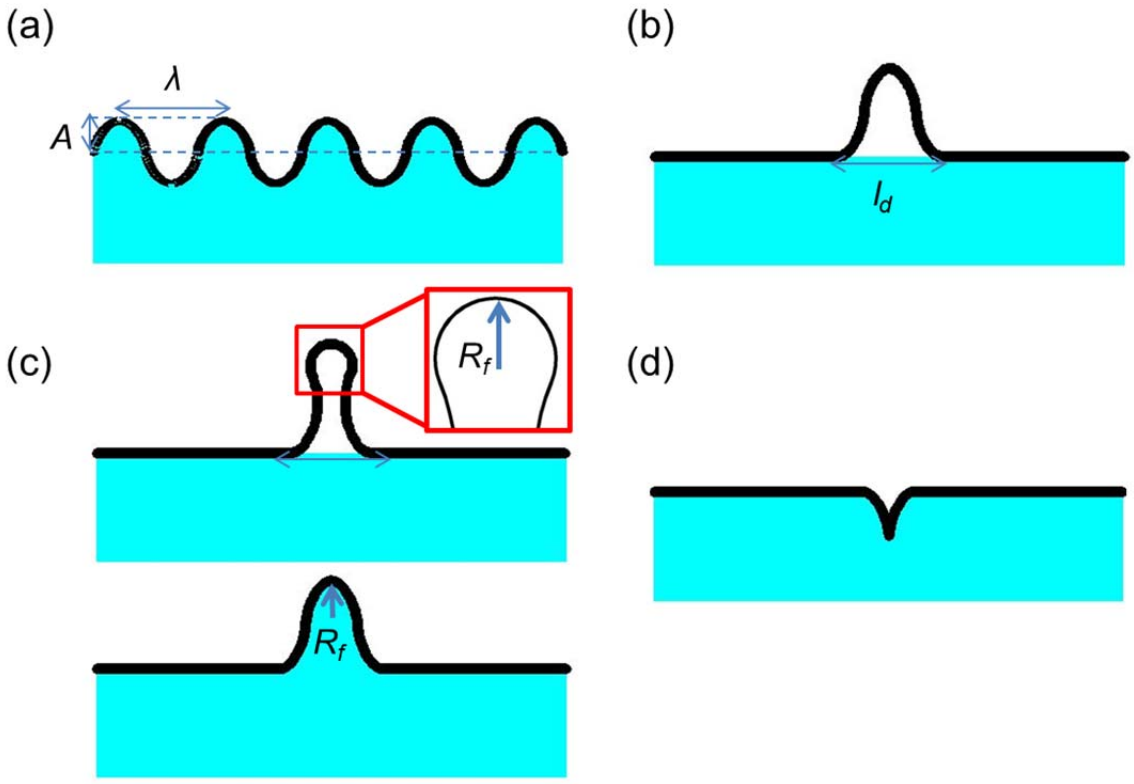

Figure 1.1 Mechanical instabilities on the featureless surface with characteristic length scales. (a) wrinkling; (b) delamination; (c) folding; (d) creasing.

1.2 Mechanical instabilities in featureless soft material films

A classic example of mechanical instability is the buckling of a slender beam subjecting to an axial load. When a beam is compressed by an axial load, it is in equilibrium state regardless of the magnitude of the load. But this equilibrium state can become unstable above a critical load leading to buckling failure. For a simply supported ideal beam, the lowest critical load (P_1) was first solved by Leonhard Euler mathematically dated back to 1744 as[56]

$$P_1 = \frac{\pi^2}{l^2} EI \tag{1.1}$$

where l is the total length of the beam, E is the elastic modulus, and I is the area moment of inertia of the cross-section of the beam. More generally, by neglecting the shear force caused by the axial load, the critical buckling load can be obtained by solving the eigenvalue problem of the fourth order ordinary differential equation or potential energy minimization for beam deflection with arbitrary, simple boundary conditions as[56]

$$P_{cr} = \frac{n\pi^2}{L^2} EI \tag{1.2}$$

here n is an integer, which is the order of the eigenvalue, equal to 1 for the lowest critical load. Note that Equation 1.2 has the same functional resemblance as Equation 1.1 but L here represents the "effective length" of the beam. This effective length is taken as the length between two inflection points of the deflected beam subjected to simple boundary conditions. At the inflection point, the moment equals to zero, which is exactly the same condition as the simply supported beam used to derive P_1 in equation 1.1.

In thin films systems, the buckling manifests itself as surface undulations. The types of the undulations can generally be classified as wrinkling, delamination, folding or creasing.) Ideally, Wrinkling results in homogeneous patterns while the later three are localized features (Figure 1).[14, 20, 24] In this section, we discuss the mechanistic aspect of the formation of these surface instability patterns and their practical applications.

1.2.1 Wrinkling

Surface wrinkling is a commonly observed phenomenon in our daily life, such as human skins,[2] dried fruits[8] and stretched plastic sheets.[3] Wrinkle in soft (composite) material is characterized by having a regular wavelength and amplitude which appear on stretched free-standing sheets,[3, 57] floating membranes,[58-60] confined gradient films subjected to external stimuli,[61, 62] strained elastic bilayers with[12, 63] or without a substrate[64, 65]. It can be initiated by mechanical compression,[66 67] thermal stress,[63, 68] osmotic pressure[48, 61] or capillary forces.[58-60] Cerda and Mahadevan derived the wavelength and amplitude for wrinkling on different medium by solving the geometrically nonlinear eigenvalue problem based on the total bending and elastic energy of the system which also satisfies the inextensibility of the compressed and buckle film.[3] For a thin film with length l and bending stiffness D, stretched by tension T with the resultant prestrain ε_L, the Poisson effect perpendicular to the stretching direction can buckle the film. The scaling law of wavelength λ (Figure 1.1a) is then[3]

$$\lambda \sim \left(\frac{D}{T}\right)^{1/4} l^{1/2} \tag{1.3}$$

and amplitude A can be expressed in terms of λ as

$$A \sim \varepsilon_L^{1/2} \lambda \tag{1.4}$$

For a film wrinkled on an elastic substrate, the strain energy comes from stretching the substrate with an effective substrate stiffness $K \sim T/l^2$. The wavelength is then[3]

$$\lambda \sim \left(\frac{D}{K} \right)^{1/4} \tag{1.5}$$

with the same expression for amplitude (Equation 1.4). Equations 1.4 and 1.5 predict that under the linear material response, the equilibrium wavelength of a bilayer system depends only on the material properties but the amplitude can be controlled by the applied strain, regardless of the stimuli. Using Föppl-von Karman plate theory, Huang *et al.* calculated the critical buckling threshold (in terms of membrane force), wavelength and amplitude in the thin or thick limit, showing the same trend that the as the amplitude continues to increase with compressive stress/strain, the wavelength remains constant.[69] Nevertheless, based on the material non-linearity of the hyperelastic substrate, Jiang and coworkers indicated that the wavelength is also dependent on the prestrain.[70]

The morphology of the wrinkle, on the other hand, is controlled by the type of stimuli[71], formation kinetics,[38, 63] stress state,[61, 72-74] surface defects[38, 75], free edges[76] or pre-patterns.[77-79] For swelling or thermally-induced wrinkles, the wrinkle morphology evolves with solvent diffusion or heat transfer which in turn determines the stress level and alters the intrinsic property of the material. For example, polymeric materials soften when temperature rise above the glass transition temperature (T_g).[38, 63] The stressed states in the thin films define the eigenmode of the wrinkles. Bumps or dimples generally form as the primary eigenmode while random or herringbone structure formed as a result of a

superposition of higher eigenmodes.[61, 69, 74] Ohzono *et al.* have also shown that an equilibrium wrinkle morphology can be reorganized by applying external loads.[72] Surface patterning is another effective way of tuning wrinkle morphology by introducing free edges that relax the stress perpendicular to it[12, 77] or providing guided pathways.[78, 80] The well-defined and readily controllable feature size and morphology make wrinkle an ideal candidate to generate regular patterns over a large area which has been applied to flexible electronics,[32, 33] thin film metrology[81], optical device,[40, 42, 82] adhesion[83-85] and wettability[47, 86] control.

1.2.2 Delamination

When a film on a substrate is loaded to a point which the interface can no longer withstand the stresses, the film detaches from the substrate, a characteristic of delamination. In the case of wrinkling, the surface undulation occurs when the film is fully attached to the substrate. At the critical threshold, delamination appears as localized blisters,[87] either strip-like[23] or circular shape[21, 88] depending on the applied force. Modeling the blister as a film buckled with both end fixed with lateral size l_d, Hutchinson and Suo have estimated the critical buckling threshold of the film, which is identical to Equation 1.2 with $L = l_d/2$ (Figure 1.1b).[87] For a circular blister, the buckling stress becomes[21]

$$\sigma_c = 1.2235 \frac{E_f}{1-\nu_f}\left(\frac{t_f}{R}\right)^{1/2} \tag{1.6}$$

where E_f, ν_f and t_f are the elastic modulus, Poisson's ratio and thickness of the delaminated film, respectively, and R is the radius of the blister. For a blister as an

incompressible strip on an elastic substrate subjected to uniaxial compression, Vella *et al.* have derived the scaling laws for the critical size l_d (Figure 1.1b) in the limits of a thin strip on a thin substrate and a wide strip on a thick substrate, respectively.[23] For the thin strip on a thin substrate, l_d is

$$l_d \sim \left(\frac{D^2 w}{E_s t_s \Gamma} \right)^{1/5} \tag{1.7}$$

where w is the width of the strip, Γ is the interfacial toughness, equal to the work of adhesion of the interface in the simplest case (Griffith's criterion)[89], E_s and t_s the elastic modulus and thickness of the substrate. For the wide strip on a thick substrate, l_d scales as

$$l_d \sim \left(\frac{D^2}{E_s \Gamma} \right)^{1/5} \tag{1.8}$$

When the stress level increases above the critical threshold, the cracks surrounding the blister grow further, deviating from a circular shape in the case of isotropic in-plane stress.[21, 90, 91] Hutchinson *et al.* show that in the initial stage of the crack growth, the blister remains nearly circular. As the stress further rises to a few times of the critical buckling stress, the crack growth is unstable to sustain length-wise perturbation, thus, growing to a telephone cord or a varicose structure depending on the Poisson's ratio of the film.[21, 91] Yu and Hutchinson pointed out that if a substrate is more compliant comparing to the film such as a metal layer on a polymeric substrate, where the critical buckling threshold can be significantly lower than predicted in Equation 1.6, a delamination pattern can have straight sides rather than undulating shapes.[92]

By directly patterning the surface with a low-adhesion layer, Moon *et al.* demonstrated that the telephone-cord like delamination patterns can be assembled into microfluidic channel or networks, where the wavy nature of the channels greatly promote chemical mixing.[49, 93] Edmondson *et al.* also showed that delamination can be harnessed to pattern the surface by providing preferential low-adhesion in polymer film on gold-coated silicon substrate.[19] Malachias *et al.* utilized similar concept to fabricate nano-channel network on etchant-sensitive sites in a semiconductor composite system.[94]

1.2.3 Folding

Folding is a localized bending state with large tip curvature that normally originates from later stage of delamination on an elastic foundation,[95, 96] and wrinkling of a film on liquid[24, 97] or on an elastic solid.[96, 98, 99] Pocivavsek *et al.* have investigated the wrinkling to folding transition for a plastic film on water. They find experimentally that the as the ratio of film displacement and wrinkle wavelength reaches above ~ 3, the wrinkle becomes unstable and energetically unfavorable.[24] The amplitude of the fold scales linearly with the displacement, in contrast to the wrinkle amplitude, which depends on the applied strain (Equation 1.4). This makes it possible for the fold to form directly in large size systems.[100] Based on scaling law, they approximate the size of the fold R_f (Figure 1.1c), defined as the radius of the maximum curvature, which is located at the fold tip, as[24]

$$R_f \sim \left(\frac{D}{K\Delta^2} \right)^{1/2} \tag{1.9}$$

where D and K are defined in Equation 1.5, Δ is the film displacement with respect to the compression. They also pointed out the fold localized from few of the existing wrinkles while other undulations decays as the displacement proceed further. This is not the case in a film on an elastic foundation, where the wrinkles few wavelength away does not decay.[98] With an elastic medium, the modulus mismatch between the film and substrate is greatly increased, resulting in more difficult a transition from wrinkle to fold and much slower or even no decay of the wrinkles after the formation of the fold.[24, 98] Brau *et al*. suggest that the fold forms progressively by multiplication of wrinkle wavelength which ends when self-contact occurs.[100]

For delamination-driven folding, Wagner *et al*. found R_f scales as

$$R_f \sim \left(\frac{D}{\Gamma}\right)^{1/2} \tag{1.10}$$

where D and Γ are defined in Equations 1.7 and 1.8. Comparing to Equation 1.9, it can be seen that the size of the fold is now controlled by the interfacial toughness rather than the substrate stiffness in the case without delamination.

1.2.4 Creasing

When an incompressible, hyperelastic solid is subjected to compressive forces above a critical threshold, the surface becomes susceptible to creasing, where the surface folds into the bulk to minimize the elastic energy (Figure 1.1d).[13, 15, 101, 102] Soft materials, either homogeneous or graded in depth-wise stiffness, such as rubber (or elastomer)[16, 102] and swollen hydrogel,[14, 103] which is normally considered incompressible, have been shown to form crease patterns. Biot predicted the critical strain for creasing in a

homogeneous solid as 46%.[104] However, experimentally the strain for creasing is substantially lower, ~ 35%.[102] Recently it has been pointed out that the critical strain Biot considered is an infinitesimal strain which is in fact an unstable wrinkling threshold[15, 16] that easily converts to crease in the presence of defects.[105, 106]

Typically, creases appear as slits or tri-wing shaped on the surface when the film is subjected to equi-biaxial stresses.[14, 103] Tallinen *et al*. have conducted a full scale finite element simulation and found that the slit-shape creases appear near the critical strain threshold while tri-wing shaped creases is stable high above the critical strain with hexagonal packing. The deep-fold morphology of the creases has been utilized by Kim and coworkers to reversibly display fluorescein-containing patterns in a thermally responsive poly(N-isopropylacrylamide-*co*-sodium acrylate) hydrogel film.[52] The creases were induced by pre-patterned steps underneath the hydrogel. Such responsive surface is also used to reversibly encapsulate polystyrene beads and cells on selective locations. A surface with coexisting wrinkle and crease has also been applied as a patterned substrate for polymeric solar cell.[43] The substrate with dual instabilities has the largest current density while the wrinkled substrate shows moderate enhancement. Particularly, the external quantum efficiency is greatly enhanced in the near infrared wavelength (~ 750 nm) on the substrate with dual instabilities owing to the resemblance of the slit shape of creases to the shape of nanowires.

1.3 Mechanical instabilities in patterned soft materials films

In section 1.2, we see that wrinkles and other type of instability patterns can be reorganized in the presence of defects/imperfections and surface patterns. In the case of

HAR patterns in which the pattern height or depth is comparable or larger than the lateral dimension, the surface pattern itself can be vulnerable to instabilities.

1.3.1 Collapse of compliant pillars

Hui *et al.* have derived the critical height h_c beyond which the weight of a column would exceed the critical buckling threshold[28]

$$h_c = \frac{7.837EI}{\rho g A} \tag{1.11}$$

where E is the elastic modulus of the column; I is the second moment of area; ρ is the density of column; g is gravitational acceleration; A is the area of the column cross section. For a cylindrical pillar with diameter d, Equation 1.11 can be re-arranged in terms of the critical aspect ratio AR_c as

$$AR_c = \left(\frac{h}{d}\right)_c = \left(\frac{0.49E}{\rho g d}\right)^{1/3} \tag{1.12}$$

For micro- or nano-scaled patterns, however, the large surface-to-volume ratio makes the surface adhesion force more dominant compared to the bulk elasticity or the gravitational body force. For soft materials, the high compliance requires less work for elastic deformation and let it easier to make conformal contact with other surfaces. Glassmaker *et al.* considered another failure mode owing to these two factors.[29] If the surface features are closely spaced, they may contact neighboring features laterally while subjecting to external mechanical disturbance. Assuming the deformation of the surface structures is purely elastic, the critical aspect ratio for cylindrical pillar below which such contact is reversible is given by[29]

$$AR_c = \frac{3^{1/4}\pi^{1/3}E^{1/3}s^{1/2}}{2^{17/12}W^{1/3}d^{1/6}\left(1-\upsilon^2\right)^{1/12}} \tag{1.13}$$

where s is the side-to-side spacing of the pillars; W is the work of adhesion of the pillar material; v is the Poisson's ratio of the material. For pillar arrays with a characteristic spacing, multiple pillars making contact under this mechanism leads to clumping into clusters with a size depending on the lattice type and pillar geometry.[107, 108 , 109] Similar phenomenon can be seen under the influence of capillary meniscus force.[44, 110, 111] Pokroy *et al.* show that by decreasing the bending stiffness of the pillars or increasing the capillary interaction, the pillars went from straight to clusters and finally to helical structure to maximized the adhesion contact.[111] Chandra *et al*. demonstrate that the clustering can induce color change to the surface structure due to Bragg diffraction.[44]

Besides making contact with neighbors, surface structures can also make contact with the ground, so called ground collapse. The critical aspect ratio for cylindrical pillars below which such ground collapse is recoverable is the again the balance of elastic energy and adhesion energy[31]

$$AR_c = \frac{\pi^{5/3}\left(1-\upsilon^2\right)^{-1/6}}{2^{11/3}3^{1/2}}\left(\frac{Ed}{W}\right)^{2/3} \tag{1.14}$$

While Equations 1.12 to 1.14 are all derived for cylindrical pillars, they can be readily adapted to other geometries. For example, for an array of long rectangular plates, the modulus E should be substituted by plane strain modulus $E/(1- v^2)$, and replacing d with lateral dimension of the plate (width) and the corresponding second moment of area.[28, 29, 31] To design surface structures, the geometry should be carefully selected to

enable or disable pattern collapsing according to these equations for desirable structure stabilities.

1.3.2 Ridge buckling of channels

Other than collapsing, compressive stress acting along the length of a rectangular plate or a thin wall confined on a rigid substrate can induce buckling.[112-115] Tirumala *et al.* have noticed the length-wise buckling behavior on swollen poly(N-isopropylacrylamide) (PNIPAAm) hydrogel with submicron patterns,[112] resembling the patterns appear on the edge growth of the long leaf[116] and plastically torn edges of polymer sheets.[6] Using simple scaling analysis by matching the bending energy and the compression energy of the swollen hydrogel plate with length l, they modeled the critical buckling strain ε_c as[113]

$$\varepsilon_c \sim \frac{w^2}{h^2} \tag{1.15}$$

where w is the width of the plate and h is the height, assuming $w < h < l$, and the buckling wavelength λ as

$$\lambda \sim \frac{h}{\sqrt{\varepsilon_c}} \tag{1.16}$$

Experimentally, the simple scaling laws (Equations 1.15 and 1.16) as found reasonably approximated the length-wise buckling even for aspect ratio (h/w) of 0.5, violating the assumption $w < h$. Tirumala *et al.* have also discovered that above a certain plate length l where the buckling can be observed, λ is insensitive to l. In the similar PNIPAAm hydrogel system but 2-3 orders of magnitude larger in length scale, DuPont

Jr. *et al.* reveal that for a fixed height, a local edge buckling state exists at low pattern aspect ratio which transforms to usual sinusoidal buckling pattern at larger aspect ratio (approximately $h/w > 1$ in the dry state) with larger wavelength.[115]

In a separate system, Yoon *et al.*[114] employed the expansion of deposited aluminum[117] onto the array of polymer plate to bring about spontaneous plate bending along the height and buckling along a length of the plate. The buckling behavior here is essentially the bilayer type, which can be described by equation 1.5.

1.3.3 Pattern transformation triggered by elastic instability

It is known that foam materials have very distinct mechanical properties, such as negative Poisson's ratio due to their interior porosity.[118, 119] Similar property also exists in two-dimensional (2D) porous membranes with periodic hole array, with or without attaching to a substrate, when undergoes a mechanical-instability triggered compaction process,[53, 120] referred as pattern transformation. It can be initiated by mechanical forces,[26, 121] osmotic pressure,[27, 46] and capillary force[122] for applications, including directed nanoparticle assembly,[27] tunable photonic[45] and phononic crystals,[46] color switch,[121] as well as auxetic materials.

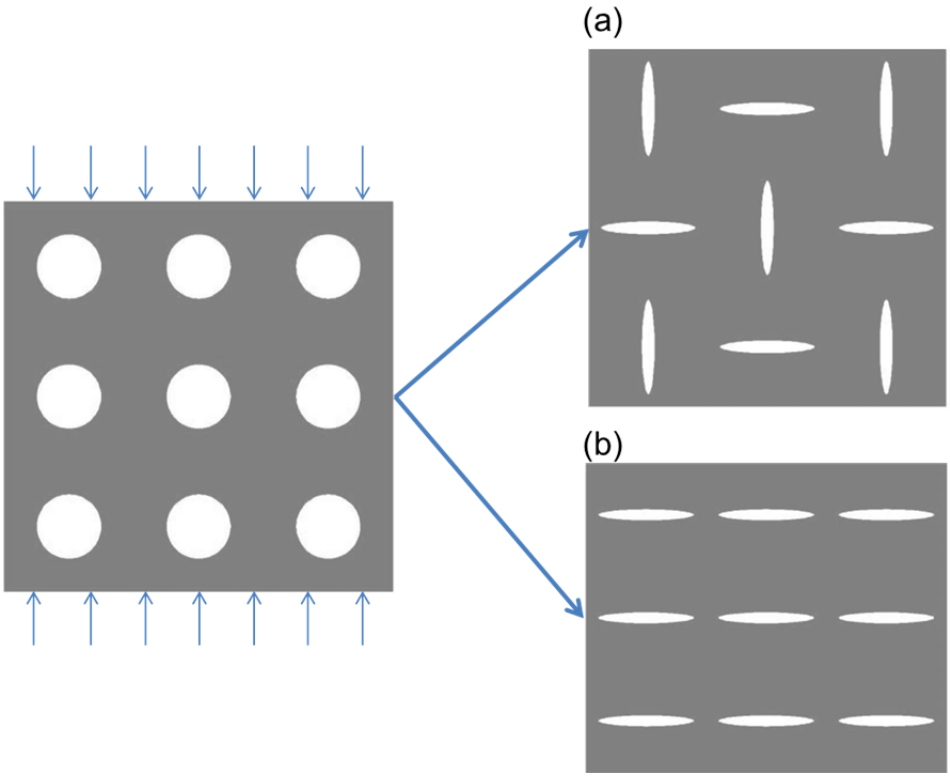

Figure 1.2 Pattern transformation of circular holes in square lattice induced by compression. (a) Transformed pattern for large areal hole fraction; (b) Transformed pattern for large areal hole fraction.

For a square lattice of circular holes on a soft membrane, the bifurcation takes place via large rotation of the joints connecting the neighboring holes, forming diamond plate-like structure (Figure 1.2a). by finite-element simulation Bertoldi *et al.* suggested that the bifurcation occurs when the porosity is greater than 34% while parallel slit-like (Figure 1.2b) collapsing happens below 34% porosity without bifurcation.[53] The onset of buckling and the mode of joint rotation are highly dependent on the lattice type, hole size and shape, porosity, and the aspect ratio and spacing. Mullin *et al.* have demonstrated that by changing the hole shape from circles to parallel ellipses, the resultant transformed patterns can be altered.[26] Zhang *et al.* also showed this tendency by stretching a soft

PDMS membrane with square lattice holes, where circular hole elongates, forming ellipses along the force direction.[27] Bertoldi and coworker studied the effect of hole shapes by perturbing the circular hole radius series to pores with four-fold symmetry, arranged in a square lattice. They discovered that this shape perturbation can lead to higher compaction ratio than circles, suggesting a path to optimal shape for auxetic materials.[123] They also investigated the pattern transformation on 3D spherical shell that results in encapsulation by void closure. This encapsulation behavior is controlled by shell thickness and void density which can induce as much as 54% volumetric compaction.[124] Kang *et al.* added another parameter by introducing inter-connected thin walls attached to a substrate, which controls the buckling modes in addition to joint rotation, leading to symmetry breaking.[125]

1.4 Adhesion and wettability of structured soft materials

As mentioned in section 1.1, the surface structures strongly affect its adhesion properties and wettability. In this section, we focus on this structural effect in soft materials, both biological and synthetic. We also discuss the underlying mechanisms, their applications and property variations under mechanical instability or large deformation.

1.4.1 Adhesion of biological structured soft materials

The exceptional climbing capability of gecko has provoked an intensive wave of research activities in recent decade trying to pinpoint its dry adhesion mechanism[29, 54, 55, 126-135] and to mimic its adhesion properties using synthetic systems.[108, 136-145] It has been shown that the gecko adhesion is based primarily on the van der Waals forces[127] and further enhanced by capillary effect.[128] These physical interactions provide the gecko

adhesion its reversibility, unlike conventional liquid-based or pressure sensitive adhesives whose integrity and strength for reapplication could dramatically decrease once separated.[146, 147]

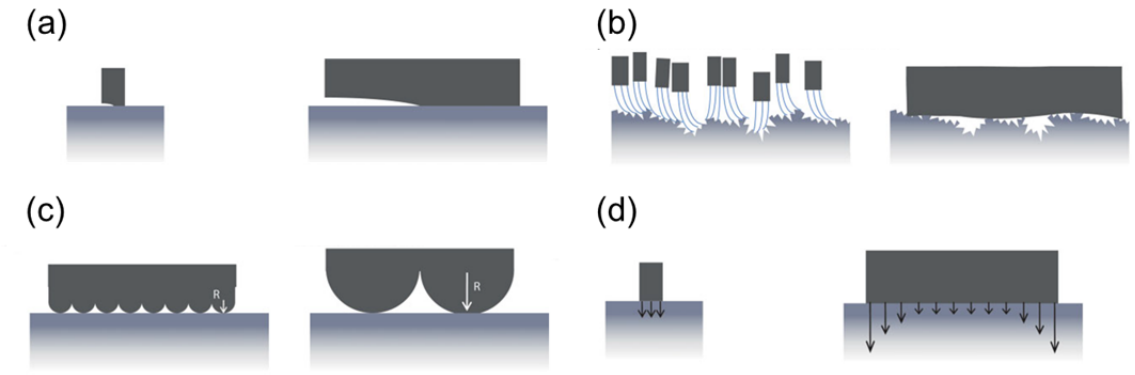

Figure 1.3 Schematics of contact splitting adhesion mechanisms in gecko or gecko-inspired structured surfaces: (a) Necessity of crack re-initiation and defect control; (b) Surface adaptability; (c) Increased surface-to-volume ratio; (d) Uniform stress distribution. The overall adhesion may be a combination of these mechanisms. (Adapted with permission from Kamperman *et al.*[148] Copyright 2010 Wiley-VCH Verlag GmbH & Co. KGaA, Weinheim)

Structurally, the gecko foot pad consists of a complex hierarchy with lamellae on the toe pad, array of setae (few tens to a hundred microns in length and few microns in diameter)[149], scales down to the nanofibrillar spatular tips (few microns in length and few hundreds nanometer in diameter)[149, 150]. Intuitively, splitting a flat pad into multiple contacts should decrease the adhesion due to the decrease in total area to make contact to the surface. In the contrary, it is found this natural design actually has multiple benefits. The adhesion mechanism is often referred as the "contact splitting" mechanism (Figure 1.3), as summarized by Kamperman and coworkers:[148] 1) Necessity of crack re-initiation and defect control. In the detachment event, a crack or defect driven separation needs to re-initiated for every contacting tip, limiting the crack propagation and defect size. 2)

Surface adaptability. The hierarchical HAR fibrillar structures considerably decrease the effective stiffness. Autumn *et al.*[151] have estimated that the effective stiffness of a setae array can decrease by more than 3 orders of magnitude from that of the bulk *β*-keratin. This makes the gecko foot pad much easier to make conformal contact even with a rough surface. 3) Increased surface-to-volume ratio. As the size of the contacting feature shrinks, its elastic energy associated with deformation decreases while the total surface area increases, minimizing the energy penalty to make contact. 4) Uniform stress distribution. Gao *et al*. show that because of the small size of the contacting tips the adhesion force is insensitive to the tip shape and the peeling force could be uniformly distributed at the time of pulling up, very different from a bulk adhesive.[132]

Arzt and coworkers also show that the dry adhesion of splitting contact can be enhanced based on a simple geometrical consideration.[55] For the contact between two spherical solids, Johnson *et al.* derived the pull-off force F needed to overcome the adhesion (referred as Johnson-Kendall-Roberts (JKR) model)[152]

$$F = \frac{3}{2}\pi W R \tag{1.17}$$

where W is the work of adhesion between the two solids, R is defined by the relative curvature as

$$\frac{1}{R} = \frac{1}{R_1} + \frac{1}{R_2} \tag{1.18}$$

where R_1 and R_2 are the radius for each sphere. For a flat substrate (as material 2), $R_2 \sim \infty$ and $R = R_1$.

If a contact is split to n individual contacts, whose size should scales accordingly as $R/\sqrt{n}$, then the pull-off force should be

$$F_n = n \times \frac{3}{2}\pi W \frac{R}{\sqrt{n}} = \sqrt{n}F \tag{1.19}$$

From Equation 1.19, it is clear that from a geometrical consideration, assuming an ideal case where all the contacts are separated at the same time, the adhesion force should be magnified by the square root of the total number of contact points.[55] In fact, this contact splitting mechanism works in many other biological species as well, such as lizards,[134] beetles, flies and spiders,[55] where similar structures can be found on the adhesives pads.

Another important property of gecko adhesion is the shear-activated adhesion force. It is revealed that a high adhesion force is only available by shearing the structure after engagement.[126, 134, 135] Theoretically, Tian *et al.*[135] show that adhesion force increases with the decrease of angle between the setae shaft and the substrate, which is caused by the rolling movement of the gecko toe during attachment.

Based on the principles of gecko adhesion, there have been extensive efforts to create synthetic dry adhesives. The simplest type among them is the single-level polymer pillar[108, 137] and nanotube array.[139, 141] Greiner *et al.*[108] studied the variation of adhesion (or pull-off force) against a spherical indenter with polydimethylsiloxane (PDMS) pillar arrays in a hexagonal or square lattice with different geometric parameters, including radius and aspect ratio. It is found that the pull-off force increases with higher preload initially and quickly reaches a plateau and the pull-off strength (pull-off force divided by

apparent contact area) increases with decreasing pattern radius and increasing aspect ratio, although the later would be limited by pattern collapse mentioned in section 1.3. One possible solution is to introduce a covering film on top of the HAR pillars, Glassmaker *et al.*[138] have shown that such covered HAR pillars are free from collapsing and the adhesion force is amplified by as many as 9 times comparing to a flat film by crack-trapping mechanism with larger contact area and high compliance from the HAR structures.

To mimic the hierarchical structures in gecko foot hairs, a few groups have also fabricated multi-level HAR structures. Northen *et al.*[136] fabricate two-level structures from polymer nanorods on nickel cantilevers. When aligned parallel the surfaces, the nickel cantilevers allow the polymer nanorods to contact the surface with noticeable adhesion force. In the presence of a magnetic field, the cantilevers are twisted away from the contact surfaces, resulting in adhesion lost. With the magnetic field actuation, the adhesion can be tuned by ~ 40 times (from 14 Pa to 0.37 Pa with and without magnetic field). In a separate vein, Murphy *et al.*[136] have fabricated two- to three-level polyurethane tilted pillar structures (300 μm, 50 μm and 3 μm in pillar diameter for the first, second and third level, respectively),[145] They show that the two-level systems have an ~ 30% increase in maximum adhesion to ~ 600 mN against a 12 mm diameter glass indenter comparing to the single layer adhesive. The three-level structures, however, suffer from structural collapsing under the load. Therefore, the adhesion strength could not be measured. Jeong and coworkers compared the shear adhesion of single or double level, titlted polyurethane acrylate (PUA) pillars where the single level pillars are comparable to the size of gecko spatula (pillar diameter is ~ 400 nm for the single level

pillar array and ~ 5 μm and ~ 400 nm for the first and second level of the double level pillar array). They found that although the single level system has a larger adhesion force against a flat substrate because of the larger total contact area (~ 21 N/cm^2 for single level and ~ 9 N/cm^2 for double level), the double level pillar array has much better tolerance to surface roughness. Experimentally, the adhesion force of the single level pillars decrease rapidly from ~ 20 N/cm^2 to < 5 N/cm^2 as the roughness scale increases from 0 to 10 μm while the adhesion only lessens from ~ 9 N/cm^2 to ~ 7 N/cm^2 for the double level pillars.[153]

Structural collapse has being known to devastate the adhesion of gecko-mimicking HAR pillars[108] or nanotubes due to reduction of contact area.[154] For other type of mechanical instability, Jagota[155] and Hui[156] have pointed out that the buckling of HAR pillars during contact can greatly enhance the effective compliance of the adhesive. The buckled pillars would have nearly no additional resistance to the external force, transferring the load to unbuckled pillars and making them much easier to accommodate rough surfaces.[155] However, they also show experimentally that the buckled plate-like pillars can result in losing contact which takes toll on the total adhesion force although this trend is contact geometry dependent.[29]

So far the study of structural adhesion has mostly focused on the interaction between a patterned surface to another flat surface. In natural environment, however, a rough or patterned surface is frequently encountered such as a leaf for insects to walk on.[157] We mentioned briefly in the above section how gecko can adapt to a rough surface by its high effective compliances. Therefore, adhesion involves the interaction between two features. In fact, for features at similar lengthscale, nature has already demonstrated fascinating

examples utilizing the mechanical interlocking to achieve strong adhesion. Burdock or cleaver seeds have pronounced hooks that are able to attach to the fabrics or furs of the animal for reproduction and dispersal purposes.[158] Diatoms also devise sophisticate silica wall to protect themselves from mechanical damage but preserve the cell division capability at the same time.[159] In a recent review, Gorb[160] summarized the common attachment devices utilized by biological systems, the operating functions, time scales and the corresponding physical interactions. He categorized attaching principles for the biological organisms as mechanical interlocking (hook, lock-and-key, clamp, etc.), suction, friction and adhesion (including wet and dry adhesion).[160] Here, mechanical forces and friction between structures are the primary contributions to the adhesion forces.

In addition to biological systems, synthetic adhesives also employ mechanical interlocking and friction for feature-to-feature adhesion. One of the long-standing examples of mechanical interlocking is the interaction between the metal-plastic composite in the industry. Normally the plastic or metal surface is chemically pre-treated to generate surface structures, taking the advantage of the synergic effect of mechanical interlocking, increase in surface area or even chemical bonding to facilitate subsequent metal plating or plastic lamination.[161] More recently, HAR surface structures, such as nanowire arrays[162] and polymer pillars[163] have been used as interlocking fasteners by pressing two surface structures against each other. Such structures have a highly anisotropic adhesion: it is strong in the shearing direction but can be easily separated by peeling in the normal direction. This property can be attributed to the lack of mechanical interlocking in the normal direction and the structure alignment induced increase of

surface contact in the shear direction. The total adhesion force is a combination of the friction originated from the van der Waals force[163] and mechanical force required to bend or even break the posts.[162] This adhesion anisotropy, however, may limit the application of this type of adhesives considering the complex stress state of a practical adhesive joint acting in multiple directions.[164] For more sophisticate structures such as posts with spherical or cap head shapes or hooks and loops (Velcro®), Williams *et al.*[165] have evaluated the detachment mechanism and concluded that the process involves the deflection, rotation or withdrawal of the whole structure to overcome the friction or interlocking constraints.

Gorb *et al.*[166] have also investigated friction-based normal adhesion of surface patterns consisting of regular array of sharp parabolic features. The adhesion force is only activated above a threshold preload, which matches well with their theoretical model. The adhesion force, however, is only a fraction of the preload. McMeeking *et al.*[167] have theoretically calculated the adhesion force between two dense pillar arrays and predicted that the adhesion force should be able to reach 30% of the tensile stress of the material. Practically, however, a large preload is required to generate significant adhesion, provided that such attachment can be successfully made, which is questionable especially when the pillars are densely packed. Further, HAR structures, which are commonly used in feature-to-feature contact, are susceptible to mechanical instability, thus, reducing pillar-pillar overlap length (defined as the insertion distance of one pillar relative to others on the countersurface) and adhesion strength.[168] For the friction based system, the friction-induced buckling can happened at intermediate overlap length, where the adhesion would be lost due to pillar failure.[167]

1.4.2 Wettability of structured soft materials

The sacred lotus leaf is known to possess excellent water repellency with water contact angle 150^{o} or greater with very small contact angle hysteresis (< 10°).[169]. Such surface is often referred as superhydrophobic and self-cleaning since the enrolling water droplet can remove any hydrophilic contaminants on the surface due to the reduced contact area and the large adhesion between water and contaminants. Water strider has the capability of keeping itself afloat and moving rapidly on the water surface due to the superhydrophobic legs.[170, 171] Namib desert beetles, on the other hand, harvest dew water from patched hydrophilic regions on top the hydrophobic hemispheres presented on their scales.[172] All these examples from nature utilize wettability for water management.

For a liquid droplet sitting on a flat surface, the equilibrium shape of the droplet is determined by the interfacial tensions at the solid-liquid-air interface. Thomas Young derived a force-balance equation to determine the equilibrium contact angle θ (or Young's contact angle) of a droplet on a homogeneous rigid surface, known as Young's equation[173, 174]

$$\cos\theta_E = \frac{\gamma_{SG} - \gamma_{SL}}{\gamma_{LG}} \tag{1.20}$$

where γ_{LG} is the interfacial energy of liquid-gas, γ_{SG} is the interfacial energy of solid-gas, and γ_{SL} is the interfacial energy of solid-liquid. A surface is considered hydrophilic if θ_E < 90º and hydrophobic if θ_E > 90º. Liquid can completely wet (θ_E = 0º) on a surface with strong chemical affinity or a surface with high surface energy, for example, a pure and clean metal surface.[175] However, on a flat homogeneous surface, the highest equilibrium

contact angle can be achieved is 120º.[174, 176] To achieve a higher apparent water contact angle, surface roughness needs to be introduced.

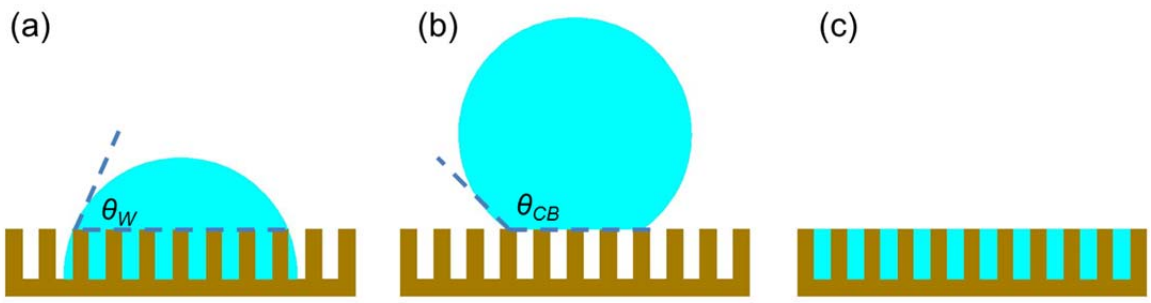

Figure 1.4 Wetting states (a) Wenzel state; (b) Cassie-Baxter state; (c) Hemi-wicking.

The effect of surface roughness was first discussed by Wenzel in 1936.[177] He considered that the roughness would increase the interfacial energy gain on the solid-liquid interface while promoting the interfacial energy lost on the solid-gas interface. On a hydrophilic material with θ_E < 90º, or $\gamma_{SG} > \gamma_{SL}$, the apparent contact angle should decrease with the increase of roughness, whereas the apparent contact angle on a rough and hydrophobic surface should increase. Wenzel defined a surface roughness ratio r as the ratio of apparent solid-liquid contact area to the projected area. the apparent contact angle in Wenzel model (θ_W) thus becomes (Figure 1.4a)[177]

$$\cos\theta_W = r\cos\theta_E \qquad (1.21)$$

Wenzel model was later extended to porous, chemically heterogeneous medium by Cassie and Baxter, considering the droplet as sitting on a composite surface.[178] If the fraction of the total surface area of each surface portion (with equilibrium contact angle

θ_{En}) to the total projected area is denoted as f_n, the apparent contact angle in Cassie-Baxter model (θ_{CB}, Figure 1.4b) is then[178, 179]

$$\cos\theta_{CB} = \sum_n f_n \cos\theta_{En} \tag{1.22}$$

For a binary system consisting of solid (f_1, θ_{E1}) and air (f_2, θ_{E2}), where θ_{E2}=180º. The contact angle is simplified as[178]

$$\cos\theta_{CB} = f_1 \cos\theta_{E1} - f_2 \tag{1.23}$$

Assuming that the solid-liquid and liquid-air interface are coplanar (when the scale of surface structure is much smaller than the droplet size), Equation 1.23 can be further simplified to

$$\cos\theta_{CB} = f_1 \cos\theta_{E1} + f_1 - 1 \tag{1.24}$$

for a structured surfaces with trapped air pockets.

With these two basic models, a question arises as to which models a water droplet should obey when it is deposited on a structured surface? While liquid can completely spread on a hydrophilic and rough surface as Wenzel model predicts, [180] it cannot completely penetrate the grooves of a rough, hydrophobic surface (θ_E > 90º) since it is energetically unfavorable since $\gamma_{SG} < \gamma_{SL}$. On a surface of moderate hydrophobicity ($90^o < \theta_E < \theta_c$), where θ_c is the threshold equilibrium contact angle, defined as,[181]

$$\cos\theta_c = \frac{f_1 - 1}{r - f_1} \tag{1.25}$$

or equivalently, on a surface of moderate roughness, Cassie-Baxter state and Wenzel state may coexist, and a metastable Cassie-Baxter non-wetting state can be transformed into a stable Wenzel wetting state, that is a wetted contact is favored and liquid fills the grooves of the rough surface only below the droplet. If $\theta_E > \theta_c$, Cassie state should be energetically favorable while Wenzel state is stable for $\theta_E < \theta_c$.

For a hydrophilic rough surface, $0 < \theta_E < \theta_c < 90^o$, Hemi-wicking (Figure 1.4c) should occur, a partial wetting state between spreading and imbibition,[181] where θ_c is

$$\cos\theta_c = \frac{1 - f_1}{r - f_1} \tag{1.26}$$

In this case, the top of the surface structures remain dry while the imbibition font progresses. Here, Cassie state can explain the wetting behavior at a sufficiently small equilibrium contact angle with the consideration of imbibition, avoiding the limitation of Wenzel model which predicts unreasonable roughness-induced complete wetting as soon as $\cos\theta_W = -1$.[174]

While the above models express the static droplet contact angle on a topographic surface, they do not provide information of the dynamic wetting behaviors. By adding more liquid to an existing droplet on the surface, the contact angle can be pinned until a certain point which the triple phase line (the contact line resides on the interface of solid, liquid and gas phases) starts to advance. This angle is called advancing contact angle θ_A. Similarly, withdrawing a droplet to a point when the triple phase line starts to retract, the contact angle is called receding contact angle θ_R.[174] The difference between θ_A and θ_R is

called the contact angle hysteresis $\Delta\theta$. Another parameter to characterize the hysteresis of droplet is the sliding angle α at which the droplet begins to roll off the surface [182]

$$\sin\alpha = \frac{2R\gamma_{LG}\left(\cos\theta_R - \cos\theta_A\right)}{\rho g V} \tag{1.27}$$

where R is the contact radius of the droplet; ρ is the liquid density; g is the gravitational acceleration, V the droplet volume. A general form of α can be obtained from the balance of droplet retention force and gravitational force for different droplet shape as[183-186]

$$\sin\alpha = \frac{2L_D k}{\rho g V} \tag{1.28}$$

where L_D is a shape dependent primary length scale of the droplet contour,[184] k is a model dependent constant.[185]

The droplet in the Cassie-Baxter state is characterized by a significantly smaller $\Delta\theta$ or α compared to that in the Wenzel state. This is owing to the composite nature of the Cassie state, where the solid fraction in the non-wetting Cassie-Baxter state is much smaller than the wetting Wenzel state, thus lowering the solid-liquid adhesion.[176] This makes Cassie state a highly desirable state to achieve superhydrophobicity ($\theta > 150°$ and $\Delta\theta$ or $\alpha < 10°$)[187-190] or highly oleophobic surfaces[191-196] by fine-tuning surface topography, including HAR posts or pillars,[176, 197] dual- and multi-scaled roughness[187, 194, 198] and re-entrant or overhang surfaces.[195, 196]

We have already mentioned earlier that wicking or imbibition can occur on a hydrophilic rough surface.[181] On cylindrical post arrays, Courbin *et al.* have shown that the final liquid spreading shape is controlled by the liquid type, which determines θ_E, and

lattice symmetry and inter-posts spacing, which determine the velocity of propagating liquid front in the structure.[199] Obara *et al.* have suggested the sharpness of pillar patterns can also affect the imbibition dynamics of the liquid.[200] Extrand *et al.* have shown that the total wetted area of square posts is controlled by pillar side width, post height and tapering angle of posts.[201] Jokinen *et al.*[202] and Vrancken *et al.*[203] further report that the shape of individual pillars can be used to control the liquid propagating direction and shape.

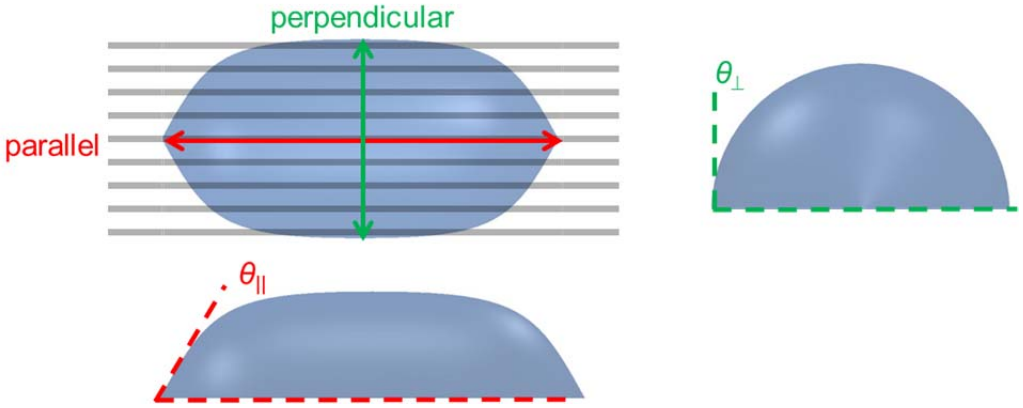

Figure 1.5 An anisotropic droplet on channel structures. The contact angle $\theta_{||}$ is measured along the channel direction and $\theta_{\perp}$ is measured perpendicular to the channel.

Another type of features is 1-D lattice or asymmetrical patterns, leading to anisotropic wetting. [204-206] For example, it is revealed that the stripe-like and scale-like structures on the superhydrophobic butterfly wing, allowing for droplet sliding only in the outward direction of the wing rather than inward, providing a self-cleaning mechanism.[207] The specially arranged relieves on the rice leaf showing 1-D order along the longitudinal direction of the leaf but randomly along the transverse direction, providing a lower longitudinal sliding angle than the transverse one.[187] the droplet on the

goose leaf with fan-shaped pattern is asymmetric with only one mirror plane along the middle axis of the pattern.[208]

Anisotropic wetting on structured surfaces can be classified as static characteristics, including anisotropic droplet shape,[208, 209] contact angle[86, 210] and morphology,[47, 211, 212] and dynamic characteristics, including directional spreading,[213-215] imbibition,[202, 216] anisotropic droplet sliding angle[187, 207, 217] and impact behavior.[218] In synthetic systems, a regular 1-D channel-like structure often results in an anisotropic droplet shape, spreading in the direction parallel to the channel/line (Figure 1.5).[86, 209, 210, 212] Such droplet has two distinct contact angles, $\theta_{||}$ which is measured in parallel to the 1-D structure and $\theta_{\perp}$ which is measured perpendicularly to the 1-D structure, normally $\theta_{||} > \theta_{\perp}$. This morphology is caused by the pinning of the triple phase line along the mountain region of the channel with a higher energy barrier while liquid can freely propagate parallel to the channel.[210] The anisotropy is largest on a slightly hydrophilic/oleophilic surface. A highly hydrophobic/oleophobic surface will have triple phase line pinning while a highly hydrophilic/oleophilic surface will have liquid imbibition or complete spreading.[212] Seemann *et al.* have explicitly examined the effect of both surface chemistry (intrinsic contact angle θ_E) and topography (channel aspect ratio *AR*, defined as channel height to channel width). They find that as θ_E increases, the liquid morphology obtained in the channel primarily changes from wedges (liquid on the channel corners), filaments (liquid in the channel) to droplets. Depending on the *AR*, composite morphology which is coexistence of droplet and wedge at low AR or filament and wedge at high AR can also be observed on hydrophilic surface for $\theta_E < 45°$. Chung *et al.* show that on UV/Ozone-oxidized PDMS wrinkles, the water contact angle can be changed in real time, while the

anisotropy is controlled by the wrinkle aspect ratio (amplitude to wavelength); the larger the amplitude, the higher the contact angle anisotropy.[86] Using UVO-treated PDMS as a dynamically tunable platform, Khare *et al.* show that a glycerin droplet go from isotropic, anisotropic, finally to imbibition above a compressive strain threshold, depending on the wrinkle amplitude.[47]

Anisotropic wetting behavior is also observed on the deformed regular 2-D patterns. On deformed HAR polymer pillars,. Kim *et al.* show that the droplet propagates along the pillar bending direction due to the droplet retention force which points toward the pillar bending direction.[213] by careful selection of the θ_E and control of the bending angle of the HAR pillar arrays, Chu *et al*. tune the liquid spreading behavior from no spreading to uni-directional spreading or bi-directional spreading.[214]

1.5 Thesis outline

This thesis considers the interplay of mechanical instabilities and large deformation in various structured polymeric materials, and exploits their applications in surface patterning, adhesion and wetting. Specifically, we investigate how wrinkling can be utilized to generate regular patterns in a newly designed gradient photo-polymer system. In turn, we look into how to use photo-patterning to regulate the formation of wrinkles and the commensurate of the lengthscales. In a separate system, we investigate the interactions between two HAR shape memory polymer (SMP) pillar arrays. In particular, we utilize the pillar buckling and collapse, generally detrimental to adhesive, to design a strong dry adhesive system via mechanical interlocking. In the same system, we fine-tune the deformation and shape recovery to study the anisotropy of water contact angles and

sliding angles, as an example of reconfigurable surface for liquid manipulation. The subsequent chapters in this dissertation are organized as:

In Chapter 2, we develop a dyed SU-8 photoresist thin film on the glass substrate with a depth-wise crosslinking gradient to induce the formation of surface wrinkles with controlled wavelength and morphology. We then pre-pattern the photoresist film by capillarity force lithography and systematically study the effect of pre-patterns size on wrinkle morphology.

In Chapter 3, we design a new adhesive system based on the buckling and interlocking of thermally-activated SMP pillars to achieve strong dry adhesion force. We investigate the interactions between two pillar arrays and the mechanistic origin of the adhesion. We also show that by changing the pillar pitch or varying the operational temperature, the adhesion force can be tuned.

In Chapter 4, we extend the study of SMP pillar array to vary the surface wettability. We carefully select the pillar geometry to refine the shape recovery capability. The static surface wettability can be greatly altered by deforming/recovering the pillars. We also utilize pillar deformation as an advanced patterning method by picking up nanoparticle assembly. We further control the deformation angle of pillar and achieve anisotropic wettability.

The dissertation is summarized in Chapter 5, where the outlook and extensions of the current work are discussed.

1.6 References

1. J. M. Gere, *Mechanics of materials*, 6th edn., Brooks/Cole, Pacific Grove, Calif. ; London, 2004.
2. K. Kareklas, D. Nettle and T. V. Smulders, *Biol. Lett.*, 2013, **9**, 20120999.
3. E. Cerda and L. Mahadevan, *Phys. Rev. Lett.*, 2003, **90**, 074302.
4. B. Li, Y. P. Cao, X. Q. Feng and H. J. Gao, *J. Mech. Phys. Solids*, 2011, **59**, 758-774.
5. T. Savin, N. A. Kurpios, A. E. Shyer, P. Florescu, H. Y. Liang, L. Mahadevan and C. J. Tabin, *Nature*, 2011, **476**, 57-62.
6. H. Y. Liang and L. Mahadevan, *Proc. Natl. Acad. Sci. U. S. A.*, 2009, **106**, 22049-22054.
7. V. Mirabet, P. Das, A. Boudaoud and O. Hamant, in *Annual Review of Plant Biology, Vol 62*, eds. S. S. Merchant, W. R. Briggs and D. Ort, Annual Reviews, Palo Alto, 2011, vol. 62, pp. 365-385.
8. J. Yin, Z. X. Cao, C. R. Li, I. Sheinman and X. Chen, *Proc. Natl. Acad. Sci. U. S. A.*, 2008, **105**, 19132-19135.
9. X. Chen and J. Yin, *Soft Matter*, 2010, **6**, 5667-5680.
10. K. F. Haven, *Wonders of the land : merging earth myth with earth science*, Libraries Unlimited, Westport, Conn., 2006.
11. J. Genzer and J. Groenewold, *Soft Matter*, 2006, **2**, 310-323.
12. N. Bowden, S. Brittain, A. G. Evans, J. W. Hutchinson and G. M. Whitesides, *Nature*, 1998, **393**, 146-149.

13. T. Tanaka, S. T. Sun, Y. Hirokawa, S. Katayama, J. Kucera, Y. Hirose and T. Amiya, *Nature*, 1987, **325**, 796-798.

14. V. Trujillo, J. Kim and R. C. Hayward, *Soft Matter*, 2008, **4**, 564-569.

15. W. Hong, X. H. Zhao and Z. G. Suo, *Appl. Phys. Lett.*, 2009, **95**, 111901.

16. E. Hohlfeld and L. Mahadevan, *Phys. Rev. Lett.*, 2011, **106**, 105702.

17. P. M. Reis, F. Corson, A. Boudaoud and B. Roman, *Phys. Rev. Lett.*, 2009, **103**, 045501.

18. P. Kim, M. Abkarian and H. A. Stone, *Nat. Mater.*, 2011, **10**, 952-957.

19. S. Edmondson, K. Frieda, J. E. Comrie, P. R. Onck and W. T. S. Huck, *Adv. Mater.*, 2006, **18**, 724-728.

20. H. X. Mei, R. Huang, J. Y. Chung, C. M. Stafford and H. H. Yu, *Appl. Phys. Lett.*, 2007, **90**, 151902.

21. J. W. Hutchinson, M. D. Thouless and E. G. Liniger, *Acta Metall. Mater.*, 1992, **40**, 295-308.

22. G. Gioia and M. Ortiz, in *Advances in Applied Mechanics, Vol 33*, Academic Press Inc, San Diego, 1997, vol. 33, pp. 119-192.

23. D. Vella, J. Bico, A. Boudaoud, B. Roman and P. M. Reis, *Proc. Natl. Acad. Sci. U. S. A.*, 2009, **106**, 10901-10906.

24. L. Pocivavsek, R. Dellsy, A. Kern, S. Johnson, B. H. Lin, K. Y. C. Lee and E. Cerda, *Science*, 2008, **320**, 912-916.

25. H. Diamant and T. A. Witten, *Phys. Rev. Lett.*, 2011, **107**, 164302.

26. T. Mullin, S. Deschanel, K. Bertoldi and M. C. Boyce, *Phys. Rev. Lett.*, 2007, **99**, 084301.

27. Y. Zhang, E. A. Matsumoto, A. Peter, P. C. Lin, R. D. Kamien and S. Yang, *Nano Lett.*, 2008, **8**, 1192-1196.

28. C. Y. Hui, A. Jagota, Y. Y. Lin and E. J. Kramer, *Langmuir*, 2002, **18**, 1394-1407.

29. N. J. Glassmaker, A. Jagota, C. Y. Hui and J. Kim, *J. R. Soc. Interface*, 2004, **1**, 23-33.

30. D. Chandra and S. Yang, *Acc. Chem. Res.*, 2010, **43**, 1080-1091.

31. P. Roca-Cusachs, F. Rico, E. Martinez, J. Toset, R. Farre and D. Navajas, *Langmuir*, 2005, **21**, 5542-5548.

32. D. Y. Khang, H. Q. Jiang, Y. Huang and J. A. Rogers, *Science*, 2006, **311**, 208-212.

33. D. H. Kim, J. H. Ahn, W. M. Choi, H. S. Kim, T. H. Kim, J. Z. Song, Y. G. Y. Huang, Z. J. Liu, C. Lu and J. A. Rogers, *Science*, 2008, **320**, 507-511.

34. H. C. Ko, M. P. Stoykovich, J. Z. Song, V. Malyarchuk, W. M. Choi, C. J. Yu, J. B. Geddes, J. L. Xiao, S. D. Wang, Y. G. Huang and J. A. Rogers, *Nature*, 2008, **454**, 748-753.

35. E. P. Chan, K. A. Page, S. H. Im, D. L. Patton, R. Huang and C. M. Stafford, *Soft Matter*, 2009, **5**, 4638-4641.

36. J. Y. Chung, T. Q. Chastek, M. J. Fasolka, H. W. Ro and C. M. Stafford, *ACS Nano*, 2009, **3**, 844-852.

37. J. Y. Chung, J. H. Lee, K. L. Beers and C. M. Stafford, *Nano Lett.*, 2011, **11**, 3361-3365.

38. J. Y. Chung, A. J. Nolte and C. M. Stafford, *Adv. Mater.*, 2009, **21**, 1358-1362.

39. C. M. Stafford, C. Harrison, K. L. Beers, A. Karim, E. J. Amis, M. R. Vanlandingham, H. C. Kim, W. Volksen, R. D. Miller and E. E. Simonyi, *Nat. Mater.*, 2004, **3**, 545-550.

40. W. H. Koo, S. M. Jeong, F. Araoka, K. Ishikawa, S. Nishimura, T. Toyooka and H. Takezoe, *Nat. Photonics*, 2010, **4**, 222-226.

41. P. J. Yoo, *Electron. Mater. Lett.*, 2011, **7**, 17-23.

42. L. Zhang, X. Y. Lang, A. Hirata and M. W. Chen, *ACS Nano*, 2011, **5**, 4407-4413.

43. J. B. Kim, P. Kim, N. C. Pegard, S. J. Oh, C. R. Kagan, J. W. Fleischer, H. A. Stone and Y. L. Loo, *Nat. Photonics*, 2012, **6**, 327-332.

44. D. Chandra, S. Yang, A. A. Soshinsky and R. J. Gambogi, *ACS Appl. Mater. Interfaces*, 2009, **1**, 1698-1704.

45. X. L. Zhu, Y. Zhang, D. Chandra, S. C. Cheng, J. M. Kikkawa and S. Yang, *Appl. Phys. Lett.*, 2008, **93**, 161911.

46. J. H. Jang, C. Y. Koh, K. Bertoldi, M. C. Boyce and E. L. Thomas, *Nano Lett.*, 2009, **9**, 2113-2119.

47. K. Khare, J. H. Zhou and S. Yang, *Langmuir*, 2009, **25**, 12794-12799.

48. H. S. Kim and A. J. Crosby, *Advanced materials (Deerfield Beach, Fla.)*, 2011, **23**, 4188-4192.

49. M. W. Moon, S. Chung, K. R. Lee, K. H. Oh, H. A. Stone and J. W. Hutchinson, *Int. J. Mater. Res.*, 2007, **98**, 1203-1208.

50. X. Y. Jiang, S. Takayama, X. P. Qian, E. Ostuni, H. K. Wu, N. Bowden, P. LeDuc, D. E. Ingber and G. M. Whitesides, *Langmuir*, 2002, **18**, 3273-3280.

51. H. Vandeparre, S. Gabriele, F. Brau, C. Gay, K. K. Parker and P. Damman, *Soft Matter*, 2010, **6**, 5751-5756.

52. J. Kim, J. Yoon and R. C. Hayward, *Nat. Mater.*, 2010, **9**, 159-164.

53. K. Bertoldi, P. M. Reis, S. Willshaw and T. Mullin, *Adv. Mater.*, 2010, **22**, 361-366.

54. C. Y. Hui, N. J. Glassmaker, T. Tang and A. Jagota, *J. R. Soc. Interface*, 2004, **1**, 35-48.

55. E. Arzt, S. Gorb and R. Spolenak, *Proc. Natl. Acad. Sci. U. S. A.*, 2003, **100**, 10603-10606.

56. Z. P. Bažant and L. Cedolin, *Stability of structures : elastic, inelastic, fracture, and damage theories*, Oxford University Press, New York, 1991.

57. B. Audoly and A. Boudaoud, *Phys. Rev. Lett.*, 2003, **91**, 086105.

58. J. Huang, M. Juszkiewicz, W. H. de Jeu, E. Cerda, T. Emrick, N. Menon and T. P. Russell, *Science*, 2007, **317**, 650-653.

59. D. Vella, M. Adda-Bedia and E. Cerda, *Soft Matter*, 2010, **6**, 5778-5782.

60. H. King, R. D. Schroll, B. Davidovitch and N. Menon, *Proc. Natl. Acad. Sci. U. S. A.*, 2012, **109**, 9716-9720.

61. M. Guvendiren, S. Yang and J. A. Burdick, *Adv. Funct. Mater.*, 2009, **19**, 3038-3045.

62. D. Chandra and A. J. Crosby, *Adv. Mater.*, 2011, **23**, 3441-3445.

63. P. J. Yoo and H. H. Lee, *Macromolecules*, 2005, **38**, 2820-2831.

64. T. R. Hendricks and I. Lee, *Nano Lett.*, 2007, **7**, 372-379.

65. C. C. Fu, A. Grimes, M. Long, C. G. L. Ferri, B. D. Rich, S. Ghosh, L. P. Lee, A. Gopinathan and M. Khine, *Adv. Mater.*, 2009, **21**, 4472-4476.

66. K. Efimenko, M. Rackaitis, E. Manias, A. Vaziri, L. Mahadevan and J. Genzer, *Nat. Mater.*, 2005, **4**, 293-297.

67. P. C. Lin and S. Yang, *Appl. Phys. Lett.*, 2007, **90**, 241903.

68. N. Bowden, W. T. S. Huck, K. E. Paul and G. M. Whitesides, *Appl. Phys. Lett.*, 1999, **75**, 2557-2559.

69. Z. Y. Huang, W. Hong and Z. Suo, *J. Mech. Phys. Solids*, 2005, **53**, 2101-2118.

70. H. Q. Jiang, D. Y. Khang, J. Z. Song, Y. G. Sun, Y. G. Huang and J. A. Rogers, *Proc. Natl. Acad. Sci. U. S. A.*, 2007, **104**, 15607-15612.

71. C. M. Chen and S. Yang, *Polym. Int.*, 2012, **61**, 1041-1047.

72. T. Ohzono and M. Shimomura, *Phys. Rev. B*, 2004, **69**, 132202.

73. T. Ohzono and M. Shimomura, *Phys. Rev. E*, 2005, **72**, 025203.

74. D. Breid and A. J. Crosby, *Soft Matter*, 2011, **7**, 4490-4496.

75. V. Reichert, S. K. Basu, L. F. Francis, A. V. McCormick and L. E. Scriven, *Prog. Org. Coat.*, 2008, **63**, 33-37.

76. H. Vandeparre and P. Damman, *Phys. Rev. Lett.*, 2008, **101**, 124301.

77. W. M. Choi, J. Z. Song, D. Y. Khang, H. Q. Jiang, Y. Y. Huang and J. A. Rogers, *Nano Lett.*, 2007, **7**, 1655-1663.

78. T. Ohzono, H. Watanabe, R. Vendamme, C. Kamaga, T. Kunitake, T. Ishihara and M. Shimomura, *Adv. Mater.*, 2007, **19**, 3229-3232.

79. S. J. Kwon, P. J. Yoo and H. H. Lee, *Appl. Phys. Lett.*, 2004, **84**, 4487-4489.

80. C. F. Guo, V. Nayyar, Z. W. Zhang, Y. Chen, J. J. Miao, R. Huang and Q. Liu, *Adv. Mater.*, 2012, **24**, 3010-3014.

81. J. Y. Chung, A. J. Nolte and C. M. Stafford, *Adv. Mater.*, 2011, **23**, 349-368.

82. S. G. Lee, D. Y. Lee, H. S. Lim, D. H. Lee, S. Lee and K. Cho, *Adv. Mater.*, 2010, **22**, 5013-5017.

83. P. C. Lin, S. Vajpayee, A. Jagota, C. Y. Hui and S. Yang, *Soft Matter*, 2008, **4**, 1830-1835.

84. E. P. Chan, E. J. Smith, R. C. Hayward and A. J. Crosby, *Adv. Mater.*, 2008, **20**, 711-716.

85. Y. Bai, C. R. Jin, A. Jagota and C. Y. Hui, *J. Appl. Phys.*, 2011, **110**, 054902.

86. J. Y. Chung, J. P. Youngblood and C. M. Stafford, *Soft Matter*, 2007, **3**, 1163-1169.

87. J. W. Hutchinson and Z. Suo, in *Advances in Applied Mechanics, Vol 29*, Academic Press Inc, San Diego, 1992, vol. 29, pp. 63-191.

88. C. Coupeau, *Thin Solid Films*, 2002, **406**, 190-194.

89. A. A. Volinsky, N. R. Moody and W. W. Gerberich, *Acta Mater.*, 2002, **50**, 441-466.

90. M. Ortiz and G. Gioia, *J. Mech. Phys. Solids*, 1994, **42**, 531-559.

91. B. Audoly, *Phys. Rev. Lett.*, 1999, **83**, 4124-4127.

92. H. H. Yu and J. W. Hutchinson, *Int. J. Fract.*, 2002, **113**, 39-55.

93. M. W. Moon, K. R. Lee, K. H. Oh and J. W. Hutchinson, *Acta Mater.*, 2004, **52**, 3151-3159.

94. A. Malachias, Y. F. Mei, R. K. Annabattula, C. Deneke, P. R. Onck and O. G. Schmidt, *ACS Nano*, 2008, **2**, 1715-1721.

95. T. J. W. Wagner and D. Vella, *Soft Matter*, 2013, **9**, 1025-1030.

96. S. S. Velankar, V. Lai and R. A. Vaia, *ACS Appl. Mater. Interfaces*, 2012, **4**, 24-29.

97. D. P. Holmes and A. J. Crosby, *Phys. Rev. Lett.*, 2010, **105**, 038303.

98. Y. Ebata, A. B. Croll and A. J. Crosby, *Soft Matter*, 2012, **8**, 9086-9091.

99. J. F. Zang, X. H. Zhao, Y. P. Cao and J. W. Hutchinson, *J. Mech. Phys. Solids*, 2012, **60**, 1265-1279.

100. F. Brau, P. Damman, H. Diamant and T. A. Witten, *Soft Matter*, 2013, In Press. DOI:10.1039/c1033sm50655j.

101. M. A. Biot, *Applied Scientific Research, Section A*, 1963, **12**, 168-182.

102. A. N. Gent and I. S. Cho, *Rubber Chem. Technol.*, 1999, **72**, 253-262.

103. M. Guvendiren, J. A. Burdick and S. Yang, *Soft Matter*, 2010, **6**, 5795-5801.

104. M. A. Biot, *Mechanics of incremental deformations*, Wiley, New York,, 1965.

105. Y. P. Cao and J. W. Hutchinson, *Proceedings of the Royal Society a-Mathematical Physical and Engineering Sciences*, 2012, **468**, 94-115.

106. S. Q. Cai, D. Y. Chen, Z. G. Suo and R. C. Hayward, *Soft Matter*, 2012, **8**, 1301-1304.

107. C. Majidi, R. E. Groff and R. Fearing, in *ASME 2004 International Mechanical Engineering Congress and Exposition*, ASME, Anaheim, California, USA, 2004, pp. 579-584.

108. C. Greiner, A. del Campo and E. Arzt, *Langmuir*, 2007, **23**, 3495-3502.

109. Y. Zhang, C. W. Lo, J. A. Taylor and S. Yang, *Langmuir*, 2006, **22**, 8595-8601.

110. S. H. Kang, N. Wu, A. Grinthal and J. Aizenberg, *Phys. Rev. Lett.*, 2011, **107**, 177802.

111. B. Pokroy, S. H. Kang, L. Mahadevan and J. Aizenberg, *Science*, 2009, **323**, 237-240.

112. V. R. Tirumala, R. Divan, L. E. Ocola and D. C. Mancini, *J. Vac. Sci. Technol. B*, 2005, **23**, 3124-3128.

113. V. R. Tirumala, C. M. Stafford, L. E. Ocola, J. F. Douglas and L. Mahadevan, *Nano Lett.*, 2012, **12**, 1516-1521.

114. H. Yoon, A. Ghosh, J. Y. Han, S. H. Sung, W. B. Lee and K. Char, *Adv. Funct. Mater.*, 2012, **22**, 3723-3728.

115. S. J. DuPont, R. S. Cates, P. G. Stroot and R. Toomey, *Soft Matter*, 2010, **6**, 3876-3882.

116. E. Sharon, B. Roman, M. Marder, G. S. Shin and H. L. Swinney, *Nature*, 2002, **419**, 579-579.

117. H. Yoon, H. Woo, M. K. Choi, K. Y. Suh and K. Char, *Langmuir*, 2010, **26**, 9198-9201.

118. G. N. Greaves, A. L. Greer, R. S. Lakes and T. Rouxel, *Nat. Mater.*, 2011, **10**, 823-837.

119. R. Lakes, *Science*, 1987, **235**, 1038-1040.

120. D. Y. Fozdar, P. Soman, J. W. Lee, L. H. Han and S. C. Chen, *Adv. Funct. Mater.*, 2011, **21**, 2712-2720.

121. J. Li, J. M. Shim, J. Deng, J. T. B. Overvelde, X. L. Zhu, K. Bertoldi and S. Yang, *Soft Matter*, 2012, **8**, 10322-10328.

122. X. L. Zhu, G. X. Wu, R. Dong, C. M. Chen and S. Yang, *Soft Matter*, 2012, **8**, 8088-8093.

123. J. T. B. Overvelde, S. Shan and K. Bertoldi, *Adv. Mater.*, 2012, **24**, 2337-2342.

124. J. Shim, C. Perdigou, E. R. Chen, K. Bertoldi and P. M. Reis, *Proc. Natl. Acad. Sci. U. S. A.*, 2012, **109**, 5978-5983.

125. S. H. Kang, S. Shan, W. L. Noorduin, M. Khan, J. Aizenberg and K. Bertoldi, *Adv. Mater.*, 2013, **25**, 3380-3385.

126. K. Autumn, Y. A. Liang, S. T. Hsieh, W. Zesch, W. P. Chan, T. W. Kenny, R. Fearing and R. J. Full, *Nature*, 2000, **405**, 681-685.

127. K. Autumn, M. Sitti, Y. C. A. Liang, A. M. Peattie, W. R. Hansen, S. Sponberg, T. W. Kenny, R. Fearing, J. N. Israelachvili and R. J. Full, *Proc. Natl. Acad. Sci. U. S. A.*, 2002, **99**, 12252-12256.

128. G. Huber, H. Mantz, R. Spolenak, K. Mecke, K. Jacobs, S. N. Gorb and E. Arzt, *Proc. Natl. Acad. Sci. U. S. A.*, 2005, **102**, 16293-16296.

129. W. R. Hansen and K. Autumn, *Proc. Natl. Acad. Sci. U. S. A.*, 2005, **102**, 385-389.

130. R. Spolenak, S. Gorb, H. J. Gao and E. Arzt, *Proc. R. Soc. London Ser. A-Math. Phys. Eng. Sci.*, 2005, **461**, 305-319.

131. H. J. Gao, X. Wang, H. M. Yao, S. Gorb and E. Arzt, *Mech. Mater.*, 2005, **37**, 275-285.

132. H. J. Gao and H. M. Yao, *Proc. Natl. Acad. Sci. U. S. A.*, 2004, **101**, 7851-7856.

133. C. Creton and S. Gorb, *MRS Bull.*, 2007, **32**, 466-472.

134. A. Jagota and C. Y. Hui, *Mater. Sci. Eng. R-Rep.*, 2011, **72**, 253-292.

135. Y. Tian, N. Pesika, H. B. Zeng, K. Rosenberg, B. X. Zhao, P. McGuiggan, K. Autumn and J. Israelachvili, *Proc. Natl. Acad. Sci. U. S. A.*, 2006, **103**, 19320-19325.

136. M. T. Northen, C. Greiner, E. Arzt and K. L. Turner, *Adv. Mater.*, 2008, **20**, 3905-3909.

137. S. Reddy, E. Arzt and A. del Campo, *Adv. Mater.*, 2007, **19**, 3833-3837.

138. N. J. Glassmaker, A. Jagota, C. Y. Hui, W. L. Noderer and M. K. Chaudhury, *Proc. Natl. Acad. Sci. U. S. A.*, 2007, **104**, 10786-10791.

139. L. T. Qu, L. M. Dai, M. Stone, Z. H. Xia and Z. L. Wang, *Science*, 2008, **322**, 238-242.

140. M. D. Bartlett, A. B. Croll, D. R. King, B. M. Paret, D. J. Irschick and A. J. Crosby, *Adv. Mater.*, 2012, **24**, 1078-1083.

141. L. Ge, S. Sethi, L. Ci, P. M. Ajayan and A. Dhinojwala, *Proc. Natl. Acad. Sci. U. S. A.*, 2007, **104**, 10792-10795.

142. H. Lee, B. P. Lee and P. B. Messersmith, *Nature*, 2007, **448**, 338-341.

143. A. Majumder, A. Ghatak and A. Sharma, *Science*, 2007, **318**, 258-261.

144. Y. Tian, J. Wan, N. Pesika and M. Zhou, *Sci Rep*, 2013, **3**, 1382.

145. M. P. Murphy, S. Kim and M. Sitti, *ACS Appl. Mater. Interfaces*, 2009, **1**, 849-855.

146. E. M. Petrie, *Handbook of adhesives and sealants*, 2nd edn., McGraw-Hill, New York, 2007.

147. I. Benedek, *Pressure-sensitive adhesives and applications*, 2nd edn., Marcel Dekker, New York, 2004.

148. M. Kamperman, E. Kroner, A. del Campo, R. M. McMeeking and E. Arzt, *Adv. Eng. Mater.*, 2010, **12**, 335-348.

149. R. Ruibal and V. Ernst, *J. Morphol.*, 1965, **117**, 271-293.

150. K. Autumn, *MRS Bull.*, 2007, **32**, 473-478.

151. K. Autumn, C. Majidi, R. E. Groff, A. Dittmore and R. Fearing, *J. Exp. Biol.*, 2006, **209**, 3558-3568.

152. K. L. Johnson, *Contact mechanics*, Cambridge University Press, Cambridge Cambridgeshire ; New York, 1985.

153. H. E. Jeong, J. K. Lee, H. N. Kim, S. H. Moon and K. Y. Suh, *Proc. Natl. Acad. Sci. U. S. A.*, 2009, **106**, 5639-5644.

154. B. A. Chen, P. G. Oppenheimer, T. A. V. Shean, C. T. Wirth, S. Hofmann and J. Robertson, *J. Phys. Chem. C*, 2012, **116**, 20047-20053.

155. A. Jagota and S. J. Bennison, *Integr. Comp. Biol.*, 2002, **42**, 1140-1145.

156. C. Y. Hui, A. J. Jagota, L. L. Shen, A. Rajan, N. Glassmaker and T. Tang, *J. Adhes. Sci. Technol.*, 2007, **21**, 1259-1280.

157. D. Voigt, A. Schweikart, A. Fery and S. Gorb, *J. Exp. Biol.*, 2012, **215**, 1975-1982.

158. M. B. V. Roberts, *Biology; a functional approach*, Ronald Press Co., New York,, 1972.

159. I. C. Gebeshuber and R. M. Crawford, *Proc. Inst. Mech. Eng. Part J.-J. Eng. Tribol.*, 2006, **220**, 787-796.

160. S. N. Gorb, *Philos. Trans. R. Soc. A-Math. Phys. Eng. Sci.*, 2008, **366**, 1557-1574.

161. A. J. Kinloch, *Adhesion and adhesives : science and technology*, Chapman and Hall, London ; New York, 1987.

162. H. Ko, J. Lee, B. E. Schubert, Y. L. Chueh, P. W. Leu, R. S. Fearing and A. Javey, *Nano Lett.*, 2009, **9**, 2054-2058.

163. C. Pang, T.-i. Kim, W. G. Bae, D. Kang, S. M. Kim and K.-Y. Suh, *Adv. Mater.*, 2012, **24**, 475-479.

164. A. V. Pocius, D. A. Dillard and M. K. Chaudhury, *Adhesion science and engineering*, 1st edn., Elsevier, Amsterdam ; Boston, 2002.

165. J. A. Williams, S. G. Davies and S. Frazer, *Tribology Letters*, 2007, **26**, 213-222.

166. S. N. Gorb and V. L. Popov, *Philos. Trans. R. Soc. Lond. Ser. A-Math. Phys. Eng. Sci.*, 2002, **360**, 211-225.

167. R. M. McMeeking, L. F. Ma and E. Arzt, *J. Appl. Mech.-Trans. ASME*, 2009, **76**, 031007.

168. C. Pang, D. Kang, T.-i. Kim and K.-Y. Suh, *Langmuir*, 2011, **28**, 2181-2186.

169. W. Barthlott and C. Neinhuis, *Planta*, 1997, **202**, 1-8.

170. D. L. Hu, B. Chan and J. W. M. Bush, *Nature*, 2003, **424**, 663-666.

171. X. Q. Feng, X. F. Gao, Z. N. Wu, L. Jiang and Q. S. Zheng, *Langmuir*, 2007, **23**, 4892-4896.

172. A. R. Parker and C. R. Lawrence, *Nature*, 2001, **414**, 33-34.

173. T. Young, *Philosophical Transactions of the Royal Society of London*, 1805, **95**, 65-87.

174. P.-G. de Gennes, F. Brochard-Wyart and D. Quéré, *Capillarity and wetting phenomena : drops, bubbles, pearls, waves*, Springer, New York, 2004.

175. M. E. Schrader, *J. Colloid Interface Sci.*, 1984, **100**, 372-380.

176. A. Lafuma and D. Quere, *Nat. Mater.*, 2003, **2**, 457-460.

177. R. N. Wenzel, *Ind. Eng. Chem.*, 1936, **28**, 988-994.

178. A. B. D. Cassie and S. Baxter, *Trans. Faraday Soc.*, 1944, **40**, 546-551.

179. A. J. B. Milne and A. Amirfazli, *Adv. Colloid Interface Sci.*, 2012, **170**, 48-55.

180. S. Shibuichi, T. Onda, N. Satoh and K. Tsujii, *J. Phys. Chem.*, 1996, **100**, 19512-19517.

181. J. Bico, U. Thiele and D. Quere, *Colloid Surf. A-Physicochem. Eng. Asp.*, 2002, **206**, 41-46.

182. Y. I. Frenkel, *J. Exptl. Theoret. Phys. (USSR)*, 1948, **18**, 659.

183. C. W. Extrand and Y. Kumagai, *J. Colloid Interface Sci.*, 1995, **170**, 515-521.

184. A. ElSherbini and A. Jacobi, *J. Colloid Interface Sci.*, 2006, **299**, 841-849.

185. C. J. Lv, C. W. Yang, P. F. Hao, F. He and Q. S. Zheng, *Langmuir*, 2010, **26**, 8704-8708.

186. M. Miwa, A. Nakajima, A. Fujishima, K. Hashimoto and T. Watanabe, *Langmuir*, 2000, **16**, 5754-5760.

187. L. Feng, S. H. Li, Y. S. Li, H. J. Li, L. J. Zhang, J. Zhai, Y. L. Song, B. Q. Liu, L. Jiang and D. B. Zhu, *Adv. Mater.*, 2002, **14**, 1857-1860.

188. Z. G. Guo, W. M. Liu and B. L. Su, *J. Colloid Interface Sci.*, 2011, **353**, 335-355.

189. E. Celia, T. Darmanin, E. T. de Givenchy, S. Amigoni and F. Guittard, *J. Colloid Interface Sci.*, 2013, **402**, 1-18.

190. P. Roach, N. J. Shirtcliffe and M. I. Newton, *Soft Matter*, 2008, **4**, 224-240.

191. L. Zhai, F. C. Cebeci, R. E. Cohen and M. F. Rubner, *Nano Lett.*, 2004, **4**, 1349-1353.

192. H. Y. Erbil, A. L. Demirel, Y. Avci and O. Mert, *Science*, 2003, **299**, 1377-1380.

193. R. G. Karunakaran, C. H. Lu, Z. H. Zhang and S. Yang, *Langmuir*, 2011, **27**, 4594-4602.

194. X. Deng, L. Mammen, H. J. Butt and D. Vollmer, *Science*, 2012, **335**, 67-70.

195. A. Tuteja, W. Choi, M. L. Ma, J. M. Mabry, S. A. Mazzella, G. C. Rutledge, G. H. McKinley and R. E. Cohen, *Science*, 2007, **318**, 1618-1622.

196. A. Tuteja, W. Choi, J. M. Mabry, G. H. McKinley and R. E. Cohen, *Proc. Natl. Acad. Sci. U. S. A.*, 2008, **105**, 18200-18205.

197. N. J. Shirtcliffe, S. Aqil, C. Evans, G. McHale, M. I. Newton, C. C. Perry and P. Roach, *J. Micromech. Microeng.*, 2004, **14**, 1384-1389.

198. N. J. Shirtcliffe, G. McHale, M. I. Newton, G. Chabrol and C. C. Perry, *Adv. Mater.*, 2004, **16**, 1929-1932.

199. L. Courbin, E. Denieul, E. Dressaire, M. Roper, A. Ajdari and H. A. Stone, *Nat. Mater.*, 2007, **6**, 661-664.

200. N. Obara and K. Okumura, *Phys. Rev. E*, 2012, **86**, 020601.

201. C. W. Extrand, S. I. Moon, P. Hall and D. Schmidt, *Langmuir*, 2007, **23**, 8882-8890.

202. V. Jokinen, M. Leinikka and S. Franssila, *Adv. Mater.*, 2009, **21**, 4835-4838.

203. R. J. Vrancken, M. L. Blow, H. Kusumaatmaja, K. Hermans, A. M. Prenen, C. W. M. Bastiaansen, D. J. Broer and J. M. Yeomans, *Soft Matter*, 2013, **9**, 674-683.

204. D. Y. Xia, L. M. Johnson and G. P. Lopez, *Adv. Mater.*, 2012, **24**, 1287-1302.

205. M. J. Hancock, K. Sekeroglu and M. C. Demirel, *Adv. Funct. Mater.*, 2012, **22**, 2223-2234.

206. S. Tawfick, M. De Volder, D. Copic, S. J. Park, C. R. Oliver, E. S. Polsen, M. J. Roberts and A. J. Hart, *Adv. Mater.*, 2012, **24**, 1628-1674.

207. Y. M. Zheng, X. F. Gao and L. Jiang, *Soft Matter*, 2007, **3**, 178-182.

208. H. Wu, R. Zhang, Y. Sun, D. D. Lin, Z. Q. Sun, W. Pan and P. Downs, *Soft Matter*, 2008, **4**, 2429-2433.

209. O. Bliznyuk, V. Veligura, E. S. Kooij, H. J. W. Zandvliet and B. Poelsema, *Phys. Rev. E*, 2011, **83**, 041607.

210. D. Y. Xia and S. R. J. Brueck, *Nano Lett.*, 2008, **8**, 2819-2824.

211. R. Seemann, M. Brinkmann, E. J. Kramer, F. F. Lange and R. Lipowsky, *Proc. Natl. Acad. Sci. U. S. A.*, 2005, **102**, 1848-1852.

212. S. Neuhaus, N. D. Spencer and C. Padeste, *ACS Appl. Mater. Interfaces*, 2012, **4**, 123-130.

213. T. I. Kim and K. Y. Suh, *Soft Matter*, 2009, **5**, 4131-4135.

214. K. H. Chu, R. Xiao and E. N. Wang, *Nat. Mater.*, 2010, **9**, 413-417.

215. C. Q. Lai, C. V. Thompson and W. K. Choi, *Langmuir*, 2012, **28**, 11048-11055.

216. M. L. Blow and J. M. Yeomans, *Philos. Trans. R. Soc. A-Math. Phys. Eng. Sci.*, 2011, **369**, 2519-2527.

217. N. A. Malvadkar, M. J. Hancock, K. Sekeroglu, W. J. Dressick and M. C. Demirel, *Nat. Mater.*, 2010, **9**, 1023-1028.

218. X. Y. Li, L. Q. Mao and X. H. Ma, *Langmuir*, 2013, **29**, 1129-1138.

Chapter 2

Guided wrinkling in osmotic swollen, pre-patterned photoresist thin films

2.1 Introduction

Wrinkling in thin films, including bi-layers[1-14] and layers with crosslinking gradient,[15-17] is of interests for a wide variety of applications, including organic light-emitting diodes,[5] flexible electronics,[18, 19] microlens array,[9, 20] adhesives[21, 22] and thin film metrology.[23] Depending on the type and conditions of the stress induced, pattern morphology and dimension can be fine-tuned with wavelength spanning from 0.1 to 100 μm when the stress exceeds the critical buckling stress. Mechanical[6, 7, 24] and osmotic stresses[8-12, 21, 25, 26] are commonly utilized to generate wrinkles.

Typically, random wrinkle morphology is formed on flat[1, 2, 5, 14, 15, 17, 24] and curved films[27, 28] under an isotropic stress (e.g. thermal annealing and solvent swelling/annealing). For most applications, however, ordered structures[9, 18, 19, 22] are desired. It has been demonstrated that one-dimension (1-D) ripples and two-dimension (2-D) zigzag wrinkles can be created by controlling the level and direction of applied mechanical strain.[6, 29-32] In the case of heating/cooling or solvent swelling/annealing of a patterned film,[2-4, 10, 11, 26, 33-35] the growing wrinkles can be aligned with the pattern edges due to the stress relaxation perpendicular to the propagating swelling wave front.[13] This alignment persists to a certain distance before the wrinkles become isotropic again. This persistence length is typically much larger than the intrinsic wavelength, which is determined by the stress state and the respective Young's modulus of the film and

substrate.[7, 9, 12, 26] It has been suggested that when confining the wrinkle with a template that is comparable or smaller than the persistent length, morphological alignment can be induced, where the wrinkle morphology depends on both the boundary geometry and the stress state.[2, 3, 9, 26] So far, experimentally there are only a few scattered results from pre-patterns with feature size smaller the wrinkle wavelength or amplitude.[2, 32, 36, 37] For example, Okayasu *et al.*[2] presented preliminary results on small pattern effect on thermally-induced wrinkles but the mechanism was not well-understood and the aligned wrinkles did not show long-range in-phase order. Ohzono *et al.*[37, 38] and Lee *et al.*[32] have also studied wrinkles formation on small subsumed patterns. However, for both of their systems, the wrinkles were mechanically generated whose morphology depends primarily on the applied stress rather than the pre-patterns.

Here, we were interested in the effect of pre-pattern size on the wrinkle formation and morphological evolution. For this purpose, we designed a new wrinkling system using SU-8 photoresist thin films (200 nm to 4 μm thick) consisting of light-absorbing dye molecules to create a depth-wise modulus gradient after photo-crosslinking. Wrinkles were induced by exposing the dyed SU-8 thin films to tetrahydrofuran (THF) solvent vapor. We then imprinted the dyed SU-8 film into 1-D channels by capillary force lithography (CFL)[39, 40] to guide the wrinkle formation and orientation. The pattern pitch was varied from 1 μm to 20 μm and height from 15 nm to 2 μm, that is an order of magnitude larger, comparable, or an order of magnitude smaller than the intrinsic wavelength and amplitude of the wrinkles obtained from the flat film, while keeping the pre-pattern's width/pitch ratio constant. At the smallest pre-pattern pitch (1 μm), the swollen film in the patterned region evolved from isotropic wrinkles to dual orientational

ones, where one set of wrinkles perpendicularly oriented to the pre-patterns and the other set of locally buckled patterns aligned in parallel to the pre-patterns as the pre-pattern height increased. Further increase of the pattern size and pitches led to anisotropic waves perpendicular to the pre-pattern either in-phase or out-of-phase depending on the size of the pre-pattern pitch vs. the intrinsic wrinkle wavelength. At the largest pre-pattern pitch (20 μm), isotropic wrinkles were confined on the thicker regions.

2.2 Experimental methods

2.2.1 Materials and fabrication

The SU-8 in γ-butyrolactone solution (SU-8 2 from Microchem) was mixed with rhodamine B (Aldrich) of at 6.26 mM, followed by sonication for 1 h to obtain homogeneous solutions. The cover glasses or Si wafers were used as substrates for coating SU-8 films. They were freshly cleaned by oxygen plasma (Harrick Expanded Plasma Cleaner & PlasmaFlo™) at ~30 W for 1 h. The dyed SU-8 film was spin-coated at 500 to 6000 rpm for 30 s on the substrate, and prebaked at 65°C for 1-5 min and 95°C for 1-5 min, respectively. The film was flood exposed to UV light (Newport 97435) of dosages ranging from 50 to 400 mJ, followed by post-exposure bake (PEB) at 95°C for the same duration as the pre-bake. For controlled swelling, the cured SU-8 film was placed in a glass jar and exposed to tetrahydrofuran (THF) (Fisher Scientific), which was placed in a separated glass container to create saturated vapor (see setup in Figure 2.1b) for a certain period of time.

For imprint lithography, we first created SU-8 masters by photolithography under UV flood exposure at the dosage of 50-300 mJ, depending on the photoresist thickness. Subsequently, the master patterns were replicated to a polydimethylsiloxane (PDMS,

Dow Corning Sylgard 184, 10:1 wt/wt precursor/crosslinker) mold. The dyed SU-8 films for swelling tests were prepared by imprint lithography following the procedure described in the literature.[40] The imprinted films were cured at 95°C and the swelling experiments were carried out following the procedure described above. The free standing dyed SU-8 film was prepared by etching away the glass substrate in 48 wt% hydrofluoric acid for 10 min, followed by DI water rinsing multiple times. It is then picked up onto a paraffin film for drying before the solvent exposure.

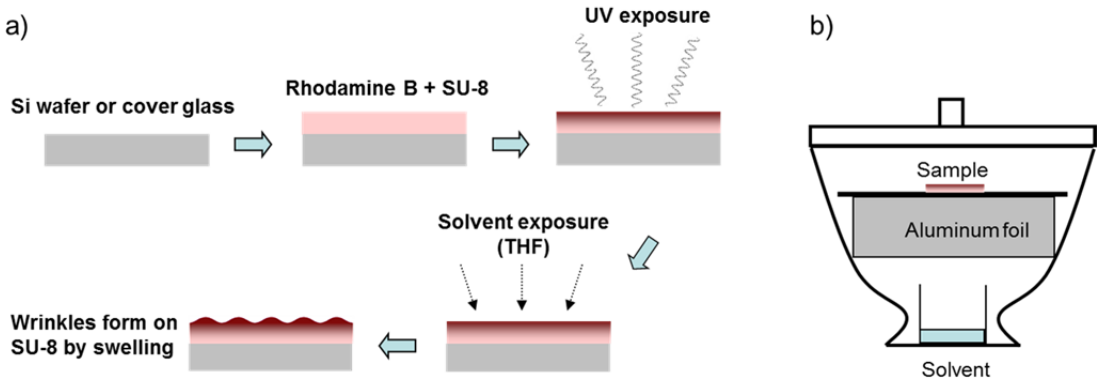

Figure 2.1 (a) Schematic illustration of the surface wrinkling process in the dyed SU-8 thin film upon swelling by a solvent. (b) Setup for the solvent exposure experiment.

2.2.2 Characterizations

The thickness of cured SU-8 films was measured using profilometer (Alpha Step 200) for film thickness > 500 nm and by ellipsometer (J. A. Woollam alpha-SE) for thinner films or by examining the cross-sectional image using scanning electron microscopy (SEM, FEI Quanta FEG ESEM and FEI Strata DB235). The wrinkle patterns and movies were captured from optical microscope (Olympus BX61) in the reflection mode. The morphologies of the wrinkling patterns were imaged using the aforementioned optical microscope, SEM and atomic force microscope (AFM, Veeco Dimension 3100).

The wrinkle wavelength was estimated by 2-D fast Fourier transform of the original pattern using ImageJ. The UV-vis spectra of SU-8 films cast on cover glasses were obtained from Cary Varian 5000, scanned in the range of 200 to 800 nm. The fluorescent intensity profile across the depth is obtained by Leica SP5-MP confocal microscope excited by a 543 nm diode laser.

2.3 Dyed SU-8 photoresist as a wrinkling platform

Previously, we have created a hydrogel thin film with gradient crosslinking density as a wrinkling platform by taking advantage of oxygen diffusion gradient in poly(2-hydroxyethyl methacrylate) (PHEMA) hydrogel films, which has a softer upper layer and stiffer bottom layer near the substrate.[17] When immersed in water, the softer top layer swells more than the stiffer layer underneath, resulting in a net compressive stress that buckles the film above the critical stress threshold. The wrinkle morphology is found dependent on the crosslinker concentration, whereas the wrinkle wavelength (on the order of 50 μm and larger) is proportional to the film thickness.[16, 17] Similarly, Chandra and coworkers have demonstrated self-wrinkling during UV-curing of acrylate monomers,[15] where a crosslinking gradient is introduced due to the presence of oxygen on the top layer. The liquid top layer spontaneously swells the underlying crosslinked film to form wrinkles, where the wrinkle size is controlled by the resin thickness, and oxygen and photoinitiator concentrations.

Torres *et al*., on the other hand, have created gradient thin films from poly(furfuryl alcohol) with a stiff top layer and softer bottom layer.[41] The compressive stress is originated from the volumetric contraction of the top polymerized layer on the less crosslinked, viscoelastic bottom layer. The wavelength or morphology in such system is

found indirectly controlled by the photoacid generator concentration and the curing temperature, while the wrinkling mechanism is not fully understood. Moreover, the demonstrated wrinkle alignment is based on well-understood edge effect. It is yet to be seen whether the wrinkle wavelength and morphology can be readily controlled in such gradient films using simple geometrical parameters. More importantly, questions remain whether we can direct the wrinkle formation using a pre-pattern; what is the relationship between the intrinsic wrinkle size vs. pre-pattern size and what determines the wrinkling morphology.

SU-8 is a photoresist that has been commonly used in conventional photolithography and holographic lithography to create various micro- and nanostructures. The unexposed SU-8 film, however, is thermoplastic. It has a low T_g (~ 50 ^oC) and relatively low viscosity above T_g, Previously, we have used CFL and thermal reflow, followed by UV curing through a mask to create hierarchical pillar structures.[40] Here, by swelling photocrosslinked SU-8 thin films with dye molecules (Figure 2.1), we created wrinkles with wavelength ranging from a few hundred nanometers to a few micrometers.

As the light passes through a light absorbing medium, it decays exponentially along the film thickness, forming a gradient crosslinking density decreasing from the top to the bottom.[42] This phenomenon has recently been utilized to fabricate reversibly foldable structure based on SU-8 photoresist.[43] In our system, we added rhodamine B dye in the SU-8 thin film (Figure 2.1a and 2.2), to promote the formation of crosslinking gradient.

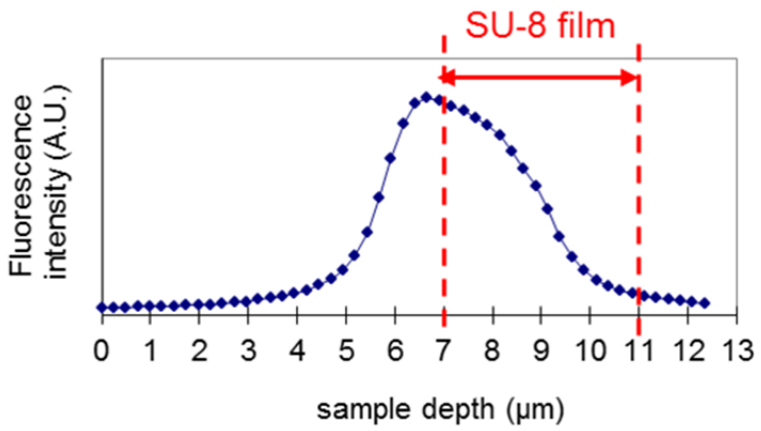

Figure 2.2 Fluorescent intensity of rhodamine B along the depth of SU-8 film.

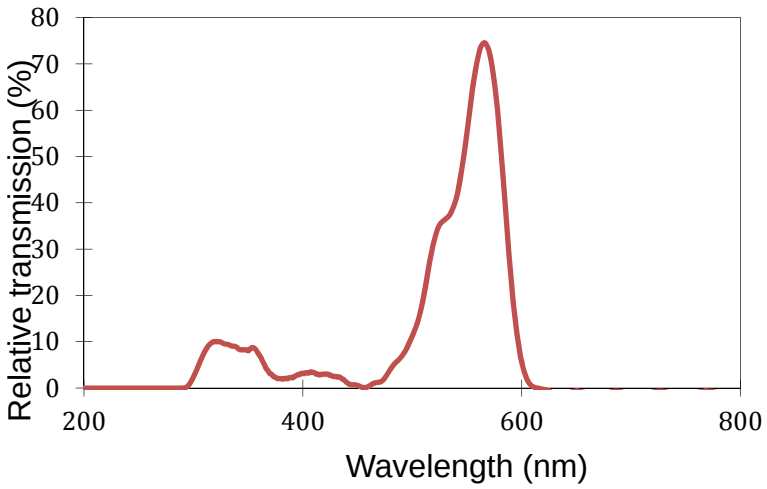

Figure 2.3 The relative transmittance of a dyed SU-8 (3.8μm, 6.26 mM rhodamine B) vs. a pure SU-8 film.

As seen in Figure 2.3, addition of rhodamine B decreased the UV transmission by ~10% averaged over 3.8 μm. On the top of the film, more than 10% of the light would be absorbed, leading to a higher concentration of photoacids, which was attenuated toward the substrate, thus, creating a crosslink gradient. To confirm this, we detached SU-8 film with rhodamine B of the same thickness from the substrate for swelling in THF vapor. If

the crosslinking density is higher at the outer surface, the film should bend toward the surface caused by the strain mismatch since the layer near the substrate should have a lower crosslinking density, leading to higher swelling ratio and larger strain. As seen in Figure 2.4, the as-detached film naturally curled toward the substrate side, indicating residual thermal stress generated in the graded film during curing.[44] Upon exposure to THF vapor for 16 h, the film reversibly bent upward and crumpled as we expected, confirming the existence of a stiffer layer on top and a crosslinking gradient along film thickness. Moreover, compared to a much longer solvent exposure time (> 4h) to swell the free-standing pure SU-8 film, which lowered the film the glass transition temperature (T_g) of the SU-8 film, causing the film to buckle, only 20-40 min solvent swelling was needed to buckle the dyed SU-8 of the same thickness but attached to the substrate. These observations confirmed that the wrinkling of the dyed SU-8 should be triggered by the residual stress upon swelling.

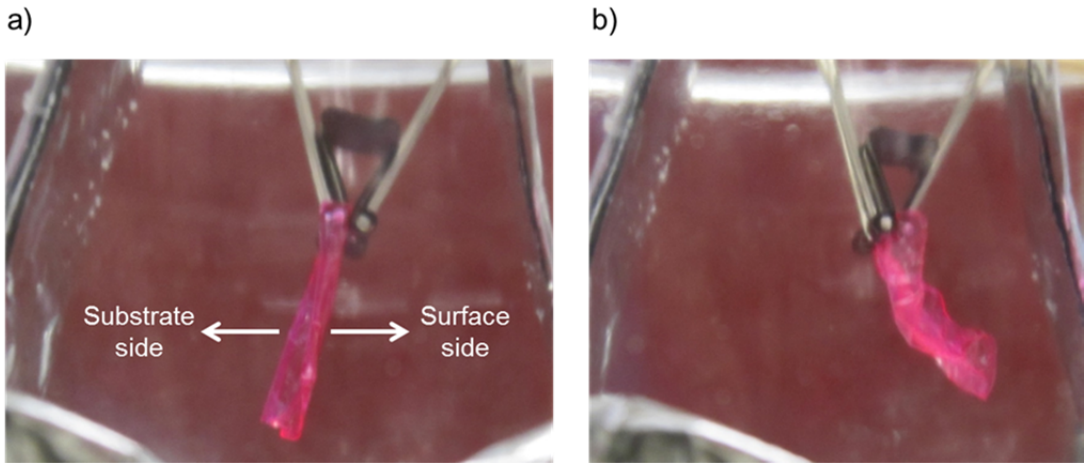

Figure 2.4 Curling of a free-standing dyed SU-8 film (3.8μm). (a) As-detached film. (b) Sample shown in (a) was exposed to THF vapor for 16 h.

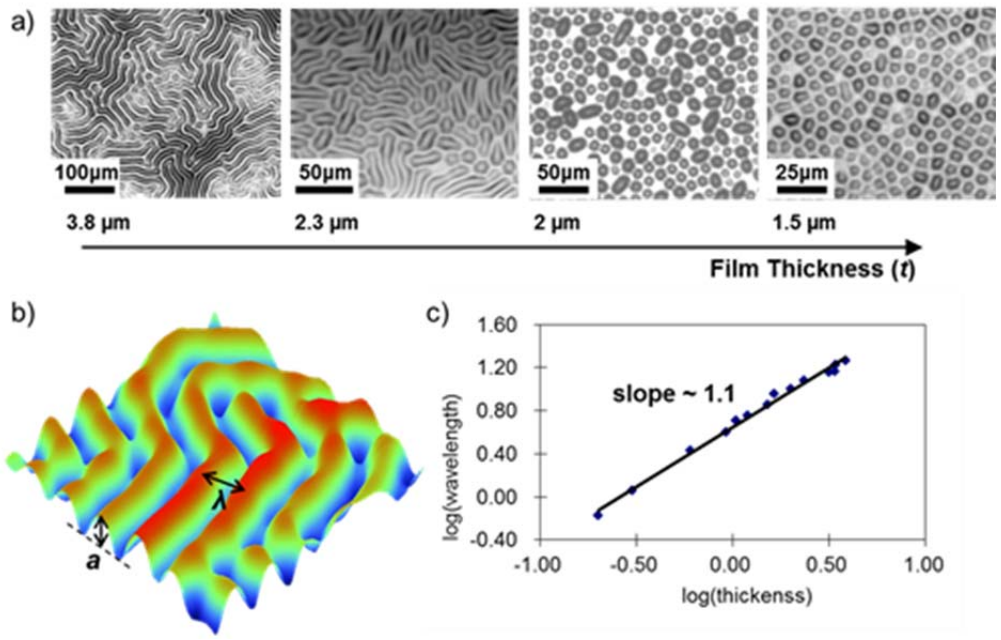

Figure 2.5 (a) Morphologic evolution of wrinkles formed when swelling the dyed SU-8 films with different thickness on a substrate, from lamella, peanut to hexagon when decreasing film thickness. (b) Representative AFM image of an isotropic wrinkles generated by THF swelling. (c) Wrinkle wavelength as a function of film thickness.

The thin film morphology changed from lamella, peanut to semi-hexagon patterns as film thickness decreased (see Figure 2.5a). This can be explained by that the hexagonal pattern was first formed near the critical buckling stress when only one eigenmode prevailed, whose wavevectors were equal in magnitude and summed up to zero.[45] When the residual stress was increased with the increase of film thickness, higher order modes appeared and the hexagon transformed to peanut, and finally lamellar structures when the film thickness reached to 3.8 μm (Figure 2.5a).[14, 17, 45] Also it can be seen in Figure 2.5b-c that the wrinkle wavelength λ is linearly proportional to the film thickness. The results are different from our previous observation when swelling gradient hydrogel films with softer top layer: the wrinkling morphology is dependent on crosslinker concentration but

not film thickness; and the wrinkle wavelength is linearly proportional to the film thickness.[17]

2.4 Guided wrinkling on pre-patterned photoresist

Building upon the studies in flat films, we prepared 9 samples from the dyed SU-8 (~3.8 μm thick) with channel-type pre-patterns (see Figure 2.6 and Table 2.1) with fixed pitch p to width w ratio (p = 2w) and variable height h and p, which were larger, comparable, or smaller than the intrinsic wrinkle wavelength λ and amplitude a, to probe geometric effect of pre-patterns on the wrinkle morphology. The pre-pattern height in our experiment was always smaller than the film thickness due to existence of the residual film during imprint lithography.[39] Although no external pressure was applied during the imprinting, we found that the average film thickness decreased by ~ 400 nm to ~ 3.4 μm, where the excess SU-8 was expelled to the surrounding area near the mold. At this thickness, the average wrinkle λ =16.7 μm and the average a = 724 nm.

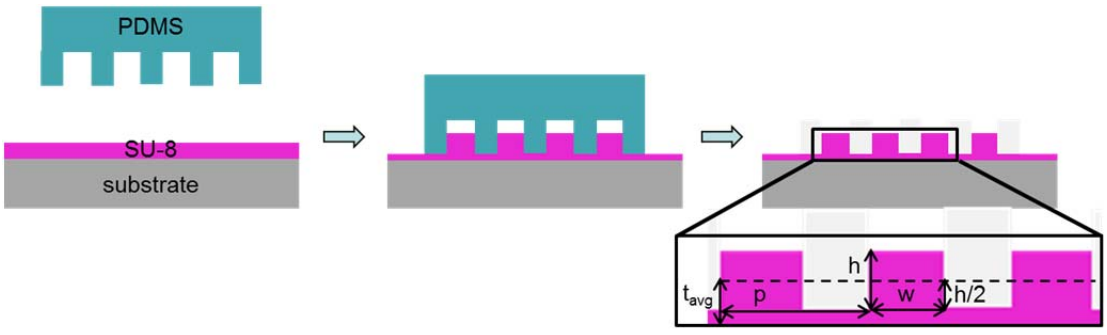

Figure 2.6 (a) Fabrication of 1-D pre-pattern on the SU-8 film by imprint lithography. h is the pattern height, p is the pitch, w is the width and t_{avg} is the average film thickness.

Pre-pattern dimension									
Pitch *p*	200 μm			20 μm			1 μm		
Height *h*	2 μm	800 nm	300 nm	2 μm	800 nm	300 nm	300 nm	60 nm	15 nm

Table 2.1. Pre-pattern dimensions.

On the pre-pattern with p = 200 μm, the wrinkles were confined primarily on the mountain regions of the 1-D pre-pattern (Figure 2.7a-c). This can be understood by the difference in critical buckling strain. Lee and coworkers[46] showed theoretically that in a graded film, the critical buckling strain decreases with the increase of surface to near-substrate modulus ratio. Since the pre-patterned SU-8 film was subjected to the same UV dosage in the pre-pattern as in the flat regions, the modulus gradient should be more pronounced on the thicker region with the bottom layers softer than those in the thinner region. Therefore, the wrinkles tend to nucleate first on the mountain region of the pre-patterns. It is apparent that these confined wrinkles remain essentially isotropic but subject to edge effects.[13, 26] As the pre-pattern height decreased, the wrinkles began to nucleate at the valley region. This is reasonable because the depth of the valley regions decreased with pre-pattern height h during imprinting. For example, for a pre-pattern with h = 2 μm, the mountain region would be $t_{avg} + h/2$ = 4.4 μm thick while the valley region would be $t_{avg} - h/2$ = 2.4 μm thick (see Figure 2.6 for definition). Here, t_{avg} is the average film thickness, which remained at ~3.4 μm, for the conservation of local volume. For a pre-pattern with h = 800 nm, to keep the same average film thickness, the mountain region would be ~3.8 μm while the valley region would be ~3 μm.

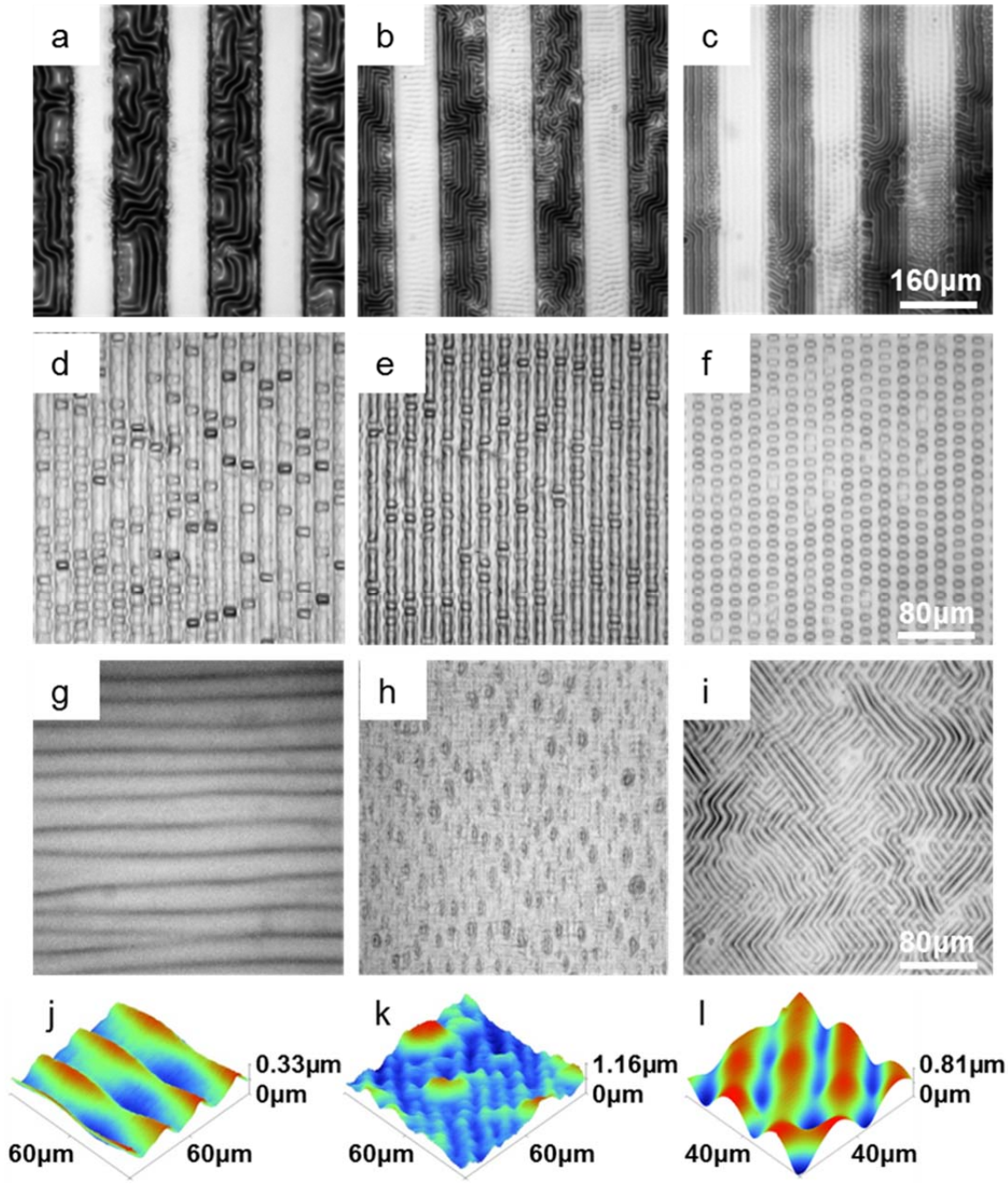

Figure 2.7 Optical images of the wrinkle morphology when swelling a pre-patterned SU-8 film doped with rhodamine B (3.4 μm thick) in THF for 40 min. (a-c) p = 200 μm (darker regions have larger height). (a) h = 2μm. (b) h = 800nm. (c) h = 300nm. Scale bar in (c) is applicable to (a-c). (d-f) p = 20μm. (d) h = 2μm. (e) h = 800nm. (f) h = 300nm. (g-l) p = 1μm. (g) h = 300nm. (h) h = 60nm. (i) h = 15nm. Scale bar in f is applicable to (d-i). (j-l) AFM images of (g-i) at higher magnification.

For p = 20 μm pre-patterns, the pattern size was comparable to the wrinkle wavelength (~16.7 μm). In this case, the wrinkles lost their isotropic nature completely and their formation was dominated by the edge effect of the pre-patterns. Therefore, they were aligned perpendicularly to the pre-pattern wavevector. On the pre-patterns with h comparable with or larger than the intrinsic wrinkle amplitude a, undulations started from the edges (Figure 2.8) and gradually evolved into bumps (Figure 2.7d and 2.7e) at the end of the swelling. In fact, this type of edge perturbation also occurred on the 200 μm pitch pre-patterns when $h \geq 800$ nm (Figure 2.7a and 2.7b). This can be explained by the fact that the solvent diffused from both the top surface and the sidewall on the edges, which effectively released the residual stress initially. As the stress level increased with extended solvent exposure, bumps form across the mountain region of 20 μm pitch pre-patterns to release excessive stresses. On the other hand, for h = 300 nm (smaller than a = 724 nm), this process was much less significant and a regular array of bumps grew directly on the mountain region of pre-patterns (see Figure 2.7f).

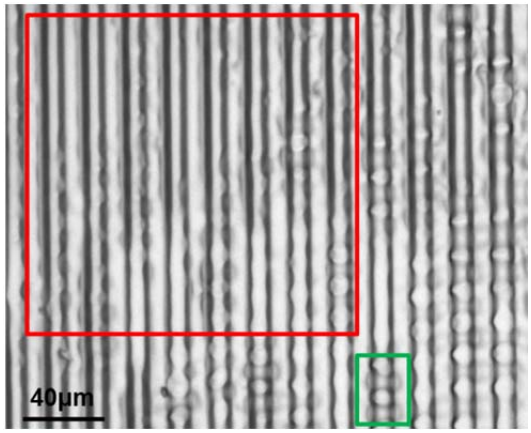

Figure 2.8 Edge undulation (highlighted in red) and premature wrinkle on the SU-8 pre-patterns (p=20 μm, h=800 nm) after swollen in THF for ~30 min. The deformation in the valley region caused by the wrinkle formation can also be observed (highlighted in green).

The alignment of wrinkles on the pre-patterns with p (=1μm) < λ is distinct at different h. For h = 300 nm, the wrinkles aligned perpendicularly to the pre-pattern with a pronounced long-range in-phase order as shown in Figure 2.7g and 2.7j. Compared to Figure 2.7f, the effect of changing p from 20 μm to 1 μm was significant. As we mentioned earlier that when the compressive stress in a flat film is just above the critical buckling threshold, a hexagonal array pattern is formed, Here, an array of hexagonal bumps appered. As the stress increased, the lamella structure was observed as shown in Figure 2.7b and 2.7c, both on the mountain and valley regions. When the confinement size decreased, wrinkles nucleated preferentially on the mountain region, the buckling pattern would no longer be confined only to the mountain region of the pre-pattern because the intrinsic wavelength was larger than the pre-pattern pitch. It can be seen in Figure 2.7d to 2.7f and more clearly in Figure 2.8 that the buckling pattern confined on the mountain region could cause deformation in the valley. We speculate that for p =1 μm, much smaller than λ, such buckling pattern should interact with neighboring pre-patterns. If one bump is to form from a mountain region of the pre-pattern, its size should span through a few pitches across the pre-patterns. This bump could then provide adjacent pre-patterns a preferential location for further growth of the buckling pattern, sustaining the long-range order as shown in Figure 2.7g and 2.7j. However, this long-range order introduced additional bending rigidity originated from the pre-patterns. Approximating the bending of the pre-patterns on the dyed SU-8 film as an orthogonally stiffened plate, we can derive the bending rigidity D_p perpendicular to the direction of pre-pattern wavevector as[47]

$$D_p \sim D + \frac{Etz_p^3}{1-\upsilon^2} + \frac{EI_p}{p} \qquad (2.1)$$

assuming there is a new neutral plane (Figure 2.9), where D is the bending rigidity of the flat film, E is the modulus of the film, t is the film thickness, z_p is the distance between the new neutral plane and the middle plane of the flat film, v is the Poisson ratio of the film, and I_p is the moment of inertia of the stiffener (mountain region of the pre-pattern) with respect to the new neutral plane.

The second and third terms of Eq. 2.1 represent the additional bending rigidity from the pre-patterns. For the wrinkles, this implies a higher bending energy penalty, which prefers formation of wrinkles of longer wavelength with smaller amplitude.[48] Indeed, experimentally we observed that increase of the average wavelength of the aligned wrinkles to 20 μm led to decrease of amplitude to 200 nm from the pre-patterns (p = 1 μm, h = 300 nm).

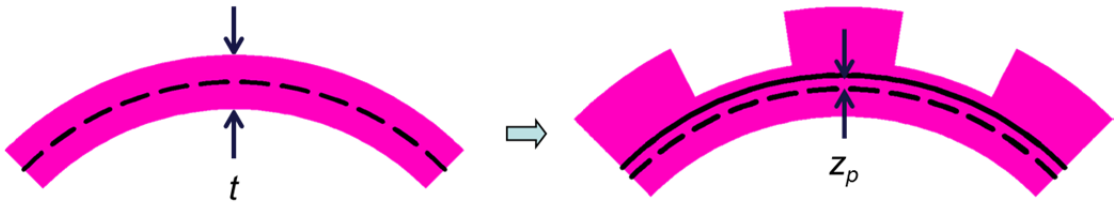

Figure 2.9 Schematic of the shifting of neutral plane for bending and the parameters, t: the thickness of a flat plate; z_p: the shifting distance of the neutral plane.

We note that when decreasing h from 300 nm to 60 nm on p =1 μm pre-patterns, a dramatic change in morphology occurred (Figure 2.7h). Two types of buckling were observed. One set of wrinkles (λ = 7.6 μm and a = 152.2 nm) was aligned perpendicularly

to the pre-pattern, similar to the wrinkles on h = 300 nm pre-patterns. The second one was localized and elongated bulges with the short axis parallel to the pre-patterns. Different from the first set of aligned wrinkles, the bulges had a broad distribution of aspect ratio and amplitude (see Figure 2.7h and 2.7k); the amplitude could be much larger than the aligned wrinkles. Experimentally, the aligned wrinkles always preceded the growth of bulges, indicating the aligned wrinkles grew just above the critical buckling threshold. The fact that the wavelength of the aligned wrinkles is smaller than that from the flat film (~16.7 μm) may imply that the first set was a result of pre-buckling.[14, 41, 49] Rather than growing to the full wavelength wrinkles, further stress release above the buckling threshold was achieved by forming the localized bulges, similar to other localized secondary buckling patterns, such folding[50, 51] and ridge-like structures.[52]

Although the exact formation mechanism of these wrinkles with dual-scale and orientation remained unclear, we believe that this was the interplay of the wrinkle nucleation and bending rigidity of the gradient film. As mentioned above, the wrinkles tended to nucleate from the thicker region in our system that led to the aligned wrinkles shown in Figures 2.7a – 2.7g. For the pre-pattern of h = 60nm and p = 1 μm, wrinkles still nucleated from the pre-pattern's mountain regions, forming the in-phase pre-buckles. However, comparing to film of h = 300 nm, the secondary wrinkle would nucleate immediately after the formation of the primary pre-buckles before it had a chance to grow into full wavelength wrinkles. Furthermore, the secondary wrinkle should nucleate at the higher over-stress (well above the critical buckling threshold), resulting in larger wrinkle amplitude. At the similar wavelength, larger amplitude implies larger curvature and a higher bending energy. Presumably, bending rigidity is smaller along the pre-pattern

wavevector that force these secondary wrinkles to grow in parallel to the pre-pattern channels. In addition, the nucleation and growth of secondary wrinkles occurs on top of the primary pre-buckles would require extra energy to do so. This may explain why the secondary wrinkles were absent in thicker films with h = 300 nm. Nonetheless, to verify this hypothesis and to identify the point of transition from in-phase alignment to dual buckling and finally to isotropic morphology, more investigations will be needed in the future. When the pre-pattern height h was further decreased to ~15 nm, which was two orders of magnitude smaller than the intrinsic wrinkle amplitude, the pre-patterns had little effect on the wrinkle formation or orientation (Figure 2.7i and 2.7l).

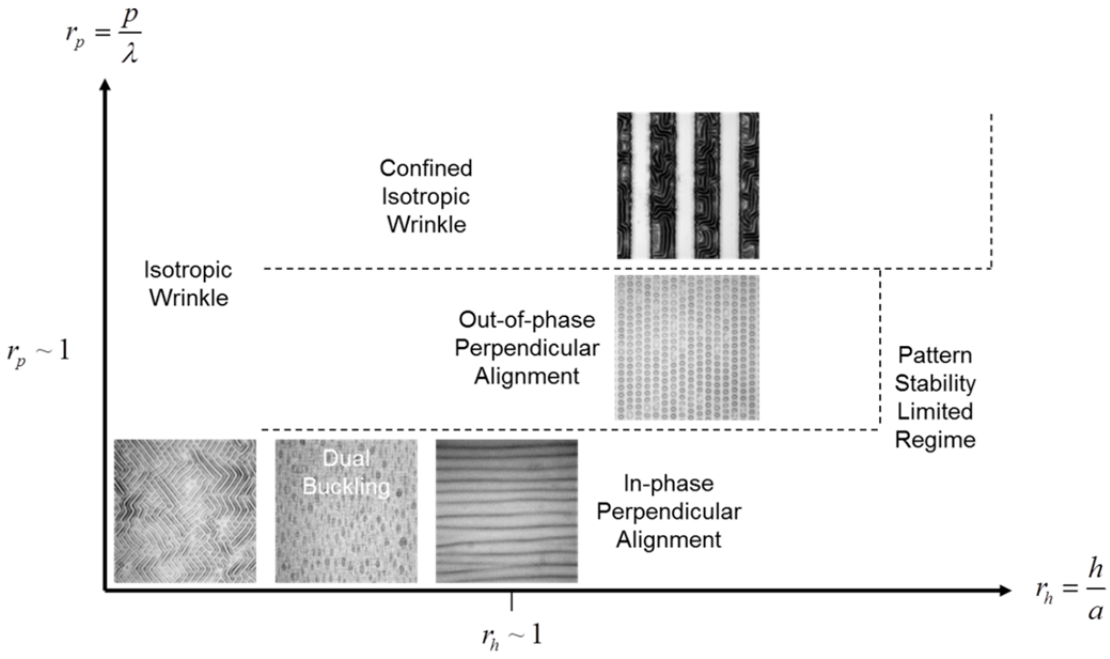

Figure 2.10 Morphology diagram for wrinkle alignment as a function of the ratio of pre-pattern amplitude to film thickness r_t and the ratio of pre-pattern wavelength to wrinkle wavelength r_w.

The wrinkle morphology as a function of 1-D pre-pattern dimension can be summarized in a morphology map shown in Figure 2.10. We introduced the pitch ratio $r_p = p/\lambda$ and height ratio $r_h = h/a$ as primary parameters. When $r_h << 1$, the wrinkle remained isotropic. When $r_h >> 1$, the pre-pattern aspect ratio (h/p) is limited by the elasticity of the material at $r_p << 1$ since swelling will decrease the film modulus. The wrinkle morphology on pre-patterns with $r_p > 1$ stayed isotropic but was confined to buckle first on the pattern's mountain regions. As $r_p \sim 1$, only 1-D wrinkles were possible on the pre-pattern mountain regions. For the intermediate r_h in between these two regimes, the morphology is highly dependent on the wrinkle wavelength. When $r_p \geq 1$, the confined isotropic or 1-D wrinkles still dominated in the respective regions. A previous study[26] agrees with our observation and suggests that the 1-D wrinkle would occur whenever the lateral dimension of the pre-pattern is smaller than the persistent length of the isotropic wrinkles. For 1-D wrinkles in this regime, it was also observed that there was no phase correlation between the neighboring mountain regions. For $r_p << 1$, two additional wrinkle alignment configurations are possible. In the case of $r_h \sim 1$, the wrinkles aligned perpendicular to the pre-patterns. This type of alignment showed a long-range in-phase order, unlike the case of $r_p \sim 1$. Further reducing r_h led to the dual buckling with the primary pre-buckling wrinkles aligned perpendicular to the pre-pattern wavevector and the secondary bulges aligning its short axis parallel to the pre-patterns.

2.5 Conclusion

We developed a new wrinkling system by UV curing dyed photoresist, SU-8, thin films, followed by solvent swelling. A gradient modulus with stiffer layer on top was obtained after photocrosslinking and a library of isotropic pattern morphologies with

wrinkle wavelength ranging from 700 nm to 20 μm were generated depending on the original film thickness. We then introduced 1-D channel-type pre-patterns with different dimensions to manipulate the wrinkle formation and its morphology. Specifically, we investigated the effect of pre-pattern pitch and height on wrinkle morphology, and whether wrinkles appeared on the mountain or valley regions of the pre-patterns. At the smallest pre-pattern height (~ 15 nm), no prominent change in morphology was observed and the wrinkles remained isotropic. As the height increased, different types of wrinkle alignment emerged depending on the commensurate between the intrinsic winkle wavelength and the pre-pattern size. At the largest wrinkle wavelength (~20 μm), confined isotropic wrinkles were nucleated first on the mountain regions of the pre-patterns. When wrinkle wavelength and amplitude were comparable to those of the pre-pattern, the wrinkles aligned perpendicular to the pre-pattern in an out-of-phase fashion. When the pre-pattern pitch became approximately an order of magnitude smaller than that of the intrinsic wrinkle wavelength, two distinct morphologies were observed depending on the pre-pattern height. When the height was close to the intrinsic wrinkle amplitude, the in-phase perpendicular order prevailed. Further decreasing the pre-pattern height gave rise to 1) small pre-buckling wrinkles aligned perpendicular to the pre-pattern and 2) bulges aligned parallel to the pre-patterns. The combination of patterning and depth-wise crosslinking gradient in polymer thin films will offer new strategies to create hierarchical structures with desired orientations, especially in the case when pre-pattern size is smaller than the intrinsic wrinkling wavelength. The rich morphologies demonstrated here in the range of submicron to microns could potentially lead to new optical or wetting applications.

2.6 Reference

1. N. Bowden, S. Brittain, A. G. Evans, J. W. Hutchinson and G. M. Whitesides, *Nature*, 1998, **393**, 146-149.

2. T. Okayasu, H. L. Zhang, D. G. Bucknall and G. A. D. Briggs, *Adv. Funct. Mater.*, 2004, **14**, 1081-1088.

3. S. J. Kwon, P. J. Yoo and H. H. Lee, *Appl. Phys. Lett.*, 2004, **84**, 4487-4489.

4. P. J. Yoo, K. Y. Suh, S. Y. Park and H. H. Lee, *Adv. Mater.*, 2002, **14**, 1383-1387.

5. W. H. Koo, S. M. Jeong, F. Araoka, K. Ishikawa, S. Nishimura, T. Toyooka and H. Takezoe, *Nat. Photonics*, 2010, **4**, 222-226.

6. P. C. Lin and S. Yang, *Appl. Phys. Lett.*, 2007, **90**, 241903.

7. W. M. Choi, J. Z. Song, D. Y. Khang, H. Q. Jiang, Y. Y. Huang and J. A. Rogers, *Nano Lett.*, 2007, **7**, 1655-1663.

8. J. Y. Chung, A. J. Nolte and C. M. Stafford, *Adv. Mater.*, 2009, **21**, 1358-1362.

9. E. P. Chan and A. J. Crosby, *Adv. Mater.*, 2006, **18**, 3238-+.

10. S. J. Kwon and J. G. Park, *J. Phys. Chem. C*, 2007, **111**, 4404-4411.

11. W. X. Qian, R. B. Xing, X. H. Yu, X. J. Quan and Y. C. Han, *J. Chem. Phys.*, 2007, **126**, 064901.

12. H. Vandeparre, S. Gabriele, F. Brau, C. Gay, K. K. Parker and P. Damman, *Soft Matter*, 2010.

13. H. Vandeparre and P. Damman, *Phys. Rev. Lett.*, 2008, **101**, 124301.

14. D. Breid and A. J. Crosby, *Soft Matter*, 2011, **7**, 4490-4496.

15. D. Chandra and A. J. Crosby, *Adv. Mater.*, 2011, **23**, 3441-+.

16. M. Guvendiren, J. A. Burdick and S. Yang, *Soft Matter*, 2010, **6**, 2044-2049.

17. M. Guvendiren, S. Yang and J. A. Burdick, *Adv. Funct. Mater.*, 2009, **19**, 3038-3045.

18. D. Y. Khang, H. Q. Jiang, Y. Huang and J. A. Rogers, *Science*, 2006, **311**, 208-212.

19. D. H. Kim, J. H. Ahn, W. M. Choi, H. S. Kim, T. H. Kim, J. Z. Song, Y. G. Y. Huang, Z. J. Liu, C. Lu and J. A. Rogers, *Science*, 2008, **320**, 507-511.

20. D. Chandra, S. Yang and P. C. Lin, *Appl. Phys. Lett.*, 2007, **91**, 251912.

21. E. P. Chan, E. J. Smith, R. C. Hayward and A. J. Crosby, *Adv. Mater.*, 2008, **20**, 711-+.

22. P. C. Lin, S. Vajpayee, A. Jagota, C. Y. Hui and S. Yang, *Soft Matter*, 2008, **4**, 1830-1835.

23. J. Y. Chung, A. J. Nolte and C. M. Stafford, *Adv. Mater.*, 2011, **23**, 349-368.

24. K. Efimenko, M. Rackaitis, E. Manias, A. Vaziri, L. Mahadevan and J. Genzer, *Nat. Mater.*, 2005, **4**, 293-297.

25. D. Breid and A. J. Crosby, *Soft Matter*, 2009, **5**, 425-431.

26. E. P. Chan and A. J. Crosby, *Soft Matter*, 2006, **2**, 324-328.

27. S. Kundu, C. S. Davis, T. Long, R. Sharma and A. J. Crosby, *J. Polym. Sci. Pt. B-Polym. Phys.*, 2011, **49**, 179-185.

28. A. C. Trindade, J. P. Canejo, L. F. V. Pinto, P. Patricio, P. Brogueira, P. I. C. Teixeira and M. H. Godinho, *Macromolecules*, 2011, **44**, 2220-2228.

29. T. Ohzono and M. Shimomura, *Phys. Rev. B*, 2004, **69**, 132202.

30. T. Ohzono and M. Shimomura, *Phys. Rev. E*, 2005, **72**, 025203.

31. T. Ohzono and M. Shimomura, *Langmuir*, 2005, **21**, 7230-7237.

32. J. H. Lee, H. W. Ro, R. Huang, P. Lemaillet, T. A. Germer, C. L. Soles and C. M. Stafford, *Nano Lett.*, 2012, **12**, 5995-5999.

33. P. J. Yoo and H. H. Lee, *Langmuir*, 2008, **24**, 6897-6902.

34. J. Yin and C. H. Lu, *Soft Matter*, 2012, **8**, 6528-6534.

35. E. P. Chan, J. M. Karp and R. S. Langer, *J. Polym. Sci. Pt. B-Polym. Phys.*, 2011, **49**, 40-44.

36. C. F. Guo, V. Nayyar, Z. W. Zhang, Y. Chen, J. J. Miao, R. Huang and Q. Liu, *Adv. Mater.*, 2012, **24**, 3010-3014.

37. T. Ohzono, H. Watanabe, R. Vendamme, C. Kamaga, T. Kunitake, T. Ishihara and M. Shimomura, *Adv. Mater.*, 2007, **19**, 3229-3232.

38. T. Ohzono, H. Watanabe, R. Vendamme, C. Kamaga, T. Kunitake, T. Ishihara and M. Shimomura, *Adv. Mater.*, 2007, **19**, 3229-3232.

39. K. Y. Suh, Y. S. Kim and H. H. Lee, *Adv. Mater.*, 2001, **13**, 1386-1389.

40. Y. Zhang, C. T. Lin and S. Yang, *Small*, 2010, **6**, 768-775.

41. J. M. Torres, C. M. Stafford and B. D. Vogt, *Soft Matter*, 2012, **8**, 5225-5232.

42. M. Gaudet, J. C. Camart, L. Buchaillot and S. Arscott, *Appl. Phys. Lett.*, 2006, **88**, 024107.

43. M. Jamal, A. M. Zarafshar and D. H. Gracias, *Nat. Commun.*, 2011, **2**, 527.

44. S. Keller, G. Blagoi, M. Lillemose, D. Haefliger and A. Boisen, *J. Micromech. Microeng.*, 2008, **18**, 125020.

45. T. Tanaka, S. T. Sun, Y. Hirokawa, S. Katayama, J. Kucera, Y. Hirose and T. Amiya, *Nature*, 1987, **325**, 796-798.

46. D. Lee, N. Triantafylldis, J. R. Barber and M. D. Thouless, *J. Mech. Phys. Solids*, 2008, **56**, 858-868.

47. N. J. Huffington, *J. Appl. Mech.*, 1956, **23**, 15-20.

48. J. Groenewold, *Physica A*, 2001, **298**, 32-45.

49. R. Huang and S. H. Im, *Phys. Rev. E*, 2006, **74**, 026214.

50. P. Kim, M. Abkarian and H. A. Stone, *Nat. Mater.*, 2011, **10**, 952-957.

51. Y. Ebata, A. B. Croll and A. J. Crosby, *Soft Matter*, 2012, **8**, 9086-9091.

52. J. F. Zang, X. H. Zhao, Y. P. Cao and J. W. Hutchinson, *J. Mech. Phys. Solids*, 2012, **60**, 1265-1279.

Chapter 3

Buckling-based strong dry adhesives via interlocking

3.1 Introduction

Adhesion between polymers plays an important role in a wide range of industrial applications, including electronic packaging and automotive and airplane assemblies. Compared to liquid based adhesives, dry adhesives as manifested in gecko foot hairs are attractive because they require no liquid handling or lengthy curing during the adhesive attachment and the adhesion strength can be rapidly switched. The ability of gecko to cling on almost any surface is attributed to the split contact adhesion resulting from millions of hierarchical fibrillar structures on its toe pads via the weak non-covalent van der Waals force and/or capillary forces.[1-3] Specifically, it has been shown that the directional tilt of the fibrillars and a lateral friction force play the critical role in the gecko's articulation of attachment and detachment.[4-6] High net friction and adhesion forces are obtained at small pulling angles between the spatulae and the substrate. For detachment, the spatulae are peeled off perpendicularly from the substrate, leading to reduction of adhesion and friction force over three orders of magnitude. There have been numerous attempts to fabricate synthetic gecko-like adhesives with fibrillar architectures of variable size, shape and tip geometry as well as different degree of tilting of the fibrillar structures.[7-20]

In comparison, dry adhesives based on collective mechanical interlocking forces, such as those exhibited in the Burdock seeds with many small hooks and loops, have received relatively less attention until recently. The discovery of the interlocking

mechanism in Burdock seeds led to the invention of Velcro® tape,[21, 22] which could have a very large adhesion strength (~ 120 N/cm^2) [23] to hold a person and automotive body parts using the Velcro® tape. This is because any force pulling the hooks/loops apart is spread evenly across all hooks and the strength of the bond depends on how well the hooks are embedded in the loops. Different from gecko adhesion, when a force is applied in the normal direction or pulled in a direction parallel to the plane of the Velcro® surface, more hooks and loops are engaged, thus, adhesion strength increases.

Insects such as beetle and dragonfly employ similar type of interlocking adhesion mechanisms.[24] Many beetles have arrays of protrusions on their elytra and wings. These features attach the elytron to the wing when the beetle is at rest, offering the resistance to be sheared and preserving the easiness of spanning the wings.[25, 26] A certain species of dragonflies has tapered cuticles on the head and the neck to lock the head in place by friction during feeding or tandem flight.[25, 27]

Recently, several groups have begun to investigate adhesion between two structured surfaces, including identical random nanowires,[28, 29] and periodic arrays of high-aspect-ratio polymers pillars,[26] and complementary ripples.[30, 31] The interlocked nanowires and pillars show highly anisotropic adhesion, where the shear adhesion is much larger than the normal adhesion. This is because the engagement and alignment of nanowires/pillars in the shear motion promotes the contact area between them. In the case of periodic polymer pillar array imitating the beetle wing structures, the adhesion is anisotropic[26, 32] and preload dependent.[33] The adhesion also increases monotonically with pillar aspect ratio.[26] In a separate vein, McMeeking and coworkers developed a theoretical model for a friction-based fastener, mimicking the dragonfly head arrester. Such fastener is expected

to achieve an adhesion strength that is ~ 30% of the tensile strength of the material.[27] However, in reality, engaging such adhesives would be difficult and could be further complicated by structural buckling.[27] So far, researchers have attempted to avoid buckling and collapse of the pillars in the adhesion study using well-ordered pillars as model systems since buckling and collapsing of the pillars will complicate the interpretation of the pillar-pillar contact, not to mention that it will be very difficult to image such interface.[26, 27, 34, 35] However, instability exists commonly in bioorganisms, and practical samples. Therefore, it will be critically important to understand the impact of buckling of the pillars at the interface, specifically, to the interlocking adhesion strength.

Here, we demonstrated a strong dry adhesive through interlocking of two complimentary sets of buckled shape memory polymer (SMP) pillar arrays above the glass transition temperature (T_g, 60 ^oC) under a load. When engaged at 80 ^oC, the SMP pillars became rubbery; they interweaved and/or indented with each other at a preload larger than the critical buckling threshold. After cooling down to room temperature, the interlocked pillars were fixed in a glassy state. It required strong forces at room temperature to separate the two pillar surfaces, ~ 53.6 ± 25.1 N/cm^2 in the normal direction and ~ 71.9 ± 23.2 N/cm^2 in the shear direction for cylindrical pillars in a hexagonal lattice (1 μm diameter, spacing 1 μm, and aspect ratio 4). Both adhesion values were much larger than the corresponding adhesion from a pillar-to-flat surface contact (12.3 ± 8.8 N/cm^2, normal, and 15.0 ± 2.3 N/cm^2, shear) and a flat-to-flat surface contact (7.1 ± 5.0N/cm^2, normal, and 15.8 ± 2.0N/cm^2, shear). Despite the strong adhesion exhibited by the interlocked pillars, the two pillared surfaces could be easily separated by

reheating to 80 ^{o}C through the release of the elastic energy stored in the deformed (i.e. buckled) state. Further, we showed that the adhesion could be tuned by varying the pillar spacing. By comparing the experimental results with theoretical calculation and finite element simulation, we elucidated the buckling based interlocking adhesion mechanisms.

3.2 Experimental methods

3.2.1 Materials and fabrication

The PDMS mold was prepared from the Si master, which was treated with (tridecafluoro-1, 1, 2, 2-tetrahydrooctyl)trichlorosilane (Gelest Inc.) under vacuum. The degassed liquid PDMS prepolymer mixture (10:1 weight ratio, Sylgard 184, Dow Corning) was poured over the patterned Si wafer and cured at 65 ^{o}C for 4 hours, after which the PDMS mold was carefully peeled off from the Si master.

The SMP precursors, bisphenol A diglycidyl ether (BADGE), poly(propylene glycol) bis(2-aminopropyl ether) (Jeffamine D230) and decylamine (DA) were purchased from Sigma Aldrich. The SMP adhesive was prepared following a similar formulation reported in literature.[36] Briefly, BADGE, Jeffamine D230 and DA were mixed at a molar ratio of 4 : 1 : 2. The mixture was then degassed by ultrasonication for 1 h, subsequently poured onto a PDMS mold, and thermally cured (100 °C for 1.5 h and 130 °C for 1 h). After cooling to room temperature, the cured SMP was carefully separated from the PDMS mold by peeling and the sample was cut into 1 - 2 cm^2. For bonding, two identical pillared SMP surfaces were pressed together at a preload of ~ 24 N/cm^2 at 80 °C for 1 min, followed by cooling under the load.

3.2.2 Characterizations

The T_g of the SMP was characterized using TA Q2000 differential scanning calorimeter (DSC) at a heating rate of 1 °C/min in nitrogen and TA Q800 dynamic mechanical analysis (DMA) at 1 Hz, 0.2% strain and a heating rate of 1 °C/min in nitrogen under "multifrequency, strain'' mode.

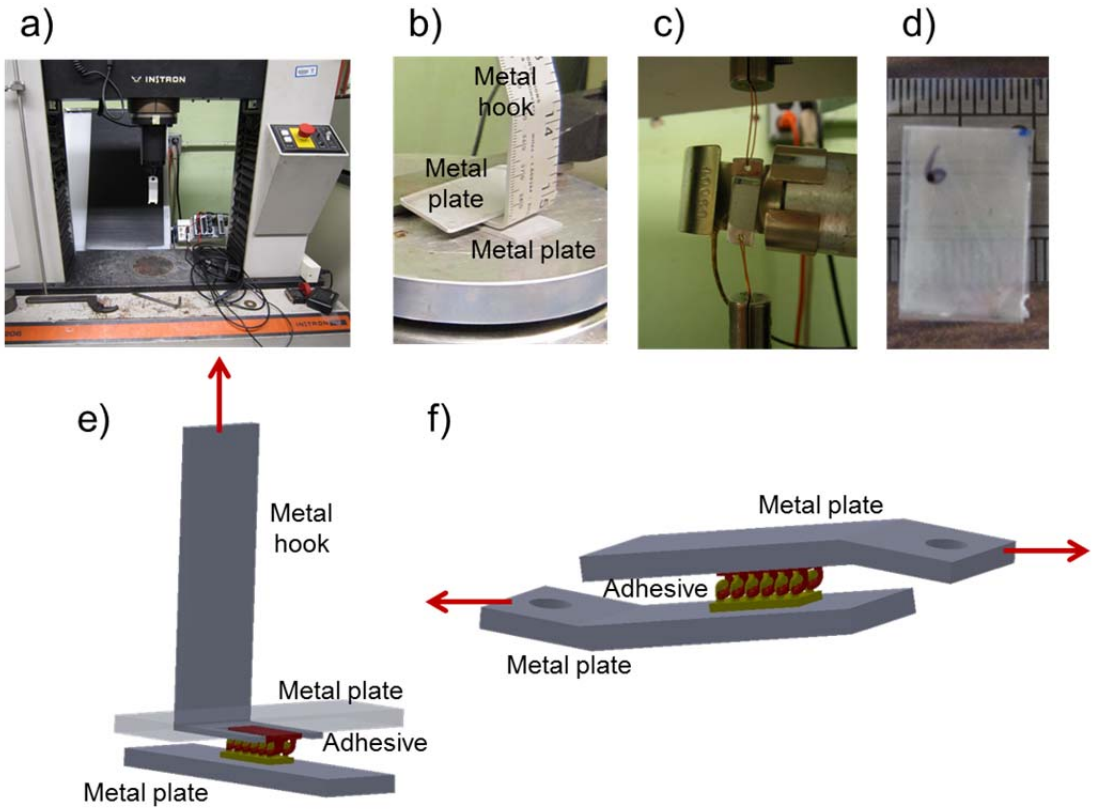

Figure 3.1 Adhesion test setup. (a) The adhesion tester, modified from universal testing machine, Instron 4206. (b-c) The normal adhesion test setup with temperature-controlling capability. (d) The engaged two sets of SMP pillars, appearing opaque due to the buckled pillars. (e) Schematic of the normal adhesion test. (f) Schematic of the shear adhesion test.

The adhesion tests were carried out using Instron 4206 universal testing machine (UTM). The home-made sample holders for normal and shear adhesion were attached to the load cell bearing a maximum load of 100 N (see Figure 3.1). In a typical test, the

crosshead moved at a speed of 0.02 in/min until the adhesion failure. The corresponding load-displacement data were collected using LabView (National Instruments). For adhesion test performed at 80 °C, the temperature was controlled using a hot plate or a heating gun equipped with temperature feedback control in the normal or shear adhesion tests, respectively. For all the temperature-dependent experiments, the samples were equilibrated at the designated temperature for at least 5 minutes.

The room temperature stress-strain curve of SMP was obtained using an Instron 4206. The load cell was 2.5 kN and the crosshead speed was 0.02 in/min. The stress-strain at 80 °C curve was recorded using TA Q800 DMA. The SMPs were equilibrated at 80 °C for 5 min, then stretched at a strain rate of 5%/min till reaching 5% strain. The Young's moduli of the SMP were determined from the linear portion of the corresponding stress-strain curves.

The adhesive surfaces separated by the UTM tests were examined using FEI Quanta FEG ESEM and FEI Strata DE235 scanning electron microscopes (SEM) at an accelerating voltage of 5 kV.

3.2.3 Finite element simulation

The single pillar pair and multiple pillar interaction models were meshed by 50424 and 4715 eight nodes hexahedral elements C3D8R per pillar, respectively. These later models were calculated by Abaqus/Explicit. The simulation was performed using Simulia Abaqus 6.10-1. The bent pillar model was constructed using 120776 four nodes tetrahedral elements C3D4. This model was analyzed by Abaqus/Standard.

3.3 Criterion and interactions for SMP pillar-pillar contact

It is known that adhesion between materials is mediated by their surface or near-surface properties, including 1) local chemistry to affect intrinsic adhesion at the molecular level, 2) microscopic surface roughness (topography), 3) macroscopic materials mechanical properties (compliance), and 4) the effective contact, which is dependent on the magnitude and type of the loading applied to the surface. In the past decade many gecko-inspired dry adhesives have been fabricated, which almost exclusively exploit the surface geometric effect for adhesion enhancement. Few have explored manipulation of materials intrinsic properties, including local chemistry at the molecular level,[37, 38] and tunable bulk modulus.[12, 39, 40] It has been shown that interlocking between identical or complementary structured surfaces could offer strong and anisotropic adhesion.[26, 28, 29, 41] However, detailed insights of the interfacial interaction between two sets of microstructured surfaces, its dependence of geometry and bulk modulus, and the resulting macroscopic adhesive properties remain lacking in the literature.

SMPs are materials that can memorize temporary shapes and recover to their permanent shape upon exposure to an external stimulus, such as heat, light, and solvent.[42-44] The "permanent" shape is typically achieved by chemical or physical crosslinking. Above a thermal phase transition temperature, either a T_g or a melting transition temperature (T_m), the polymers can be deformed. Upon cooling, the deformed "temporary" shape can be fixed. Near the shape memory transition, an SMP changes from the glassy state to the rubbery state with 2-3 orders of magnitude change of the elastic modulus. The low modulus at the rubbery state facilitates intimate interfacial contact between two opposing surfaces for bonding, whereas the high modulus at the

glassy state favors high adhesion in the bonded state. The entropic energy stored in the deformed state can be later released on demand in the shape recovery process to trigger automatic debonding. Recently, SMPs have been used in micropillars (~ 10 μm in diameter) to thermally control gecko-like dry adhesion, that is, contact between pillar and flat surface, by coating a thin adhesive layer on the tips of SMP micropillars[40] or directly patterning SMP in pillars.[12] Both studies showed that temperature played a key role to tune the bulk materials stiffness and the effective contact through deformation or tilting of the pillars.

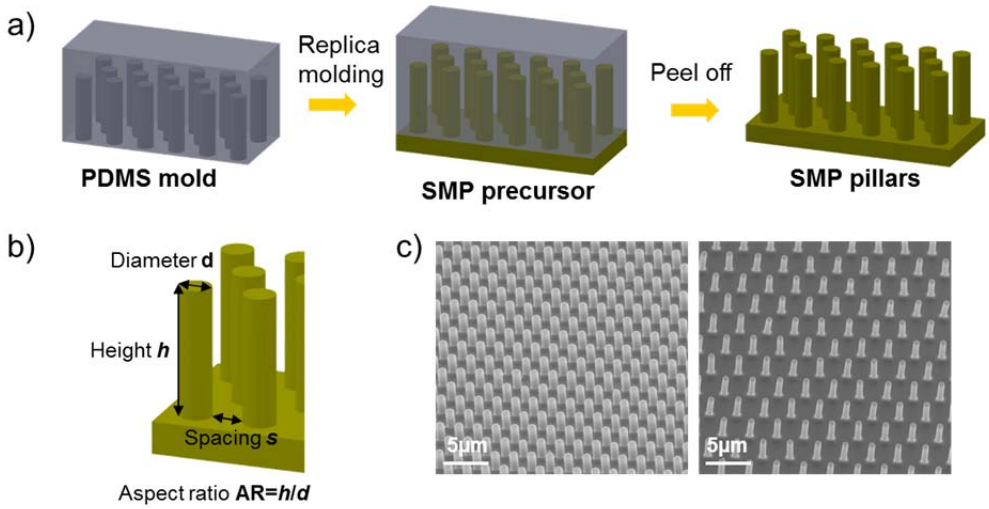

Figure 3.2 Fabrication of shape memory polymer pillars via replica molding. a) Schematics of the fabrication process. b) Characteristics of pillars. c) SEM images of SMP pillar arrays in a hexagonal lattice with d = 1 μm, s = 1 μm (left) and 2 μm (right), and AR = h/d = 4.

We are interested in interlocking adhesion through pillar-pillar contact and tuning the effective modulus of the SMP pillars at different temperatures for controlled bonding and debonding, specifically, how buckling of the pillars could impact their interfacial interactions. Utilizing replica molding (Figure 3.2), we fabricated cylindrical SMP

micropillars in a hexagonal lattice with pillar diameter of 1 μm and aspect ratio (AR = height/diameter, h/d) of 4. The pillar-to-pillar spacing was varied as 1 μm and 2 μm. Here, the SMP was epoxy based from diglycidyl ether of bisphenol A epoxy monomer (BADGE), poly(propylene glycol)bis(2-aminopropyl) ether (Jaffamine D-230) and decylamine (DA) (see Figure 3.3). The BADGE, Jeffamine D230 and DA were mixed in a molar ratio of 4 : 1 : 2 to obtain an SMP with T_g of 60°C. Dynamic mechanical analysis (DMA) showed that the storage modulus dropped approximately 3 orders of magnitude, from 2.5 GPa at 22 °C (glassy state) to 3.6 MPa at 80 °C (rubbery state, Figure 3.3b). Likewise, the tensile modulus was found to drop from 2.2 GPa at 22 °C to 3.1 MPa at 80 °C.

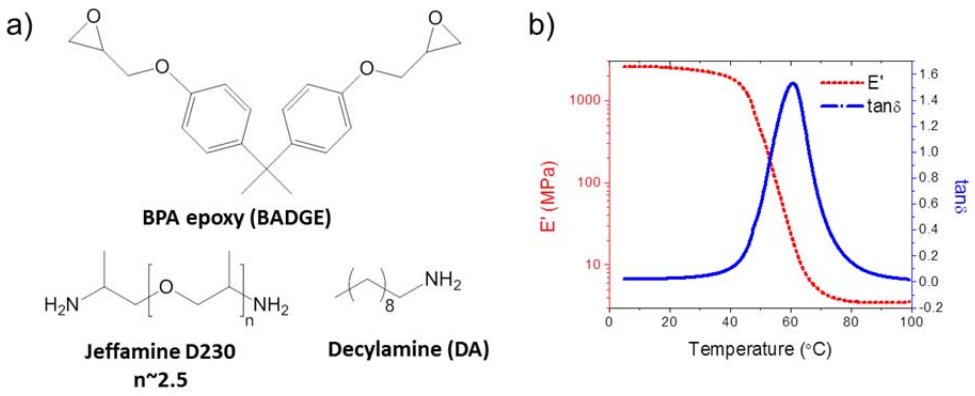

Figure 3.3 Shape memory polymer composition and thermomechanical properties. (a) Chemical structures of the ingredients. (b) Storage modulus (E') and loss tangent (tanδ) as a function of temperature measured by dynamic mechanical analysis. T_g is ~ 60 °C from the mixture of bisphenol A diglycidyl ether, Jeffamine D230 and decylamine in a molar ratio of 4 : 1 : 2.

Two sets of identical pillars were pressed against each other at 80°C under a preload. Under this condition, the pillars were softened and deformed. While maintaining the load, the pillars were cooled down to room temperature to fix the deformed states of the pillars

(see Figure 3.4a). This completed the bonding process. The adhesion forces were measured in the normal and shear directions at both 80 ^{o}C and room temperature to study temperature dependent detachment (see the setup for macroscopic adhesion measurement in Figure 3.1). The results were compared to those from pillar-to-flat and flat-to-flat samples to evaluate the enhancement of dry adhesion strength and anisotropy by the interlocking mechanism.

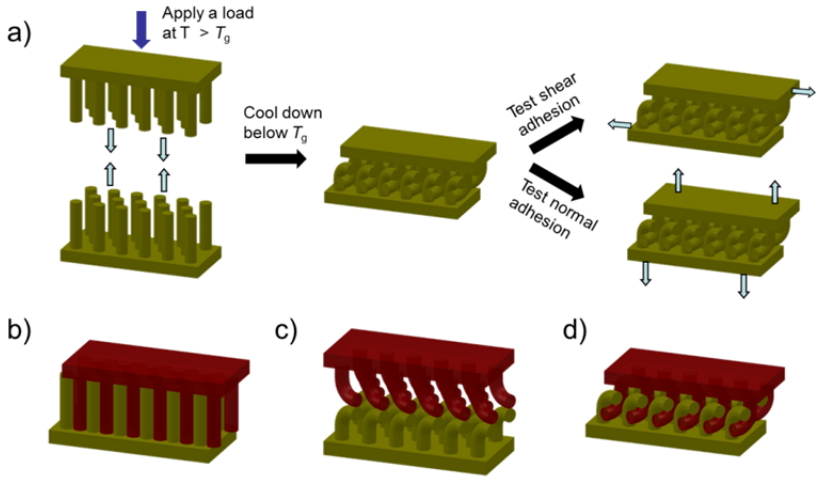

Figure 3.4 (a) Illustration of engaging pillar-to-pillar contact and adhesion measurement. (b-d) Three possible interlocking modes between two sets of identical SMP pillar arrays. (b) Interdigitation. (c) Indenting. (d) Interweaving.

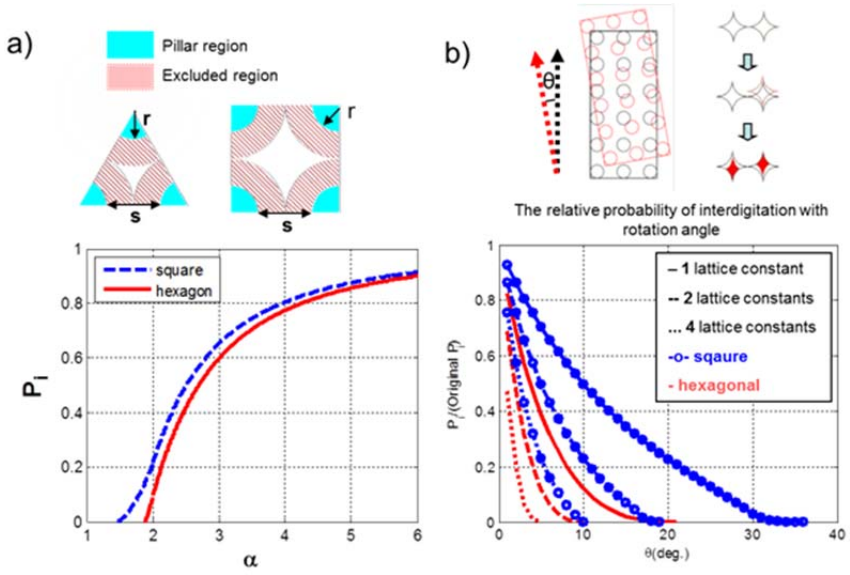

Figure 3.5 Estimation of the probability of interdigitaion for pillar-to-pillar contact. (a) robability of pillar interdigitation without relative rotation. (b) Relative probability of pillar interdigitation with a rotation angle θ.

There are three possible scenarios of pillar-to-pillar contact: 1) interdigitation, 2) indenting, and 3) interweaving (see Figure 3.4b-d). When the preload is small, the pillars remain straight and can interdigitate with pillars from the other set of sample (Figure 3.4b). In this case, the adhesion could be amplified by increasing the effective contact area as demonstrated by Suh and coworkers.[26] The possibility of interdigitation, however, as we show below is limited by pillar geometry. Here, a spacing parameter α is introduced as

$$\alpha = 1 + \frac{s}{d} \tag{3.1}$$

where d is the pillar diameter and s is the spacing between pillars (see definition in Figure 3.2c). Considering two pillar arrays to interact with each other with only translational

degree of freedom (no relative rotation), the probability of interdigitation, P_i, for a hexagonal lattice is dependent solely on α,

$$P_i = \left(1 - \frac{2\pi}{\sqrt{3}\alpha^2}\right) - \frac{3}{\alpha^2}\cos^{-1}\left(\frac{\alpha}{2}\right) - \frac{3}{2\alpha}\sin\left[\cos^{-1}\left(\frac{\alpha}{2}\right)\right] \quad (3.2)$$

for $2 > \alpha \geq \sqrt{3}$, and

$$P_i = 1 - \frac{2\pi}{\sqrt{3}\alpha^2} \quad (3.3)$$

for $\alpha \geq 2$.

For $\alpha < \sqrt{3}$, the interdigitation does not occur. In our system, for α = 2 (s = 1 μm) and α = 3 (s = 2 μm), P_i = 9.31% and 59.69%, respectively (Figure 3.5a). These values explain why the interdigitation can be achieved in the system reported by Pang *et al*., which has α = 3.[26] For pillars with α = 2 in our system, the geometrical interdigitaion is highly unlikely, especially when the relative rotation is involved, which is difficult to avoid experimentally (Figure 3.5b).

In the other extreme, as $\alpha \sim \sqrt{3}$, McMeeking *et al*. showed that it was possible to have a strong frictional adhesion comparable to the tensile strength of the material. It is, however, very difficult to engage the pillar in the first place, which is further complicated by the elastic buckling of the pillars. For a circular pillar, the critical buckling stress σ_{cr} can be calculated by fixing one end of the pillar to the substrate and pinning the tip as the boundary conditions by assuming the frictional force generated due to contact with the substrate that restricts the horizontal displacement of the pillar tip, [45, 46]

$$\sigma_{cr} = \frac{20.19E}{16AR^2} \tag{3.4a}$$

where E is the elastic modulus of the pillar. On the other hand, the boundary condition between two pillar tips can be approximated as free ends. The critical buckling stress then becomes,[46]

$$\sigma_{cr} = \frac{\pi^2 E}{64AR^2} \tag{3.4b}$$

First, the two sets of pillars were brought into contact at 80 °C in the rubbery state at an apparent preload of 24 N/cm^2. When normalized by the pillar areal density, the effective preload became 1.06 MPa for α = 2 and 2.38 MPa for α = 3 pillars, well above the buckling threshold (σ_{cr} is 0.25 MPa from Equation 3.4a or 0.03 MPa from Equation 3.4b). Therefore, the softened pillars would be bent and collapsed against each other at 80 °C, leading to indentation (see Figure 3.4c) and/or interweaving much like weaved yarns (see Figure 3.4d). As seen in Figure 3.6, both modes of pillar-to-pillar contact were experimentally observed. It is intriguing how the pillar-to-pillar interactions will affect the effective adhesion force and anisotropy in comparison to the pillar-to-flat and flat-flat configurations, and whether it is possible to detach them on demand.

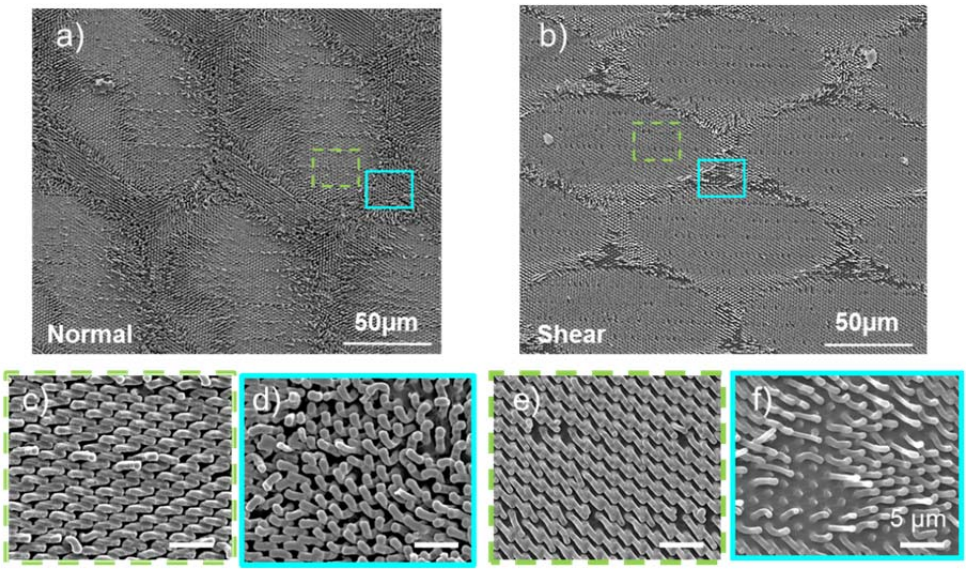

Figure 3.6 SEM images of indented and interweaved pillars after being engaged at 80 °C and subsequently separated at room temperature in the normal separation direction (a) and shear separation direction (b). (c-d) and (e-f) are corresponding higher magnified areas. c and e: indented pillars. d and f: interweaved pillars. (c-f) Scale bars: 5 μm.

Moiré patterns, which are commonly formed when two or more geometrically regular patterns are superimposed,[47] were observed after separating the interlocked pillar arrays (see Figure 3.6a and 3.6b). Recently Kang *et al*. also reported Moiré patterns when evaporating water sandwiched between two periodic pillar surface.[48] As seen in Figure 3.7, when the relative rotation angle between two compressed pillar array reaches 10°, Moiré pattern is formed with a characteristic period, which decreases as the rotation angle increases. A closer look of the Moiré pattern from 10°-rotation in Figure 3.7 suggests that there are different degrees of mismatch between pillar pairs depending on whether the pillar tips are in contact with the counter surface. Presumably, the predominant mode of interaction between two contacting pillars would be indenting as they buckle and deform together in response to the load. However, it is very difficult to directly image the pillar-to-pillar contact geometry at the interface at different contact stages as the pillars were

interweaved or indented to each other. To better understand the contact process, we used Abaqus finite element analysis (FEA) to simulate the interaction between a pair of pillars, which were then compared to the SEM images of the separated pillars after engagement. The pillar pairs were slightly misaligned at the beginning near the tips, under a load at 80^{o}C (Figure 3.8). Above T_g, when the load was greater than the buckling threshold, the pillars were deformed and pushed against each other since the initial contact started at the tips. At the final stage of the deformation, the pillars became indented to each other. In contrast, when pillars were completely mismatched with each other at the beginning, the primary mode of pillar-to-pillar contact would be interweaving since the pillars would not buckle until they became interdigitated and sliding against each other while they might or might not reach the bottom surface of the counter pillars.

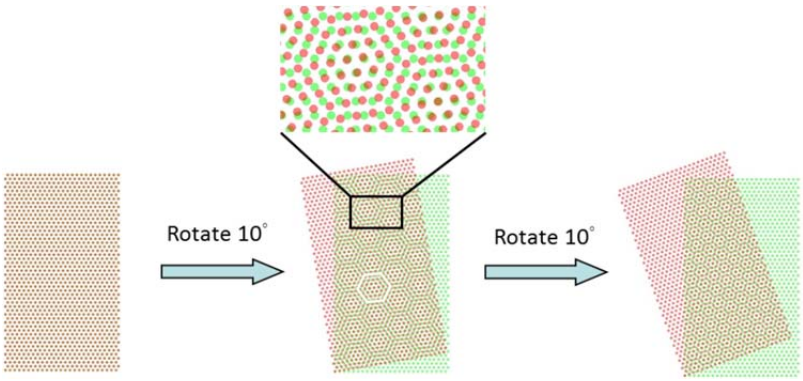

Figure 3.7 Schematic illustration of Moiré pattern formation by stepwise rotation.

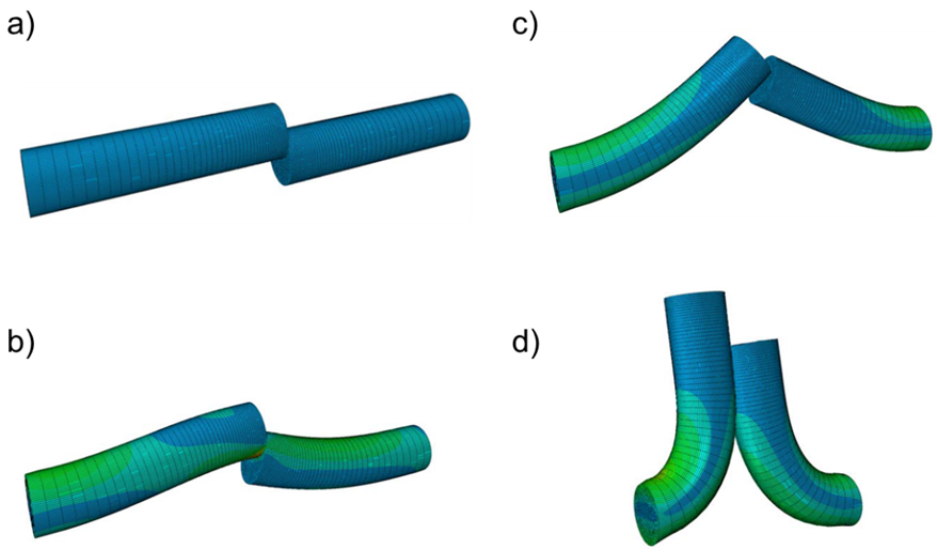

Figure 3.8 Finite element simulation of the contact process between a pair of pillars under load at 80 ^{o}C using Abaqus 6.10-1. The pillars pair is originally in a partially misaligned state (a). One side of the pillar is compressed and deformed toward the other pillar by apply a ramping displacement (b), (c) and reaching the final state (d).

To capture the collective behavior of multiple pillars at the pillar-pillar interface, we then simulated the contact process of pillars in a hexagonal array (Figure 3.9) with the same degree of misalignment as the one seen in Figure 3.8 with an additional rotation of 10°. This rotation is exaggerated comparing to the experimental condition where relative rotation < 3° is normally observed. This is so chosen to account for the relative small pillar array in the simulation of multiple pillars comparing to the real macroscopic sample. The interaction was found anti-symmetric at the beginning until reaching the point where multiple pillars were interacting with each other. The contact process is much more complex than that from a single pair. This is because when the symmetry of the pillar array is broken upon buckling, the pillars could slide and enter the open spaces available on the other set of the pillar array. Finally, when the pillars were totally collapsed, both interweaving (Figure 3.9d) and indenting (Figure 3.9e and 3.9f) pillars

were observed in simulation, which agreed well with experimental results shown in Figure 3.6. Indented pillars were often observed in the region with more pillar-to-pillar contact (by comparison of SEM images with simulated Moiré pattern in Figure 3.7), whereas interweaved pillars appeared in the region with less pillar-to-pillar contact. This can be further visualized from the pillar base mapping of Figure 3.9c (Figure 3.9d) that the pillar pairs with large fraction of overlapping base area primarily result in pillar indenting. Interestingly, Figure 3.9c also suggested that the pillar pairs bent as a result of indenting can also interweave with other neighboring pillars. The highly angle-dependent morphology could potentially contribute to a relatively large deviation in the adhesion force measurement, which we will discuss in detail later.

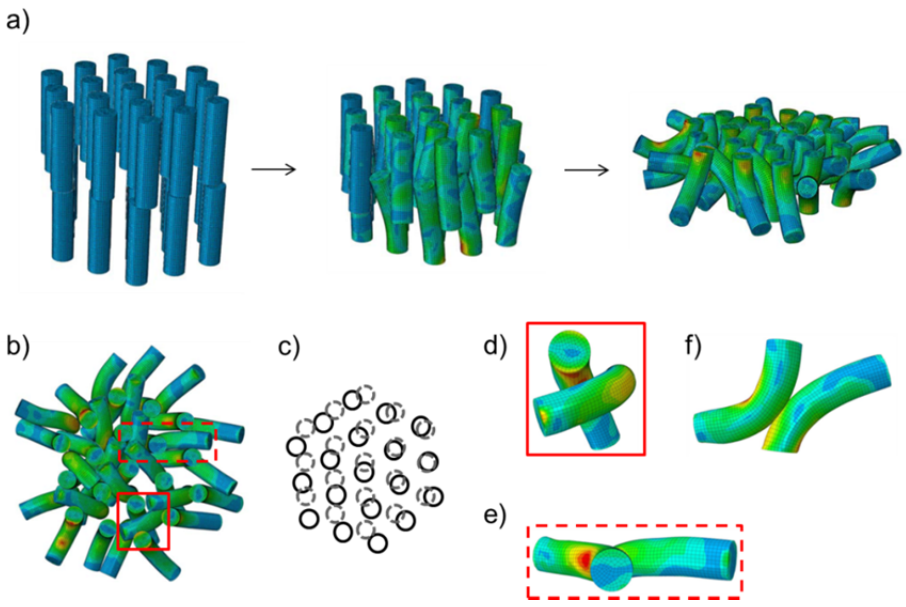

Figure 3.9 Finite element simulation of the contact process between two sets of pillars in a hexagonal array. (a) The collapsing process of the compressed pillars. (b) Bird's eye view of the fully compressed pillar arrays. (c) The mapping of two sets of interacting pillar bases, showing the relative position of pillars. Solid circles represent the set of bases directly observable in (b). The dashed circles represent the set underneath. The interweaved (d) and indented (e) pillars. (f) The side view of (e).

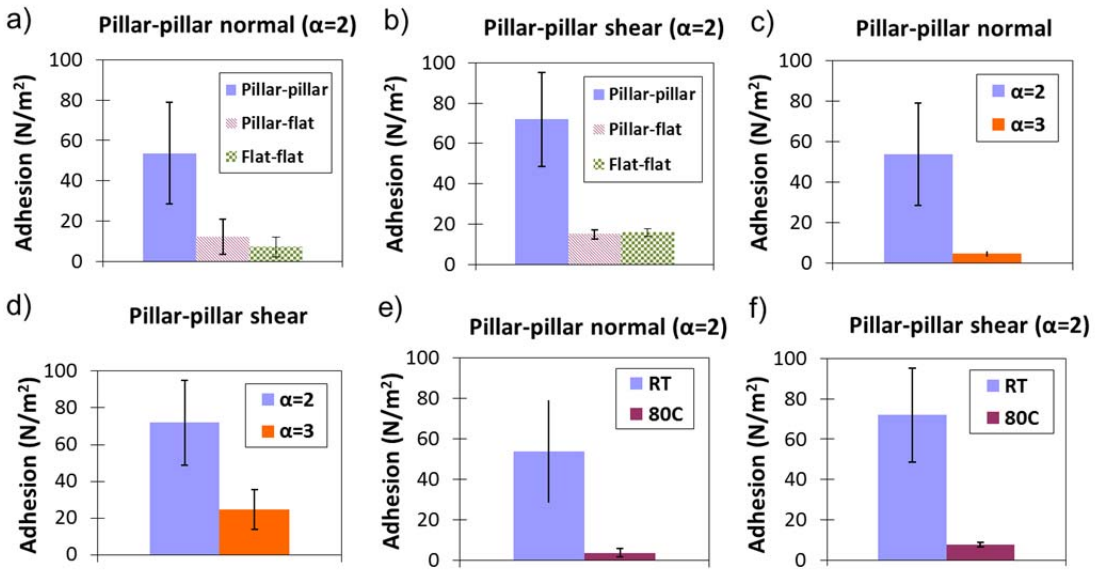

Figure 3.10 Measured pull-off force between two sets of hexagonal arrays of SMP pillars. (a) The normal adhesion of α = 2 (1μm diameter, spacing 1 μm), aspect ratio 4 samples separated at room temperature in comparison to those from the pillar-to-flat and the flat-to-flat samples . (b) The comparison for shear adhesion of the pillar-to-pillar, the pillar-to-flat and the flat-to-flat samples separated at room temperature. (c) The pillar-to-pillar normal adhesion force of α = 2 and α = 3 (1μm diameter, spacing 2 μm) samples separated at room temperature. (d) The pillar-to-pillar shear adhesion force of α = 2 and α = 3 samples separated at room temperature. (e) The normal adhesion force for α = 2 samples separated at different temperatures. (f) The shear adhesion for α = 2 samples separated at different temperatures.

3.4 Adhesion strength and theoretical analysis for SMP pillars

After the preload at an elevated temperature, the interlocked samples were cooled down quickly to room temperature to lock the structure. Upon cooling, the elastic modulus increased dramatically back to 2.5 GPa (storage modulus) and 2.2 GPa (tensile modulus), respectively. The interlocked pillars will resist any deformation for separation and we should expect a large adhesion force. As a comparison, samples were also prepared under the same preload and temperature cycle by pressing a SMP pillar array against a flat SMP (pillar-to-flat) or pressing two flat SMP films (flat-to-flat) together. Indeed, as shown in Figure 3.10a and 3.10b, the pillar-to-pillar ($\alpha = 2$) adhesion measured

at room temperature was 53.6 ± 25.1 N/cm^2 in the normal direction and 71.9 ± 23.2 N/cm^2 in the shear direction. These adhesion values were significantly larger than those from either the pillar-to-flat (12.3 ± 8.8 N/cm^2, normal and 15.0 ± 2.3 N/cm^2, shear)), or from the flat-to-flat samples (7.1 ± 5.0 N/cm^2, normal and 15.8 ± 2.0 N/cm^2, shear).

In the case of the interweaved pillars, the difference between the normal and shear adhesion would be dependent on the lever arm of bending. Using Castigliano's first theorem,[49] the normal force P required to separate a single pair of interweaved pillars is

$$P = \frac{\delta^P EI}{\left(\frac{L_2^3}{3} + \frac{\pi L_2^2 R}{2} + L_2^2 L_1 + 2L_2 R^2 + 2RL_1 L_2 + R^2 L_1 + \frac{\pi R^3}{4} \right)} \qquad (3.5)$$

where δ^p is the deflection in the normal direction, I is the area moment of inertia, L_1, L_2 and R are the base length, arm length and the bent radius, respectively (Figure 3.11a). For shear force S to separate the interweaved pair of pillars, it is given by

$$S = \frac{3\delta^S EI}{L_1^3} \qquad (3.6)$$

where δ^S is the deflection in the shear direction (Figure 3.11a).

Based on Equations 3.5 and 3.6 and assuming L_1 = 1 μm, L_2 = 1 μm, R = 1 μm and the deflections $\delta^p = \delta^S$ = 1.5 μm, we obtained P = 538 N/cm^2 and S = 9,352 N/cm^2 after normalized by the area occupied by the pillars. Compared to the normalized ultimate tensile stress of the polymer (~ 893 N/cm^2), it is expected that pillars should fracture easily in the shear test. Simulation (Figure 3.12) suggested that the stress could be concentrated at the pillar base, and more so in the shear force. Here, the interaction force

was set as a point load equal to the averaged experimental adhesion force/area. In agreement with the simulation, experimentally we did find fractured pillars in the interweaved regions for both normal and shear force of separation, but more apparent in the later (see Figure 3.6d vs. 3.6f).

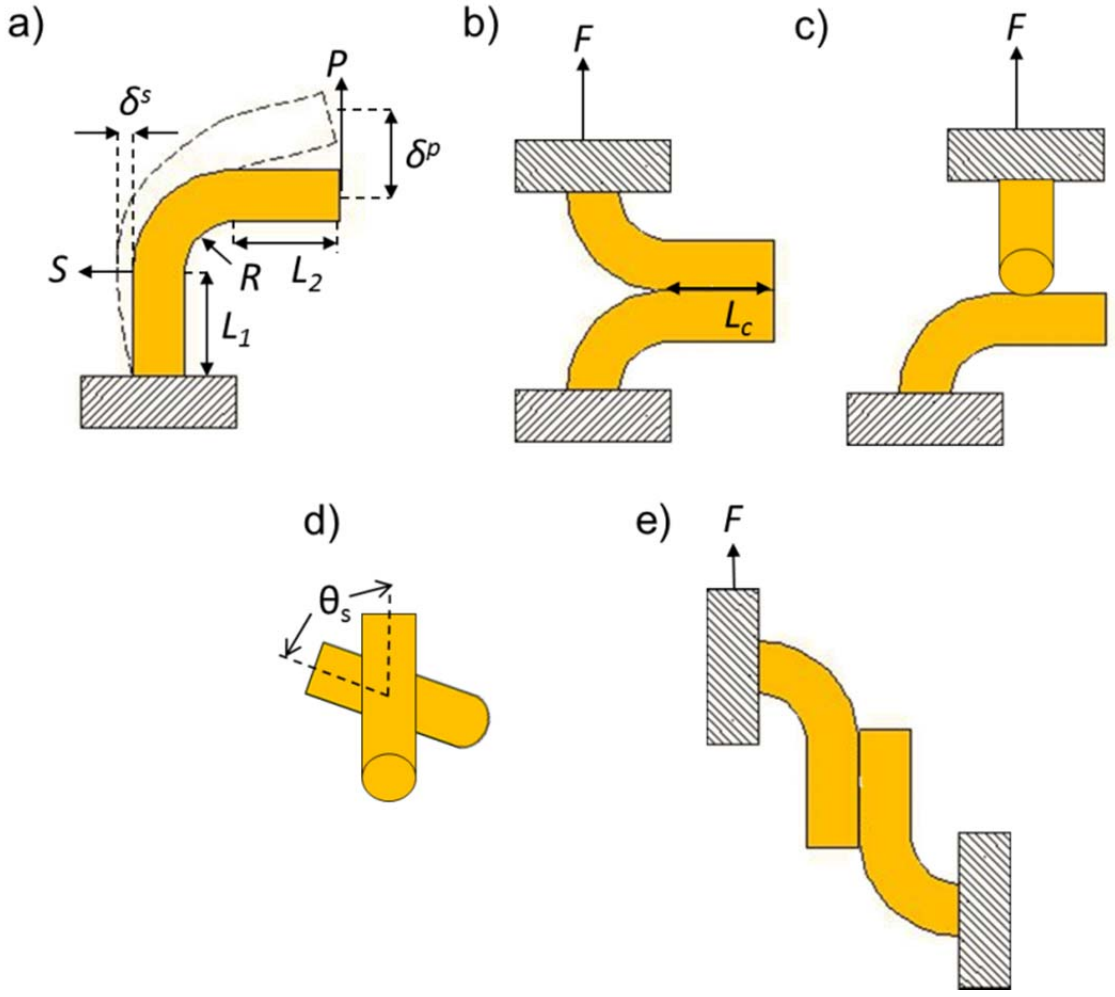

Figure 3.11 (a) Model for interweaved pillars, (b) Model of separating pillars indented in parallel by a normal force, (c) Model of separating perpendicularly indented pillars by a normal force. (d) Horizontal skew angle, θ_s, of the indented pillars, $\theta_s = 0$, pillars are parallel to each other and $\theta_s = 90°$, pillars are perpendicular to each other. e) Model of indented pillars separated by shearing.

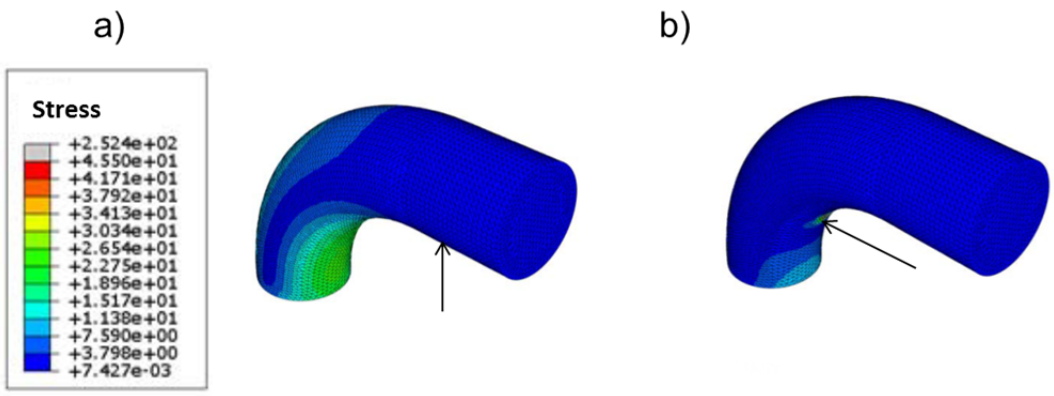

Figure 3.12 (a) Stress concentration at the base at the onset of separation of engaged pillars in the normal (a) and shear (b) directions. Arrow indicates the direction of force.

In the case of the indented pillars, the adhesion can be analyzed by contact mechanics models. Considering two extreme contacting scenarios between two cylinders, which are either in parallel (Figure 3.11b) or perpendicular (Figure 3.11c) configuration with each other under a normal pull-off force or sliding against each other under a shear force (Figure 3.11e). The adhesion between parallel-contacting cylinders can be formulated as:[50]

$$F = \left(\frac{\pi E W^3 d^2}{8\left(1-\upsilon^2\right)}\right)^{1/4}\left(\frac{L_c}{2}\right)^{3/4} \tag{3.7}$$

where L_c is the contact length, ~ 3 μm, W is the work of adhesion, 38 mJ/m, v is the Poisson's ratio, which equals to 0.45 for the SMP[51] (Figure 3.11b). After normalized by area, F = 18.3 N/cm^2. For perpendicular-contacting pillars (Figure 3.11c), the adhesion is equivalent to the sphere-on-the-flat configuration according to the JKR model[52]

$$F = \frac{3}{4}\pi W d \tag{3.8}$$

giving F = 2.6 N/cm^2 normalized by area. The actual adhesion should lie in-between the values given by Equations. 3.7 and 3.8, depending on the horizontal skew angle θ_s between the contacting pillars (Figure 3.11d).[53] For the shear adhesion, the classical Kendall's peeling model[54] is adapted for cylindrical pillars [19] (Figure 3.11e)

$$F = \sqrt{3}\left(\frac{\sqrt{\left(1-\upsilon^2\right)}\pi E d^4 W^2}{32}\right)^{1/3} \tag{3.9}$$

yielding F = 32.7 N/cm^2 normalized by area.

The measured adhesion values are in general much smaller than the calculated value for interweaved pillars but larger than the calculated value for indented pillars, as shown in Figure 3.10. This trend can be explained by 1) the actual contact was a mixture of interweaving and indenting modes. The calculation of interweaved pillars provided an upper limit for the adhesion, whereas the adhesion for indented pillars offered the lower end. 2) The calculated values were obtained from the ideal scenario of either interweaved or indented pillar pairs. In reality, the contact was mostly likely non-ideal, where L_1, L_2, R and contact geometry for the interweaved pillars and contact orientation for the indented pillars could be very different from pair to pair. Therefore, the actual normal adhesion for indented pillars should lie in between 2.6 to 18.3 N/cm^2. 3) The calculation assumed that the external load was evenly applied to all pillars. Experimentally, this could be hard to achieve, especially when the backing layer was rather thick (~ 1 - 2 mm), which would promote stress concentration, thus, drastically lowering the measured adhesion values.[55] Supporting this was that the measured pillar-to-flat normal adhesion (12.3 ± 8.8 N/cm^2) which was about half the calculated value from Equation 3.7 (25.8 N/cm^2), while the

shear adhesion (15.0 ± 2.3 N/cm^2) was ~ 5 times smaller than the theoretical value from Equation 3.9 (82.3 N/cm^2). Here, the effective diameter d in Equations 3.7 and 3.9 was slightly modified for pillar-to-flat configuration, where d is expressed by

$$\frac{1}{d} = \frac{1}{d_1} + \frac{1}{d_2} \tag{3.10}$$

Here, d_1 and d_2 are the diameters of contacting surfaces, respectively. For pillar-to-pillar contact, $d_1 = d_2$ and $d = d_1/2 = d_2/2$. For pillar-to-flat configuration, assuming d_1 is the diameter of the pillar, then $d = d_1$ and the effective diameter is therefore doubled.

Nevertheless, the calculated adhesion qualitatively agreed with the experimental results, that is, the interweaved pillars had a higher adhesion over the indented pillars as evident by the superior adhesion strength (both normal and shear) of the pillar-to-pillar samples compared to that from the pillar-to-flat samples. Further supporting this was that the calculated values for indented pillars were always smaller than the experimentally measured pillar-to-pillar adhesion. In the pillar-to-flat samples, the only mode of contact is the buckled SMP pillars indented to the flat SMP film, making cylinder-to-flat contact, which is equivalent to the parallel cylinder-to-cylinder contact in the pillar-to-pillar case.

The relatively large standard deviation in adhesion measurement reflects the significant effect of small misalignment between the two pillar substrates and variation in the pillar-to-pillar contact from batch to batch. Specifically, the normal adhesion measurement itself is very sensitive to any misalignment because of the stress concentration,[56] resulting in larger errors in general than the shear adhesion values as evident from Figure 3.10. In theoretical aspect, to better capture the behavior of the

concentrated load, fracture mechanics could be employed to understand the crack propagation process. On the other hand, measurement errors can be potentially minimized using a highly specialized instrument.[57, 58]

3.5 Tuning of the adhesion by geometry and temperature

We note that while the adhesion mechanism is completely different between gecko adhesion and Velcro adhesion, both are anisotropic, where attachment and detachment can be performed in a preferred direction. As we discussed above, the effective mode of the pillar-to-pillar contact at the interface is highly dependent on pillar geometry. Here, we quantify the adhesion anisotropy, ψ, as the ratio of shear to normal adhesion. When $\psi = 1$ the adhesion is isotropic. For $\alpha = 2$ pillars measured at room temperature, $\psi \sim 1.3$, close to isotropic regime. For $\alpha = 3$ pillars, the measured adhesion at room temperature is 4.5 ± 1.4 N/cm^2 in the normal and 24.6 ± 10.7 N/cm^2 in the shear separation, yielding a ψ value of ~ 5.4. This strong anisotropy is similar to those reported in literature from random nanowires[28] and a periodic array of tilted nanopillar system.[26] However, the origin of the anisotropy is totally different in our system, where the pillars are buckled. In the case of nanowires and well-separated, tilted nanopillars, the enhancement of the shear adhesion was attributed to the increased contact area in the shear direction. In our system, the adhesion strength is highly dependent on pillar geometry, whether the pillars are in contact or not, degree of contact, and how they make contacts with each other. As discussed earlier, since the interweaved pillars offer much higher adhesion strength than the indented ones, we examined the change of anisotropy in the interweaved pillars by increasing the pillar spacing. In the interweaved pillar regime, the decrease in normal adhesion when increasing spacing is mainly owing to the smaller areal density of the

pillars and the increase in effective lever arm for pillar deflection. When α increases from 2 to 3, the areal pillar density decreases by 56%, whereas the lateral average center to center distance (squals to $s + d$) between the interacting pillars rises by 50%. Therefore, if we recalculate the adhesion for $\alpha = 3$ sample, it is reasonable to assuming L_2 increases from 1 to 1.5 μm while all the other parameters are constant ($L_1 = 1$ μm, $R = 0.5$ μm and $\delta^p = \delta^S = 2$μm). Thus, the normal force would decrease dramatically from 538 N/cm^2 for $\alpha = 2$ pillars to 141 N/cm^2 for $\alpha = 3$ pillars normalized by the nominal areal pillar density. In experiments, the normal adhesion force was found decreased by more than an order of magnitude, from 53.6 ± 25.1 N/cm^2 for $\alpha = 2$ pillars to 4.5 ± 1.4 N/cm^2 to $\alpha = 3$ pillars (Figure 3.10c). This suggests that when increasing the spacing, the possibility of pillars interweaving with each other decreases, thus, decreasing the adhesion strength. In fact, the separated interface of $\alpha = 3$ pillars often showed random collapsed pillars (Figure 3.13) rather than the Moiré patterns observed from $\alpha = 2$ pillars, suggesting less interweaved pillars during pillar-to-pillar contact. However, the lever arm in the shear direction should be nearly negligible since it is related mainly to L_1, which does not depend on the pillar spacing. Therefore, the decreases in shear adhesion with increasing pillar spacing should scale linearly with areal pillar density. Following this simple argument, the shear adhesion should decrease by 56% from $\alpha = 2$ to $\alpha = 3$ as 32 N/cm^2 experimentally, close to the measured one, 24.6 ± 10.7 N/cm^2 (Figure 3.10d). A more accurate estimation could be obtained by adding the torsional contribution of L_2 lever arm, which was neglected in Equation 3.6. For the indented pillars, the primary contribution is the decrease in effective contact area, which again would be decreased by 56%. Recall that for $\alpha = 2$ samples, the measured average pillar-to-flat normal and shear adhesion

forces were 12.3 ± 8.8 N/cm^2 and 15.0 ± 2.3 N/cm^2, respectively. For α = 3 samples, if considering the sole contribution from the reduction in effective contact area, the pillar-to-flat adhesion should decrease to ~ 5.5 N/cm^2 and ~ 6.7 N/cm^2 in the normal and shear directions, respectively. Experimentally, the values were 4.1 ± 2.8 N/cm^2 and 10.3 ± 4.9 N/cm^2 in the normal and shear directions for α = 3 samples, close to the predicted values. Clearly, the increase of adhesion anisotropy originated primarily from the interweaved pillars.

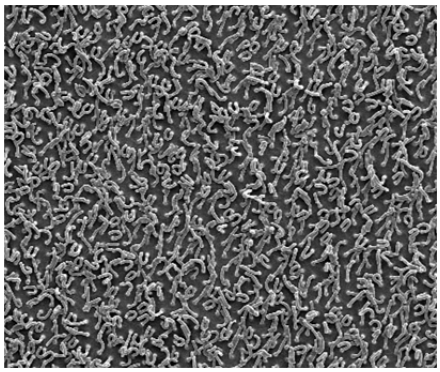

Figure 3.13 SEM image of randomly collapsed α = 3 pillars after separated from the adhesion state at 80 ^{o}C.

Another desirable characteristic of dry adhesives is the easy detachment on demand. As shown in Figure 3.10e and 3.10f, both the normal and shear adhesion dropped by an order of magnitude, from 53.6 ± 25.1 N/cm^2 to 3.6 ± 2.1 N/cm^2 and from 71.9 ± 23.2 N/cm^2 to 7.7 ± 1.0 N/cm^2, respectively, for α = 2 pillars when the samples were reheated at 80 °C. This can be attributed to the significant modulus drop above $T_{g,}$ from 2.2 GPa at room temperature to 3.1 MPa at 80 °C. According to Equations 3.5-3.9, except for JKR model, which predicts modulus independence, all the other models predict that the adhesion would decrease when modulus decrease. For the interweaved pillars, the

separation force in either normal or shear direction scales linearly with the modulus, to 0.8 N/cm^2 for normal adhesion and to 13.2 N/cm^2 for shear adhesion. For the indented pillars, the decrease in adhesion depends on the contact geometry, which is down to 3.5 N/cm^2 based on cylindrical parallel-contact model (Equation 3.7) and to 3.6 N/cm^2 for indenting pillars by the peeling model for cylindrical pillars (Equation 3.9). Overall, the measured adhesion values, 3.6 N/cm^2 (normal) and 7.6 N/cm^2 (shear) at 80 °C, were within the range of the calculated values.

Lastly, we note that although the entropic energy stored in the deformed SMP pillars can be later released on demand upon reheating above T_g to trigger automatic debonding, the recovery of high-aspect-ratio SMP micropillars should be different from the recovery behavior of bulk SMP since the surface adhesion energy becomes significant for densely packed micropillars with feature size of 1 μm.[34] Buckled micropillars can be fully recovered only if the elastic restoring energy exceeds the surface energy between interweaved or indented pillars. While the low modulus at the rubbery state facilitates buckling and intimate interfacial contact between two opposing pillar surfaces for bonding, the subsequent cooling to room temperature results in high modulus at the glassy state, which favors high adhesion. When the interfacial width, thus effective contact area, between two deformed pillars is at maximum, the highest adhesion strength is expected. However, the maximum contact is unfavorable for the pillar recovery. In our experiments, the collapsed α = 2 pillars could not be recovered and α =3 pillars were partially recovered after reheating.

Since the critical aspect ratio AR_c of pillar collapsing for d = 1 μm pillars is low (AR_c = 3.2 for lateral collapse and 6.0 for ground collapse), we investigated larger micropillars

(hexagonal array, d = 10 μm, s = 20 μm, AR = 4), which have the critical aspect ratio of 6.9 for lateral collapse and 28.0 for ground collapse. However, when two sets of 10 μm pillars were compressed together under the 24 N/cm^2 preload, they only showed partial recovery (Figure 3.14) with comparable adhesion strength, 54.4 N/cm^2 and 64.0 N/cm^2 for normal and shear adhesion, respectively, at room temperature.

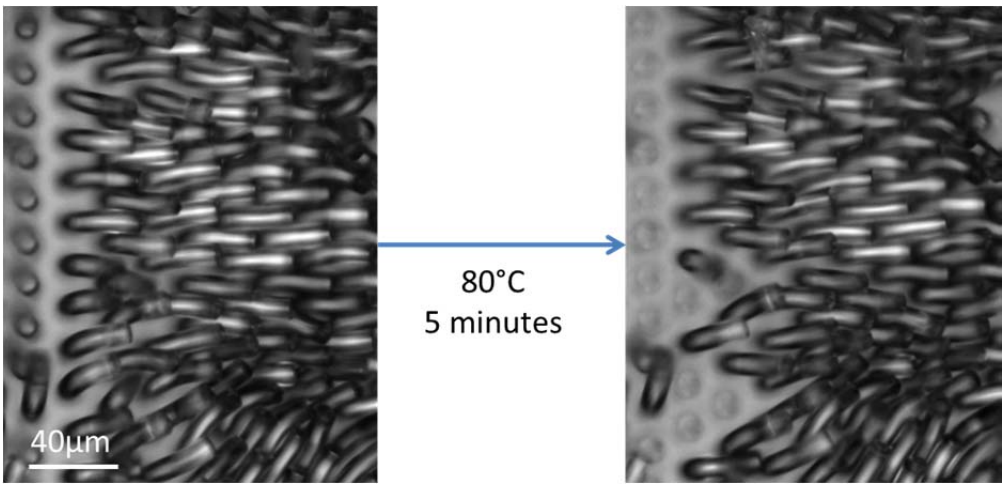

Figure 3.14 Optical images of the partially recovered 10 μm pillars in hexagonal lattice. While the recovery is observed on the slightly deformed pillars, nearly no recovery can be observed on fully collapsed pillars.

We believe that similar to the 1 μm pillars, the 10 μm pillars were also interweaved or indented when compressed together under the load, which permanently deformed the pillars beyond its critical buckling threshold. It is also found that holding the bulk SMP at programming temperature above T_g for prolonged duration would make the film unrecoverable due to the thermal-mechanical aging effect.[59, 60] This is inevitable in our experiments during the preloading stage of our adhesives. Nevertheless, careful design of pillar geometry and fine-tuning of the T_g, elastic properties of the SMP and optimization

of preload condition will be investigated to find the balance of strong adhesion and recoverability of SMP pillars.

3.6 Conclusion

In summary, we designed a unique dry adhesive with strong adhesion based on buckling and interlocking between two sets of identical SMP pillar arrays. The SMP pillar arrays were engaged at 80 °C, above SMP T_g at a preload above the buckling threshold. The pillars were found interweaved and/or indented to each other from both experiments and FEA simulation. The strong bonding was achieved after cooling the interlocked sample to room temperature, upon which the SMP pillars became glassy. The deformed pillar-to-pillar contact led to very strong dry adhesion force at room temperature, ~ 53.6 ± 25.1 N/cm^2 in the normal direction and ~ 71.9 ± 23.2 N/cm^2 in the shear direction. These values are much larger than those from pillar-to-flat (12.3 ± 8.8 N/cm^2, normal and 15.0 ± 2.3 N/cm^2, shear) and flat-to-flat contact surfaces (7.1 ± 5.0N/cm^2, normal and 15.8 ± 2.0N/cm^2, shear). Our calculation using mechanical and contact mechanics models predicts that the pillar-to-pillar adhesion should lie between the scenario of interweaved and indented pillar-to-pillar contact, in good agreement with our experimental observations. For the interweaved pillars, FEA simulations and mechanical models further showed that the theoretical adhesion force could be comparable or surpassing the maximum tensile stress of the SMP, leading to pillar fracture. When increasing pillar spacing, we found that the adhesion strength was weakened while the adhesion anisotropy increased in both experiments and calculations, which could be attributed to the decreased number of the interweaved pillars. Moreover, we showed that the use of SMP could allow for easy separation simply by heating the

interlocked pillars above T_g owing to the dramatic drop of elastic modulus. The interlocking adhesives reported here are, however, not reversible due to irreversible buckling of the small and tall pillars in a dense array. By varying the pillar geometry and size, it is possible to recover the deformed SMP pillars for reversible adhesion. Nevertheless, we believe the presented study of interlocking adhesion mechanisms based on buckling and tunable modulus, offer important insights of how to control the interfacial contact between pillars, which are critical to the design of strong dry adhesives in practice. In turn, it would open up a new path for creating structured surfaces for other applications, such as pressure sensors.[41]

3.7 Reference

1. K. Autumn, M. Sitti, Y. C. A. Liang, A. M. Peattie, W. R. Hansen, S. Sponberg, T. W. Kenny, R. Fearing, J. N. Israelachvili and R. J. Full, *Proc. Natl. Acad. Sci. U. S. A.*, 2002, **99**, 12252-12256.

2. C. Creton and S. Gorb, *MRS Bull.*, 2007, **32**, 466-472.

3. G. Huber, H. Mantz, R. Spolenak, K. Mecke, K. Jacobs, S. N. Gorb and E. Arzt, *Proc. Natl. Acad. Sci. U. S. A.*, 2005, **102**, 16293-16296.

4. K. Autumn, Y. A. Liang, S. T. Hsieh, W. Zesch, W. P. Chan, T. W. Kenny, R. Fearing and R. J. Full, *Nature*, 2000, **405**, 681-685.

5. Y. Tian, N. Pesika, H. B. Zeng, K. Rosenberg, B. X. Zhao, P. McGuiggan, K. Autumn and J. Israelachvili, *Proc. Natl. Acad. Sci. U. S. A.*, 2006, **103**, 19320-19325.

6. B. X. Zhao, N. Pesika, H. B. Zeng, Z. S. Wei, Y. F. Chen, K. Autumn, K. Turner and J. Israelachvili, *J. Phys. Chem. B*, 2009, **113**, 3615-3621.

7. A. Ghatak, L. Mahadevan, J. Y. Chung, M. K. Chaudhury and V. Shenoy, *Proc. R. Soc. London Ser. A-Math. Phys. Eng. Sci.*, 2004, **460**, 2725-2735.

8. N. J. Glassmaker, A. Jagota, C. Y. Hui and J. Kim, *J. R. Soc. Interface*, 2004, **1**, 23-33.

9. N. J. Glassmaker, A. Jagota, C. Y. Hui, W. L. Noderer and M. K. Chaudhury, *Proc. Natl. Acad. Sci. U. S. A.*, 2007, **104**, 10786-10791.

10. S. Kim and M. Sitti, *Appl. Phys. Lett.*, 2006, **89**, 261911.

11. A. del Campo, C. Greiner and E. Arzt, *Langmuir*, 2007, **23**, 10235-10243.

12. S. Reddy, E. Arzt and A. del Campo, *Adv. Mater.*, 2007, **19**, 3833-+.

13. C. Greiner, A. del Campo and E. Arzt, *Langmuir*, 2007, **23**, 3495-3502.

14. M. K. Kwak, H. E. Jeong, T. I. Kim, H. Yoon and K. Y. Suh, *Soft Matter*, 2010, **6**, 1849-1857.

15. Y. Rahmawan, T. I. Kim, S. J. Kim, K. R. Lee, M. W. Moon and K. Y. Suh, *Soft Matter*, 2012, **8**, 1673-1680.

16. L. Ge, S. Sethi, L. Ci, P. M. Ajayan and A. Dhinojwala, *Proc. Natl. Acad. Sci. U. S. A.*, 2007, **104**, 10792-10795.

17. L. Qu and L. Dai, *Adv. Mater.*, 2007, **19**, 3844-+.

18. L. T. Qu, L. M. Dai, M. Stone, Z. H. Xia and Z. L. Wang, *Science*, 2008, **322**, 238-242.

19. J. Lee, C. Majidi, B. Schubert and R. S. Fearing, *J. R. Soc. Interface*, 2008, **5**, 835-844.

20. J. H. Lee, R. S. Fearing and K. Komvopoulos, *Appl. Phys. Lett.*, 2008, **93**, 191910.

21. *U. S. Pat.*, 2717437, 1955.

22. *U. S. Pat.*, 3,748,701, 1973.

23. F. Allyn and B. Golden, in *Why Didn't I Think of That: Bizarre Origins of Ingenious Inventions We Couldn't Live Without*, Wiley, 1 edn., 1997, pp. 99-104.

24. S. N. Gorb, R. G. Beutel, E. V. Gorb, Y. K. Jiao, V. Kastner, S. Niederegger, V. L. Popov, M. Scherge, U. Schwarz and W. Votsch, *Integr. Comp. Biol.*, 2002, **42**, 1127-1139.

25. S. N. Gorb and V. L. Popov, *Philos. Trans. R. Soc. Lond. Ser. A-Math. Phys. Eng. Sci.*, 2002, **360**, 211-225.

26. C. Pang, T.-i. Kim, W. G. Bae, D. Kang, S. M. Kim and K.-Y. Suh, *Adv. Mater.*, 2012, **24**, 475-479.

27. R. M. McMeeking, L. F. Ma and E. Arzt, *J. Appl. Mech.-Trans. ASME*, 2009, **76**.

28. H. Ko, J. Lee, B. E. Schubert, Y. L. Chueh, P. W. Leu, R. S. Fearing and A. Javey, *Nano Lett.*, 2009, **9**, 2054-2058.

29. H. Ko, Z. X. Zhang, Y. L. Chueh, J. C. Ho, J. Lee, R. S. Fearing and A. Javey, *Adv. Funct. Mater.*, 2009, **19**, 3098-3102.

30. H. Shahsavan and B. X. Zhao, *Langmuir*, 2011, **27**, 7732-7742.

31. S. Vajpayee, K. Khare, S. Yang, C. Y. Hui and A. Jagota, *Adv. Func. Mater.*, 2011, **21**, 547-555.

32. C. H. Pang, S. M. Kim, Y. Rahmawan and K. Y. Suh, *ACS Appl. Mater. Interfaces*, 2012, **4**, 4225-4230.

33. C. Pang, D. Kang, T.-i. Kim and K.-Y. Suh, *Langmuir*, 2011.

34. Y. Zhang, C. W. Lo, J. A. Taylor and S. Yang, *Langmuir*, 2006, **22**, 8595-8601.

35. D. Chandra and S. Yang, *Acc. Chem. Res.*, 2010, **43**, 1080-1091.

36. T. Xie and I. A. Rousseau, *Polymer*, 2009, **50**, 1852-1856.

37. R. Wang and T. Xie, *Chem. Comm.*, 2009, **46**, 1341-1343.

38. R. Wang and T. Xie, *Langmuir*, 2010, **26**, 2999-3002.

39. T. Xie and X. C. Xiao, *Chem. Mat.*, 2008, **20**, 2866-2868.

40. S. Kim, M. Sitti, T. Xie and X. C. Xia, *Soft Matter*, 2009, **5**, 3689-3693.

41. C. Pang, G.-Y. Lee, T.-i. Kim, S. M. Kim, H. N. Kim, S.-H. Ahn and K.-Y. Suh, *Nat. Mater.*, 2012, **11**, 795-801.

42. A. Lendlein and S. Kelch, *Angew. Chem.-Int. Edit.*, 2002, **41**, 2034-2057.

43. P. T. Mather, X. F. Luo and I. A. Rousseau, *Ann. Rev. Mater. Res.*, 2009, **39**, 445-471.

44. T. Xie, *Polymer*, 2011, **52**, 4985-5000.

45. C. Y. Hui, A. Jagota, Y. Y. Lin and E. J. Kramer, *Langmuir*, 2002, **18**, 1394-1407.

46. S. Timoshenko, *Theory of elastic stability*, 2d edn., McGraw-Hill, New York, 1961.

47. I. Amidror, *The Theory of the Moiré Phenomenon*, Springer London, London, 2009.

48. S. H. Kang, N. Wu, A. Grinthal and J. Aizenberg, *Phys. Rev. Lett.*, 2011, **107**, 177802.

49. C. T. F. Ross, *Mechanics of solids*, Prentice Hall, London ; New York, 1996.

50. C. S. Davis and A. J. Crosby, *Soft Matter*, 2011, **7**, 5373-5381.

51. J. Li, Y. An, R. Huang, H. Jiang and T. Xie, *ACS Appl. Mater. Interf.*, 2012, **4**, 598-603.

52. K. L. Johnson, *Contact mechanics*, Cambridge University Press, Cambridge Cambridgeshire ; New York, 1985.

53. B. Sumer, C. D. Onal, B. Aksak and M. Sitti, *Journal of Applied Physics*, 2010, **107**.

54. K. Kendall, *J. Phys. D-Appl. Phys.*, 1975, **8**, 1449-1452.

55. S. Kim, M. Sitti, C. Y. Hui, R. Long and A. Jagota, *Appl. Phys. Lett.*, 2007, **91**, 161905.

56. M. Kamperman, E. Kroner, A. del Campo, R. M. McMeeking and E. Arzt, *Adv. Eng. Mater.*, 2010, **12**, 335-348.

57. E. Kroner, J. Blau and E. Arzt, *Rev. Sci. Instrum.*, 2012, **83**.

58. E. Kroner, D. R. Paretkar, R. M. McMeeking and E. Arzt, *Journal of Adhesion*, 2011, **87**, 447-465.

59. H. Tobushi, S. Hayashi, K. Hoshio and N. Miwa, *Smart Mater. Struct.*, 2006, **15**, 1033-1038.

60. K. Dasharathi and J. A. Shaw, Behavior and Mechanics of Multifunctional Materials and Composites 2013, San Diego, California, United States, 2013.

Chapter 4

Controlled deformation of SMP pillars for tuning surface wettability and patterning colloidal particles

4.1 Introduction

Pattern collapse and deformation[1-4] has been the major concern in fabrication of microstructured soft materials for various applications. In nature, however, twisting,[5] bundling,[6] tilting[7] and bending[8] of surface patterns or objects are commonly observed. For example, gecko setae are high aspect ratio (HAR) fibrils responsible for strong dry adhesion and easy detachment.[9] The bristles on the tarsus of the beetle clumps upon separation from the ground and splay upon engagement, maximizing the adhesion force via capillarity.[6] The tendrils of the cucumber curl dramatically, which changes the effective stiffness upon stretching as an adaptive spring.[5] On the other hand, the growing vertebrate gut tube buckles and bends itself under the constraint of mesentery, allowing it to reside in a confined space.[8]

Recently, pattern deformation has been exploited in non-conventional patterning to create complex nanoparticle assembly,[10] photonic[11] or phononic crystals[12] and negative Poisson ratio materials.[13] "Microdominos" have been created by shearing photolithographic patterns to print charge arrays into electrets.[14] Periodic metallic nanostructures are fabricated by microtoming[15] and nanoskiving[16] for optical applications. Combining soft lithography and mold deformation, Pokroy *et al.* have fabricated tilted and twisted micro- and nanostructures.[17-19] Similarly, Duan *et al*. show

that pattern collapse morphologies can be manipulated by designing feature cross sections, curvature and obliqueness.[20]

It is known that surface wettability is highly dependent on both surface chemistry and surface topography.[21] Surface chemistry determines the intrinsic wettability of the surface. Surface topography, on the other hand, can significantly enhance the (non)wettability, creating superhydrophilic, superhydrophobic[22, 23] or superoleophobic surfaces,[24-26] which are of interests for a wide range of applications, including highly sensitive plasmonic devices, oil-water separation membranes and self-cleaning surfaces.[27-29] Surface topography is determined by geometrical parameters, including feature size[30, 31] spacing, shape,[24, 32, 33] and lattice symmetry.[32, 34, 35] In this regard, controlled deformation of pattern geometry becomes an attractive method to tune the surface wettability.[36-40] Using oblique electron-beam irradiation, Kim *et al.*[39] have fabricated tilted polymer pillars by electron beam (e-beam) induced degradation, leading to volume shrinkage on the exposed side of the pillars that bends the pillars toward the e-beam. On such surfaces unidirectional water spreading along the pillar-tilting direction is observed, driven by the contact angle hysteresis.[39] With similar concept, Chu and coworkers tilt HAR silicon pillars by angled metal deposition, followed by cooling.[40] By controlling the tilting angle together with the surface chemistry of the pillars, water can be fully pinned, propagated unidirectionally, or spread bi-directionally on the pillars. Although these studies demonstrate control of the liquid dynamics and anisotropy, fabrication of the surface structures is non-trivial. Further, the titled pillars reported in the literature so far are not reversible.

Here, we fabricated recoverable, tilted pillars from shape memory polymers (SMPs) by replica molding, followed by heating above the glass transition temperature (T_g) of SMPs and shearing under a load to tilt the pillars. Upon reheating above the T_g, the tilted pillars could be recovered, showing distinct wettability in the tilted state and the recovered state. We then coated the pillars with a thin layer of gold of variable thickness to control the tilting angle. The presence of the metal layer endowed partial recovery of the pillars, as well as a wettable surface. Together with the control of the tilting angle and surface coating of the metal layer, a unique anisotropic liquid spreading behavior was observed, where the water droplet could only propagate opposite to the pillar tilting direction. The observation was completely different from the previous studies, where the titled pillars were coated uniformly with polymers or metals.[39, 40] Further, we created hierarchical structures by picking up colloidal nanoparticles on the SMP pillar array. By controlling the direction of SMP pillars in contact with the nanoparticle film, in the normal or shear direction, we showed that nanoparticles could be selectively picked up either on the tips of the pillars or on the side walls. We anticipate that such flexible system can be applied to the fabrication of more complex optical and surface plasmonic structures.[27]

4.2 Experimental methods

4.2.1 Materials and fabrication

SMP pillars were fabricated by replica-molding following the procedure reported earlier.[41] The pillar master was fabricated by photolithography from SU-8 photoresist, followed by replica molding to photocurable liquid epoxy resin (D.E.R 354, Dow Chemical) on a glass slide. For deformation, the SMP pillars were heated to 80 °C on a

hotplate for 1 min, followed by shearing using a pre-cleaned glass slide or an epoxy pattern under a load. The whole setup was then removed from the hotplate and cooled down completely (within ~ 1 min.) before removing the load. The silica nanoparticle assembly was prepared from 10 – 30 vol% silica nanoparticles (Alfa Aesar) dispersed in a mixed solution of ethanol and ethylene glycol (1:1 vol/vol). 10-50 μL nanoparticle solution was spin coated on to a 1 square inch pre-cleaned Si wafer at 3000-6000 rpm accelerated at 900-1800 rpm/s for 300 s for a single layer or multilayer nanoparticle film. Gold was sputter coated on the deformed SMP pillars using Quorum Q150T ES turbo-pumped sputter coater for 20-100 s at 20 mA. The gold-palladium alloy is coated by Cressington 108 sputter coater for 30s at 30mA. Both gold and gold-palladium alloy targets were obtained from Ted Pella Inc.

4.2.2 Characterization

The original and deformed SMP structures were examined using Olympus BX61 optical microscope, FEI Quanta FEG ESEM, FEI Strata DE235 scanning electron microscopes (SEM) at an accelerating voltage of 5kV, respectively. The static contact angles of the SMP structures were characterized by ramé-hart automated goniometer model 290 with DropImage Advanced v1.5 with 8 μL water droplet. The sliding angles were measured from 10 μL water droplet on a home-made tilting device. The thickness of sputter-coated metal films was measured by Veeco Dimension 3100 atomic force microscope.

4.3 Wettability control by SMP deformation

SMP is a smart material system that has been applied to biomedical devices,[42] temperature sensors,[43] color switching devices,[44-46] reconfigurable surfaces,[47] and

adhesives.[48-50] One unique characteristic of SMP is its tunable mechanical property near the phase transition temperature (e.g. melting temperature, T_m, or glass transition temperature, T_g). It is soft above the T_m or T_g, therefore, deformable to a temporary shape but becomes hard upon cooling, thus, locking the temporary or permanent shape.

So far, research efforts have been focused extensively on the bulk SMP formulation, types of stimuli, and the bulk material recovery mechanism and capability.[51-56] It was not until recently that researchers begin to look into the recovery property and applications of micro- or nanostructures.[41, 44, 47-49, 57] Nevertheless, few have exploited the large deformation and collapse of HAR SMP microstructures. Recently, we have created a new type of dry adhesives with strong adhesion (50-70 N/cm^2) by interlocking the buckled SMP pillars.[41]

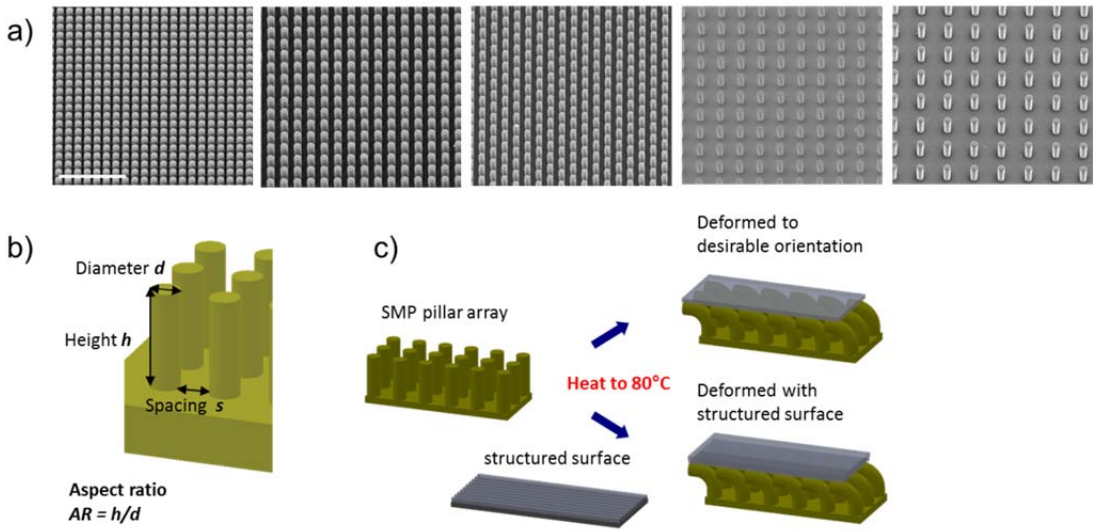

Figure 4.1 Preparation and deformation of shape memory polymer pillars. a) Representative SEM images of SMP pillar arrays used in the experiments. (left to right) Square lattice with d = 10 μm, s = 5 μm and AR = 2 (sample 1); Square and hexagonal lattice with d = 10 μm, s = 10 μm and AR = 3 (sample 2 and 3); square lattice with d = 10 μm, s = 20 μm and AR = 2.5 (sample 4); square lattice with d = 10 μm, s = 30 μm and AR = 3 (sample 5). Scale bar: 100 μm. b) Specifications of pillar samples. c) Schematics of the fabrication and deformation process.

Here, we extend the prior study and demonstrate the deformation and recovery of HAR SMP pillars as an unconventional patterning technique as well as their applications in surface wettability. Using an epoxy-based SMP,[41] we fabricated five different types of pillar arrays with diameter d = 10 μm: 1) square lattice, side-to-side spacing s = 5 μm, aspect ratio AR = height h/diameter d = 2; 2) square lattice, s = 10 μm, AR = 3; 3) hexagonal lattice, s = 10 μm spacing, AR = 3; 4) square lattice, s = 20 μm, AR = 2.5; 5) square lattice, s = 30 μm, AR = 3 (see the corresponding SEM images in Figure 4.1a and pillar definition in Figure 4.1b). It should be noted that HAR polymer structures are liable to mechanical instabilities, including lateral[1] or ground collapse,[2] especially when the feature size is in the (sub)micron length-scale, due to increasing surface area and adhesion force, which compete with high compliance of the soft material.[3] For lateral collapse, the criterion for critical aspect ratio (AR_c) is[1]

$$AR_c = \frac{3^{1/4}\pi^{1/3}E^{1/3}s^{1/2}}{2^{17/12}W^{1/3}d^{1/6}\left(1-\upsilon^2\right)^{1/12}} \tag{4.1}$$

where E is the elastic modulus, W is the work of adhesion, and v is the Poisson's ratio. For ground collapse, AR_c becomes[2]

$$AR_c = \frac{\pi^{5/3}\left(1-\upsilon^2\right)^{-1/6}}{2^{11/3}3^{1/2}}\left(\frac{Ed}{W}\right)^{2/3} \tag{4.2}$$

Experimentally, the deformed or tilted SMP pillars were heated to 80 °C above its T_g (~ 60 ^{o}C) for the recovery to occur. However, at this temperature, the polymer is very soft (~ 3.1 MPa), and the pillars can be easily collapsed. Therefore, the AR_c at 80 °C is calculated using the mechanical properties reported in our earlier paper[41] and summarized

in Table 4.1. To ensure that the pillars are recoverable at 80 °C, we chose SMP pillars with *AR* smaller than the critical values.

Spacing	Lateral	Ground
s = 5μm	4.9	28.0
s = 10μm	6.9	28.0
s = 20μm	9.8	28.0
s = 30μm	12.0	28.0

Table 4.1 Critical aspect ratio for lateral and ground collapse of SMP pillars (d = 10 μm).

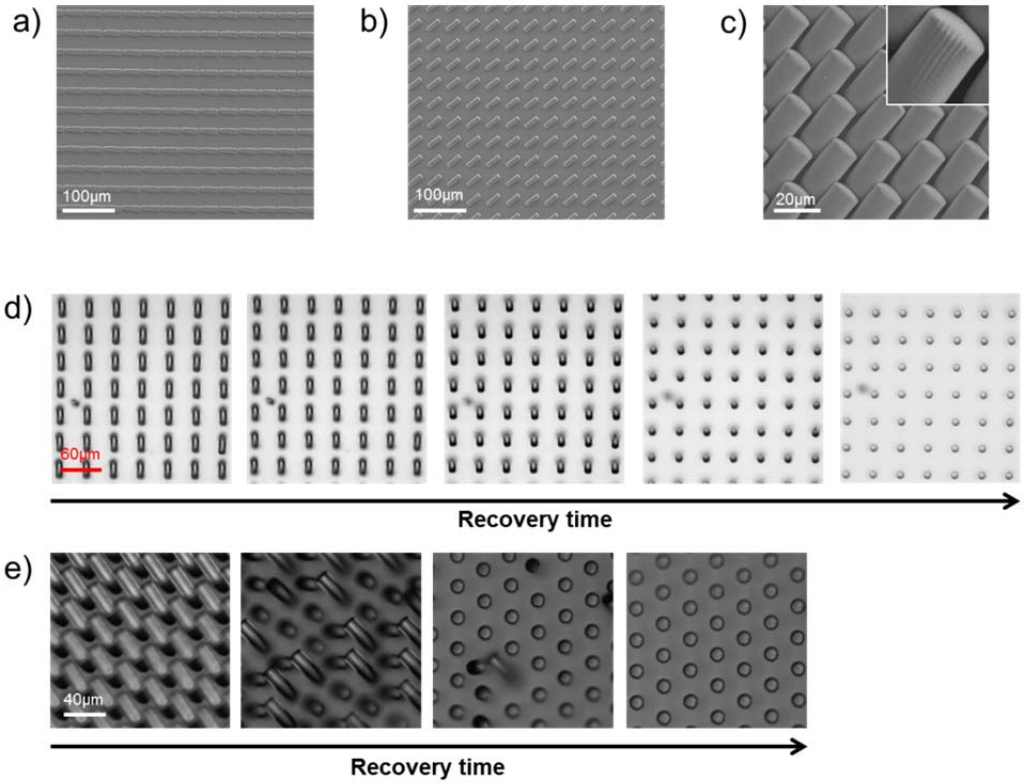

Figure 4.2 Deformed and recovered SMP pillars. (a) SMP pillars (d = 10 μm, s = 30 μm, AR = 3) deformed along a lattice vector. (b) The same pattern as (a) deformed diagonally. (c) Hierarchical structure made by deforming the pillars diagonally (d = 10 μm, s = 5 μm, AR = 3) with surface structured with channels (~ 500 nm *width*, 1 μm pitch, 300 nm depth). (d) Recovery process of SMP pillars, sample 5 (square array, d = 10 μm, s = 30 μm, AR = 3). (e) Recovery process of SMP pillars, sample 3 (hexagonal array, d = 10 μm, s = 10 μm, AR = 3).

The SMP pillar samples were subjected to shear deformation at 80 °C either by a flat or a structured surface as shown schematically in Figure 4.1c. The representative deformed SMP pillars of sample 5 can be seen in Figure 4.2a and 4.2b for shearing along the lattice vector or diagonally along the lattice. Both of the samples showed uniform deformation and orientation. Using a PDMS 1-D channel structure (width ~ 500 nm, pitch ~ 1 μm, depth = 0.3 μm) as the shearing substrate, we also demonstrated a hierarchical structure (see Figure 4.2c), where the 1-D structure was imprinted onto the deformed pillars (sample 1) with channels aligned in parallel to the direction of deformation. This one-step patterning technique may offer an efficient method to generate complex patterns mimicking the channel structures, for example, reported in butterfly wings[58] and mosquito legs[59] for guided water shedding.

In order to exploit SMP pillars as recoverable and reconfigurable surface structures, it is essential to evaluate the shape recovery of the deformed features. As shown in Figure 4.2d and Figure 4.2e for sample 5 and sample 3, respectively, tilted SMP pillars completely recovered when reheated at 80 °C, but in different manners. For sample 5, all the pillars recovered simultaneously and uniformly, while for sample 3, the recovery was more localized. This may be due to the small spacing of sample 3 (10 μm spacing in a hexagonal lattice), where the pillars were in lateral contact. The elastic energy of each pillar must first overcome the local van der Waals interactions between the laterally contacted pillars upon reheating before the whole array is fully recovered. In the case of sample 5, the pillar spacing was large enough (30 μm spacing in a square lattice) such that there was no lateral contact between the tilted pillars.

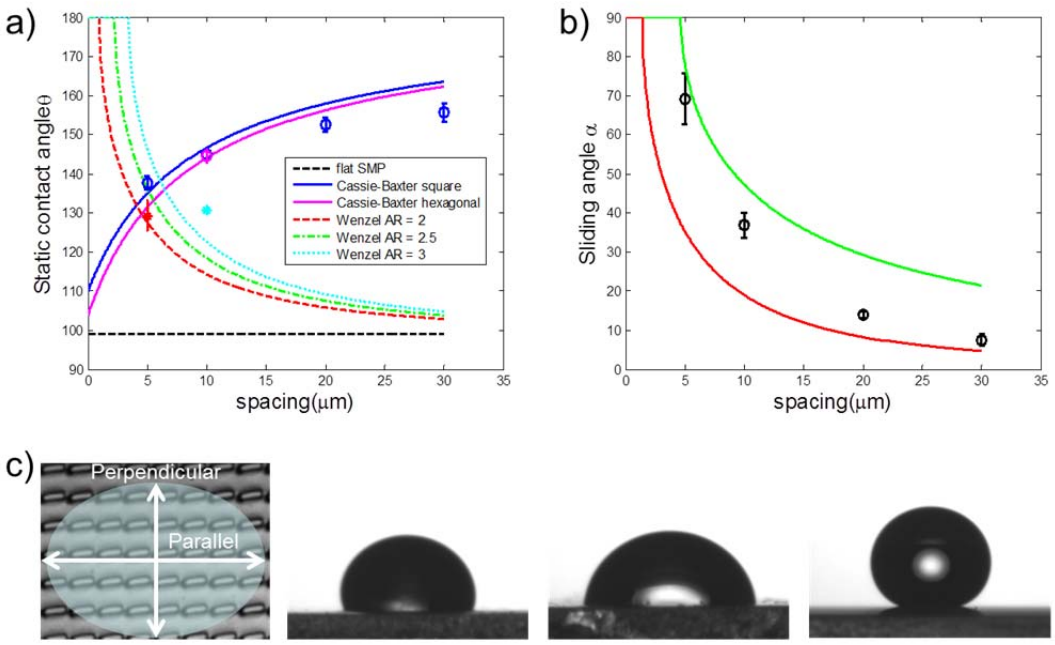

Figure 4.3 Wettability of SMP pillar arrays. (a) Static water contact angles of straight pillars (circles) and deformed pillars (stars) and theoretical values (lines) predicted by the Cassie-Baxter and Wenzel models. (b) Experimental sliding angles (circles) and the theoretical model by Frenkel (green curve) and Lv (red curve). (c) Anisotropic wetting on deformed sample 5, from left to right: the schematic showing the direction the droplet being viewed; the droplet on the deformed pillars, viewed perpendicularly to the deformed pillars; the droplet on the deformed pillars, viewed in parallel to the deformed pillars; the droplet on the original SMP pillars.

With the capability of manipulating the deformed surface patterns and their recovery, we examined the wetting behaviors on such surfaces. As shown in Figure 4.3a, the water contact angles for SMP pillars were compared with theoretical Cassie-Baxter and Wenzel models. In the Cassie-Baxter model, the droplet is assumed to sit on a composite surface and the apparent contact angle θ_{CB} is expressed as[60, 61]

$$\cos\theta_{CB} = \sum_i f_i \cos\theta_i \qquad (4.3)$$

where f_i is the area fraction of the ith component in the composite state and θ_i is the intrinsic contact angle of the ith component. For a square lattice of pillar array, θ_{CB} can be described in terms of the pillar diameter and spacing

$$\cos\theta_{CB} = \frac{\pi d^2}{4(d+s)^2}(1+\cos\theta_{SMP}) - 1 \tag{4.4}$$

where θ_{SMP} is the contact angle of flat SMP. For hexagonal lattice, Equation 4.3 becomes

$$\cos\theta_{CB} = \frac{\pi d^2}{2\sqrt{3}(d+s)^2}(1+\cos\theta_{SMP}) - 1 \tag{4.5}$$

The apparent contact angle θ_W in the Wenzel model is given by[62]

$$\cos\theta_W = r\cos\theta \tag{4.6}$$

where r the roughness ratio, defined as the real contact area to the projected area. Assuming that the droplet completely wets the deformed structures, Equation 4.6 can be rearranged for a square lattice pillar array

$$\cos\theta_W = \frac{(d+s)^2 + \pi ARd^2}{(d+s)^2}\cos\theta_{SMP} \tag{4.7}$$

Under the same assumption for a hexagonal lattice, Equation 4.6 is

$$\cos\theta_W = \frac{\sqrt{3}(d+s)^2 + 2\pi ARd^2}{\sqrt{3}(d+s)^2}\cos\theta_{SMP} \tag{4.8}$$

According to Figure 4.3a, the water contact angles of the original SMP pillars followed Equations 4.4 and 4.5, while the water contact angles of the deformed pillars agreed with the Wenzel model. We note that the Wenzel model curves shown in Figure 4.3a are for square lattices only. For the hexagonal lattice (sample 3), the measured contact angle was 127.1° ± 5.1°, also close to the Wenzel model prediction, 126.7°. However, since our SMP is intrinsically hydrophobic, it will be difficult for the water droplet to fully penetrate into the deformed structure.[21] Rather, there should be small air pockets trapped within the grooves. This may explain why our measured contact angles were slightly larger than the theoretical ones.

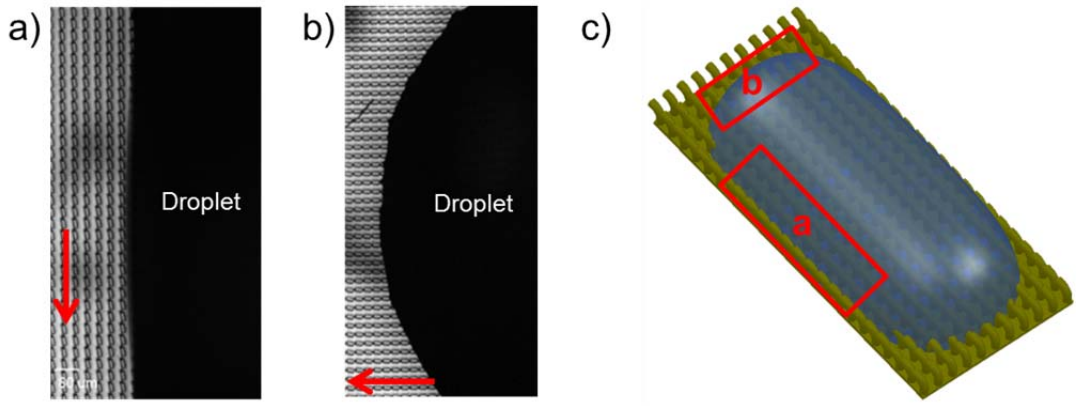

Figure 4.4 Triple phase line of deformed sample 5 (square array, d = 10 μm, s = 30 μm, AR = 3). (a) Pinned triple phase line along the deformed direction (red arrow). (b) Unpinned triple phase line perpendicular to the deformed direction. (c) Schematic of a droplet on deformed pillars, showing where the triple phase line is imaged in a and b.

More interestingly, for the larger spacing samples (s = 20 μm and 30 μm), water wet on the sheared and deformed pillar surface anisotropically. The average water contact angles along the perpendicular and parallel directions of the sheared square lattices were 131.1° ± 4.1° and 107.0° ± 5.5° for sample 4 (s = 20 μm), and 113.1° ± 7.4° and 100.9° ±

7.4° for sample 5 (s = 30 μm), respectively. As seen in Figure 4.3c, the droplet on the deformed pillars (sample 5) clearly exhibited anisotropic wetting while the original pillars were superhydrophobic. Figure 4.4 further depicts the difference in the appearance of the triple phase line for sample 5. Clearly, the triple phase line is only pinned along the channels formed by the deformed pillars because of the higher energy barrier in this direction.[35, 37] While being sheared along the lattice vector direction, these two samples are the only two samples where the pillars could be totally collapsed without interacting with each other. As the spacing is becoming smaller than the pillar height, the pillars can overlap with neighboring ones once fully deformed, forming a sawtooth-like structure (see Figure 4.5). This height variation would act as additional topological defects to pin the triple line,[21] and thus increase the contact angle parallel to the deformed patterns. Experimentally, no pronounced anisotropic wetting behavior was observed for samples 1 to 3.

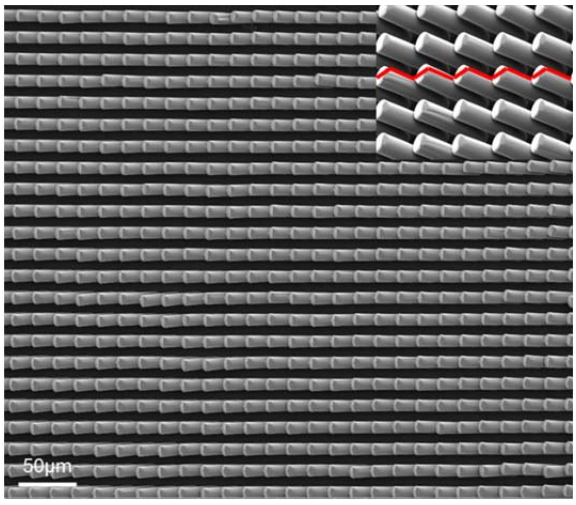

Figure 4.5 Sawtooth-like structure resulting from the small spacing samples (here is sample 2, square lattice, 10 μm spacing, aspect ratio 3). The inset shows the magnified structure tilted by 30°. The red line highlights the sawtooth-like shape.

The wettability of the original and deformed pillars can be further distinguished by the dynamic wetting behaviors. In general, the droplet in Cassie-Baxter state possesses a low hysteresis (defined by the difference of advancing and receding contact angles) and high mobility owing to the trapped air that reduces the solid component, and in turn the droplet-solid adhesion. In contrast, the droplet in Wenzel state will be highly pinned.[23] The sliding angles of the original and deformed SMP pillars reflected these properties. For the original pillars, the largest spacing provided the highest air/liquid areal fraction, and thus achieving the highest water contact angle (155.6º) and the smallest sliding angle (7.5º for a 10 μL water droplet), approaching the superhydrophobic state. As the spacing decreased, the solid fraction increased, leading to smaller water contact angles and larger sliding angles (e.g. water contact angle of 137.6º and sliding angle of 69º for sample 1), as shown in Figure 4.3a and 4.3b. The sliding angle of a droplet α is the balance between the liquid adhesion force and the gravitational force. It was modeled by Frenkel on a homogeneous solid as

$$\sin\alpha = \frac{2r\gamma\left(1+\cos\theta\right)}{\rho g V} \tag{4.9}$$

where r is the contact radius of liquid droplet on the solid, γ is the liquid-air interfacial surface energy, θ is the contact angle of the liquid on the solid, ρ is the density of the droplet, g is the gravitational acceleration and V is the droplet volume. By simple geometrical consideration, r can be rewritten as

$$r = \sin\theta \sqrt[3]{\frac{3V}{\left(2-3\cos\theta+\cos^3\theta\right)\pi}} \tag{4.10}$$

Combining Equations 4.9 and 4.10 and equating θ to the apparent water contact angle on the surface (see Equation 4.3), we solved α (the green curve in Figure 3b). It can be seen that this model overestimates the sliding angle of our samples. This may be because that Frenkel's model assumes the surface is homogeneous and flat whereas ours is a composite film, where the pinning/depinning of the triple phase line can be dramatically different. Recently, Lv and coworkers developed a model addressing this issue on a square lattice pillar array with square shaped pillars[63]

$$\sin\alpha = \frac{2r\gamma\left(1+\cos\theta\right)\sqrt{f}}{\rho g V} \tag{4.11}$$

Comparing Equation 4.9 with 4.11, there is an additional $\sqrt{f}$ term by considering the contact line depinning on the patterned surface. The prediction of sliding angle from this model is shown as the red curve in Figure 4.3b. Clearly, it underestimates the sliding angles of our SMP pillars. Since Equation 4.9 was derived from square pillars in a square lattice, whether it is applicable to other lattices or pillar geometries remains questionable. Nonetheless, both models unambiguously reveal the same trend as our SMP pillars: The sliding angle increases with smaller apparent contact angle and larger spacing. The droplets on the deformed structures, on the other hand, are fully pinned even when the surfaces were turned upside down, again implying the Wenzel state wetting with high liquid-solid contact area. The strong sliding angle contrast between the original and deformed pillars was demonstrated on a partially deformed surface as shown in a series images of the water droplets sliding down the superhydrophobic top region of the sample (undeformed pillars), but trapped and collected at the bottom deformed, high-adhesion region (Figure 4.6).

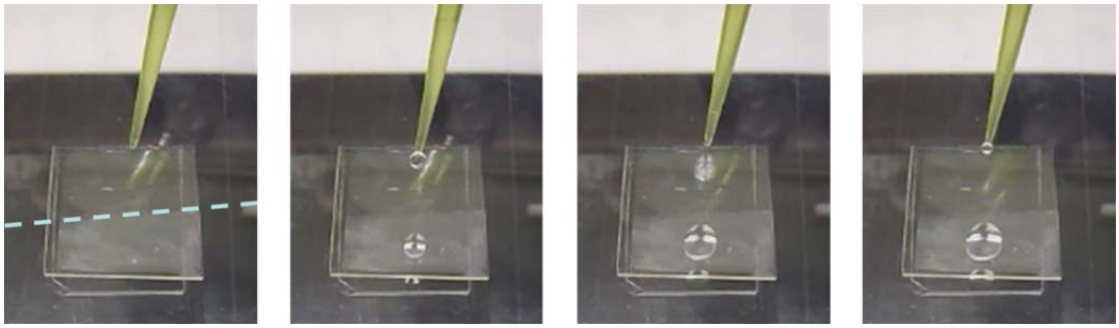

Figure 4.6 Wettability contrast between the original and deformed SMP pillar array (sample 5). The sample stage is tilted by 10°. The top half of SMP pillars are in the original state and the bottom half is in the fully deformed state, as indicated by the dashed line.

4.4 Hierarchical patterning colloidal particles using SMP pillars

In addition to wettability control, the SMP pillars can be employed as sticky fingers for advanced patterning of colloidal nanoparticles to create complex hierarchical structures. Assembly of micro-/nanoparticles has allured a great amount of interest due to its unique optical and surface properties, which can be tailored through the selection of particle size, chemistry and lattice symmetry.[64-66] Conventionally, particles such as colloids or quantum dots are assembled by slow evaporation,[67] sedimentations,[68] dip-coating[69] or spin-coating.[64, 70] These methods are normally capable of fabricating a single layer or multi-layered colloidal crystals or superlattices. With the assistance of soft lithography, it has been shown that more sophisticated 2-D patterns can be made.[71-73] However, it is nontrivial to assemble nanoparticles on microstructures with spatial control in 3-D.

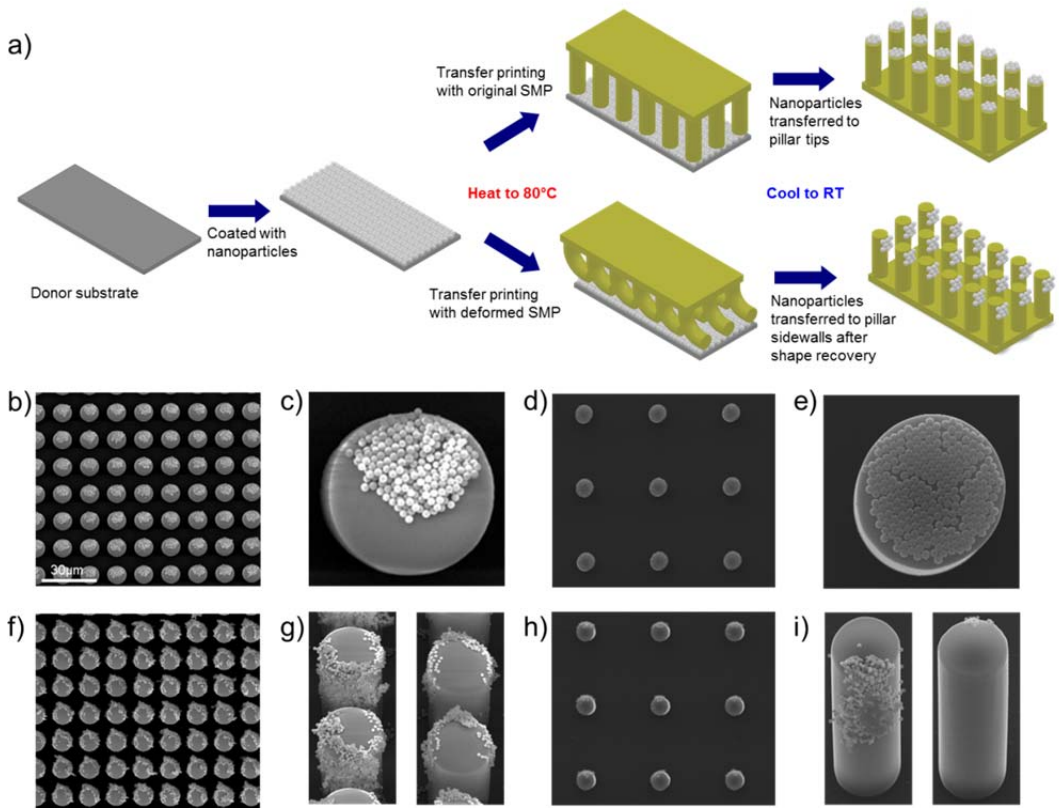

Figure 4.7 Colloidal particles selectively patterned onto SMP pillars. (a) Schematics of colloidal patterning onto SMP microstructures. Schematic of nanoparticle assembly on pillars. (b) SEM image of multilayer close-packed silica nanoparticles (500nm) picked-up by the pillar (sample 1) tips. (c) The magnified view of a single pillar in (b). (d) The SEM image of single layer close-packed silica nanoparticles (500 nm) picked-up by the pillar (sample 5) tip. (e) The magnified view of a single pillar in (d). (f) SEM image of multilayer close-packed silica nanoparticles (500 nm) picked-up by the pillar (sample 1) sidewalls. (g) The close-up view of the front (left) and back (right) side of the coated pillar in (f). (h) SEM image of a single layer close-packed silica nanoparticles (500nm) picked-up by the pillar (sample 5) sidewall. (i) The close-up view of the front (left) and back (right) side of the coated pillar in (h).

Here, by utilizing the change in mechanical properties upon heating and shape fixity upon cooling, we programmed SMP pillars as sticky fingers to pick up nanoparticles assembled on a flat sheet (see Figure 4.7a). Depending on how the pillars were engaged onto the nanoparticle film, normal to or in the shearing direction, particles could be transferred to selected locations of SMP pillars, including pillar tops and sidewalls. The

deformed pillars carrying the particles were reheated and recovered to the original shape to create the hierarchical structures. To verify the applicability to different pillar geometry and strong adhesive force of the deformed pillars, we used sample 1 and 5 to pick up both singlelayered and multilayered 500 nm silica nanoparticles assembled on Si wafers as donor substrates.

First, the deformed pillars were pressed against the nanoparticle film at 80 ºC to increase the tackiness and to promote the conformal contact. The contact area is preserved by cooling the samples down to room temperature under the load (~ 0.1 N/cm^2 for the straight pillars, ~ 2 N/cm^2 for the deformed pillars to hold the deformation) after the SMP pillars were detached. Reheating the pillars at 80 ºC recovered the particle-attached SMP pillars back to the original state. Due to partial sinking of the NPs into the pillars under the load and strong adhesive force between SMP and silica nanoparticles, the latter remained on the pillars. Figures 4.7b - 4.7e showed that the silica nanoparticles were lifted off normally from the Si wafer and transferred onto the SMP pillar top only. The close-packed nature of silica colloidal particles was clearly preserved on the pillar top, either in a multilayer (Figure 4.7b and 4.7c) or single-layer (Figure 4.7d and 4.7e) configuration. When the pillar array was deformed by shearing, however, particles were found to be attached to one side of the SMP pillars along the direction of shearing (Figure 4.7f - 4.7i).

Interestingly, when comparing the static water contact angles from the nanoparticle-coated SMP structures with the original SMP pillars, no discernible change were observed (see Figure 4.8). For a flat SMP film decorated with silica nanoparticles, the contact angle was measured as 118.9°, even higher than that of the flat SMP film (99.2°).

Our previous study showed that for amine-modified silica nanoparticles on the poly(styrene random acrylic acid) (P(S-ran-AA)) film, a thin layer of hydrophobic PS was able to wet the surface of silica nanoparticles upon annealing above T_g, rendering them hydrophobic.[74] We speculate that similarly when heating above T_g, the uncured epoxy was able to wet the pristine silica nanoparticles with surface hydroxyl groups (Figure 4.9), thus, making the surface hydrophobic. Since the surface roughness was dominated by the SMP pillars, decoration of nanoparticles on pillar tips did not have a significant effect on the overall wettability. To create a superhydrophobic surface, it requires a sufficiently large dual-scale roughness.[75-77] Nonetheless, we believe this simple and facile approach can be extended to other SMPs and nanoparticle systems to create complex 3D structures for enhanced wetting[78] or surface plasmonics applications.[27]

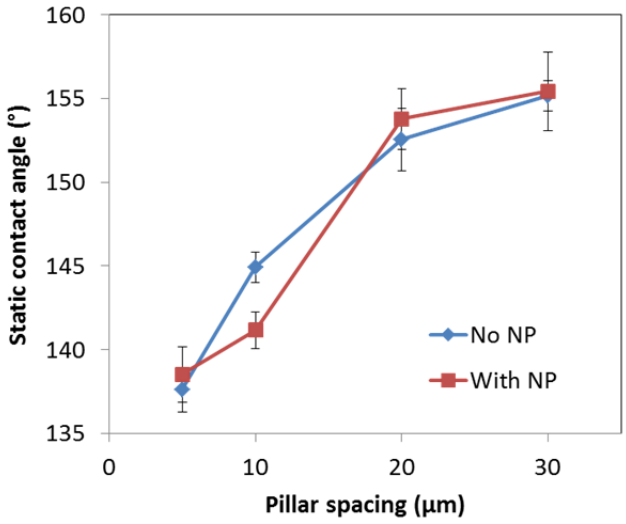

Figure 4.8 Static water contact angles of the SMP pillars with and without silica nanoparticle assembly.

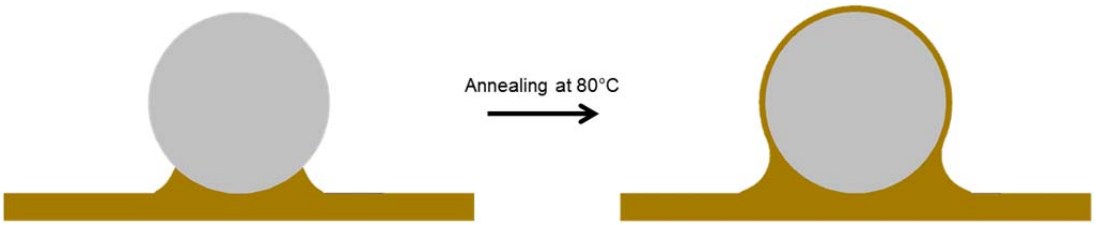

Figure 4.9 Schematic for a nanoparticle wetted by the uncured SMP after annealing.

4.5 Controlled recovery of SMP pillars for anisotropic wetting

So far we have only demonstrated the capability of manipulating the SMP pillars between two states, namely, the original straight state and the fully deformed state. Nevertheless, being able to control the extent of deformation would be invaluable for controlling the directional wetting[39, 40] and adhesion.[79] In fact, it is feasible to access any partially deformed state in our SMP pillars by manipulating the recovery constraints. To achieve this, a thin layer of gold was sputtered onto the fully deformed SMP pillars and the whole system was subsequently reheated. The pillars partially recovered to an equilibrium position, as shown in Figure 4.10a, where the pillar tilting angle could be fine-tuned by the gold film thickness (see Figure 4.10b). When the gold film thickness was increased from 0 to 25.8 nm with an increment of 6.44 nm, the tilting angle θ increased from 0 to 22.8° (see Figure 4.10c). The deformed SMP pillars tend to recover due to the stored elastic energy. However, the deposition of a much stiffer metal layer on the fully deformed pillars would prevent the complete recovery of SMP pillars. The collective bending moment balance between the SMP pillars and the coated metal layer has to reach the partially bent shape, where the degree of recovery depends on the metal layer thickness.

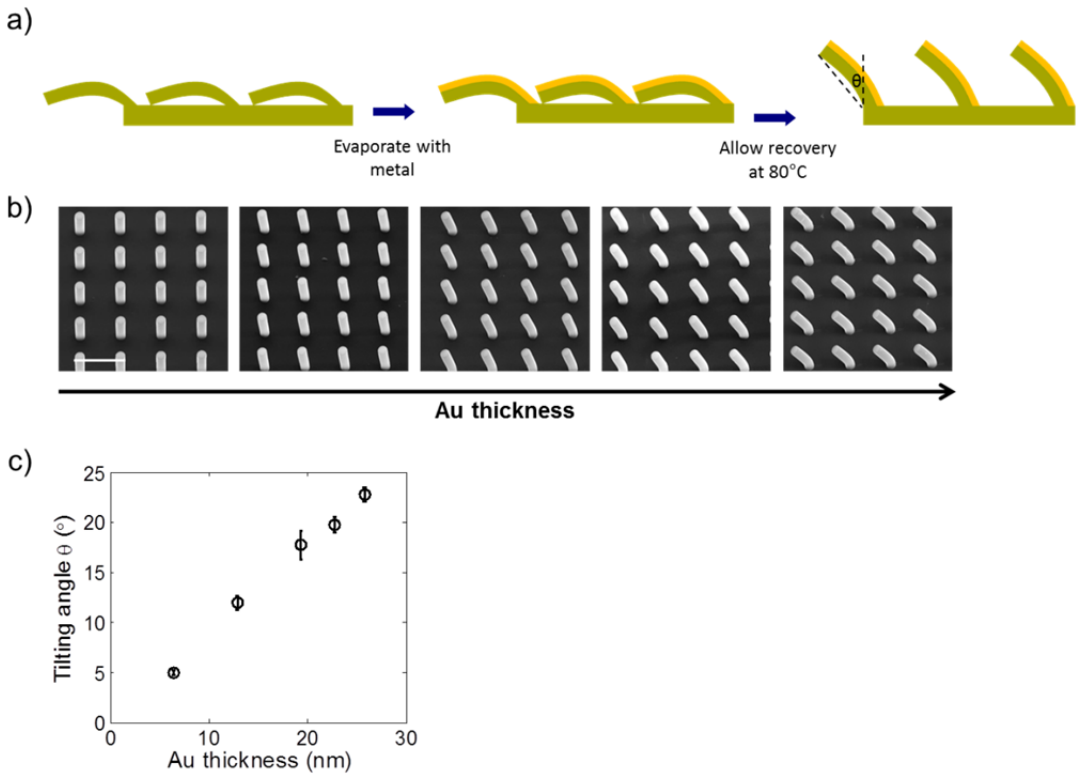

Figure 4.10 Control of the tilting angle of SMP pillars coated with a thin layer of metal. (a) Schematics of metal coating. (b) Controlling the tilting angle θ by the thickness of metal coating, the thickness of the gold layer increased by ~ 6.4 nm. Scale bar: 50 μm. (c) Tilting angle of coated SMP pillars as a function of gold thickness.

The method we demonstrate here is superior to the oblique e-beam or metal deposition,[79] which would inevitably incur damage to the original polymer features due to e-beam or thermally induced degradation. This method is also very flexible since there are rich types of metals that can be sputtered or using other low temperature deposition techniques, such as plasma-enhanced chemical vapor deposition (PECVD).[80] As a demonstration, we fabricated uniformly tilted pillars (Figure 4.11) by sputter coating ~ 20 nm gold-palladium alloy (60/40 wt%) from sample 3.

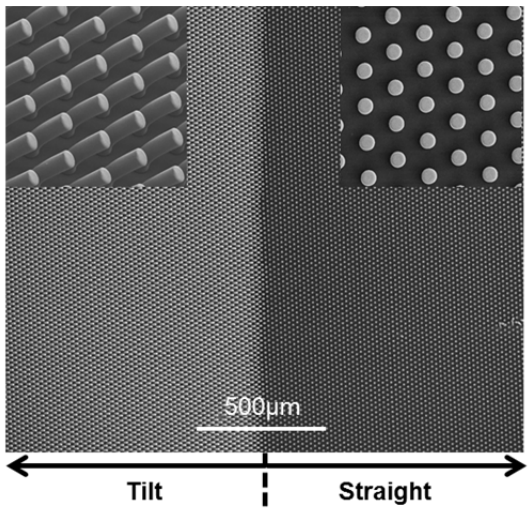

Figure 4.11 Tilted (left) and fully recovered (right) SMP pillars (sample 3) coated with ~ 20nm Au/Pd (60/40wt%).

More interestingly, the gold layer coated on the SMP pillars not only restricted the recovery behavior but dramatically changed the surface chemistry, and thus, the liquid spreading characteristics on the tilted pillars. As seen in Figure 4.12a, when water was continuously added to the existing droplet sitting on the pillars, it was clear that the wetting front of the droplet proceeded on one side continuously, while the other side was fully pinned. A closer look suggested that the liquid spread toward the opposite side of the pillar tilting direction, which was completely different from the observation reported in the literature,[39, 40, 81] where water spread unidirectionally on the tilted pillars along the tilting direction. For the previously studied tilted pillars, the entire surface is conformably coated with metal or polymers; therefore, the dynamic liquid wetting behavior is determined solely by surface topography. In our system, the metal was coated on one side of the deformed SMP pillars as evident from the shadowing effect shown in the left inset of Figure 4.12b. Once the triple phase line reached the tips of the tilted pillars, it would

be pinned both at the bottom of the shadowed area and on the tips of the partially coated pillars (see schematic and optical image in Figure 4.12c middle panel). In the opposite direction, the rim of the spreading liquid front can make preferential contact with the pillar tip and propagate downward along the coated surface, making it much easier to spread as shown on the right panel of Figure 4.11c.

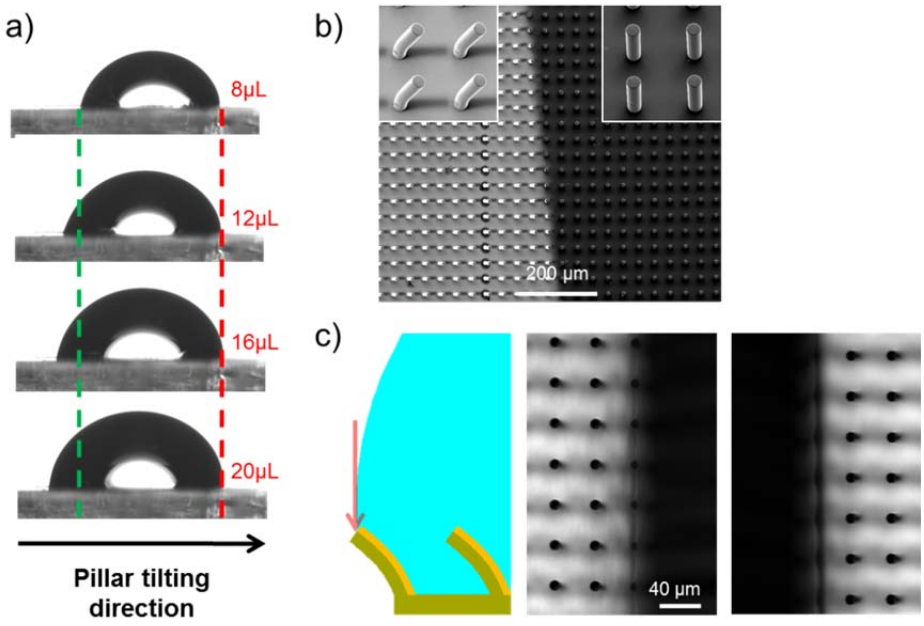

Figure 4.12 Anisotropic water spreading on gold-coated, tilted SMP pillars (sample 5). (a) A series of optical images of anisotropic liquid spreading (to the left) on the partially recovered SMP pillar (Au thickness ~ 22.8 nm, tilting angle θ ~ 19.8°). The water volumetric increment is ~ 4 μL. (b) SEM images of the SMP pillar arrays with (left) and without (right) gold coating, showing the shadowed region under the partially recovered SMP pillars. (c) Schematic of the triple phase line pinned on the tilted pillars. Red arrow indicates the pinning location on the pillar tip (left); optical images of the pinned triple phase line on the tilted pillars in the tilting direction (middle) and the reverse direction (right).

4.6 Conclusions

Using HAR SMP pillar arrays, we demonstrated that uniform patterns and hierarchical structures could be fabricated with one-step controlled deformation. We

showed distinctly different wettability on the deformed pillars vs. the original/recovered ones. While the latter exhibited Cassie-Baxter non-wettable state with sliding angle ranging from 7.5° to 69°, the deformed structures were best described by the Wenzel model, where the water droplets were fully pinned on the tilted pillars. These properties can be potentially applied to reconfigurable water collection or microfluidics. Furthermore, the SMP pillars can act as sticky fingers to selectively pick up and transfer colloidal nanoparticles on different parts of the pillars, either on the tips or the sidewalls. Further, by coating the deformed SMP pillars with a thin layer of metal**,** including gold and gold-palladium alloy, we were able to manipulate the recovery of SMP pillars and precisely control the degree of tilting by varying the metal layer thickness. This tilting was a consequence of the competition between the SMP pillars that favored the original straight state and the metal layers that preferred the bent state. With this selective coating of a metal layer on the tilted pillars, a unique anisotropic liquid spreading behavior was observed, where the water droplet was fully pinned in the direction of tilting but advanced in the reverse direction. This phenomenon is explained by the interplay of the surface chemistry and topography. We believe that this versatile deformation patterning techniques can not only be applied to surface wettability but other applications such as optics, plasmonics and dry adhesives. This patterning method can also be extended to other SMP systems as an easy and effective way to fabricate complex homogeneous or heterogeneous structures.

4.7 Reference

1. N. J. Glassmaker, A. Jagota, C. Y. Hui and J. Kim, *J. R. Soc. Interface*, 2004, **1**, 23-33.

2. P. Roca-Cusachs, F. Rico, E. Martinez, J. Toset, R. Farre and D. Navajas, *Langmuir*, 2005, **21**, 5542-5548.

3. D. Chandra and S. Yang, *Acc. Chem. Res.*, 2010, **43**, 1080-1091.

4. C. Y. Hui, A. Jagota, Y. Y. Lin and E. J. Kramer, *Langmuir*, 2002, **18**, 1394-1407.

5. S. J. Gerbode, J. R. Puzey, A. G. McCormick and L. Mahadevan, *Science*, 2012, **337**, 1087-1091.

6. T. Eisner and D. J. Aneshansley, *Proc. Natl. Acad. Sci. U. S. A.*, 2000, **97**, 6568-6573.

7. R. Ruibal and V. Ernst, *J. Morphol.*, 1965, **117**, 271-293.

8. T. Savin, N. A. Kurpios, A. E. Shyer, P. Florescu, H. Y. Liang, L. Mahadevan and C. J. Tabin, *Nature*, 2011, **476**, 57-62.

9. Y. Tian, N. Pesika, H. B. Zeng, K. Rosenberg, B. X. Zhao, P. McGuiggan, K. Autumn and J. Israelachvili, *Proc. Natl. Acad. Sci. U. S. A.*, 2006, **103**, 19320-19325.

10. Y. Zhang, E. A. Matsumoto, A. Peter, P. C. Lin, R. D. Kamien and S. Yang, *Nano Lett.*, 2008, **8**, 1192-1196.

11. X. L. Zhu, Y. Zhang, D. Chandra, S. C. Cheng, J. M. Kikkawa and S. Yang, *Appl. Phys. Lett.*, 2008, **93**, 161911.

12. J. H. Jang, C. Y. Koh, K. Bertoldi, M. C. Boyce and E. L. Thomas, *Nano Lett.*, 2009, **9**, 2113-2119.

13. K. Bertoldi, P. M. Reis, S. Willshaw and T. Mullin, *Adv. Mater.*, 2010, **22**, 361-366.

14. B. D. Gates, Q. B. Xu, V. R. Thalladi, T. B. Cao, T. Knickerbocker and G. M. Whitesides, *Angew. Chem.-Int. Edit.*, 2004, **43**, 2780-2783.

15. Q. B. Xu, B. D. Gates and G. M. Whitesides, *J. Am. Chem. Soc.*, 2004, **126**, 1332-1333.

16. Q. B. Xu, J. M. Bao, R. M. Rioux, R. Perez-Castillejos, F. Capasso and G. M. Whitesides, *Nano Lett.*, 2007, **7**, 2800-2805.

17. B. Pokroy, A. K. Epstein, M. C. M. Persson-Gulda and J. Aizenberg, *Adv. Mater.*, 2009, **21**, 463-469.

18. S. H. Kang, B. Pokroy, L. Mahadevan and J. Aizenberg, *ACS Nano*, 2010, **4**, 6323-6331.

19. B. Pokroy, S. H. Kang, L. Mahadevan and J. Aizenberg, *Science*, 2009, **323**, 237-240.

20. H. G. Duan, J. K. W. Yang and K. K. Berggren, *Small*, 2011, **7**, 2661-2668.

21. P.-G. de Gennes, F. Brochard-Wyart and D. Quéré, *Capillarity and wetting phenomena : drops, bubbles, pearls, waves*, Springer, New York, 2004.

22. W. Barthlott and C. Neinhuis, *Planta*, 1997, **202**, 1-8.

23. A. Lafuma and D. Quere, *Nat. Mater.*, 2003, **2**, 457-460.

24. A. Tuteja, W. Choi, M. L. Ma, J. M. Mabry, S. A. Mazzella, G. C. Rutledge, G. H. McKinley and R. E. Cohen, *Science*, 2007, **318**, 1618-1622.

25. A. Tuteja, W. Choi, J. M. Mabry, G. H. McKinley and R. E. Cohen, *Proc. Natl. Acad. Sci. U. S. A.*, 2008, **105**, 18200-18205.

26. X. Deng, L. Mammen, H. J. Butt and D. Vollmer, *Science*, 2012, **335**, 67-70.

27. F. De Angelis, F. Gentile, F. Mecarini, G. Das, M. Moretti, P. Candeloro, M. L. Coluccio, G. Cojoc, A. Accardo, C. Liberale, R. P. Zaccaria, G. Perozziello, L. Tirinato, A. Toma, G. Cuda, R. Cingolani and E. Di Fabrizio, *Nat. Photonics*, 2011, **5**, 683-688.

28. A. K. Kota, G. Kwon, W. Choi, J. M. Mabry and A. Tuteja, *Nat. Commun.*, 2012, **3**, 1025.

29. K. M. Wisdom, J. A. Watson, X. Qu, F. Liu, G. S. Watson and C.-H. Chen, *Proc. Natl. Acad. Sci. U. S. A.*, 2013, **110**, 7992-7997.

30. C. Sun, Z. Z. Gu and H. Xu, *Langmuir*, 2009, **25**, 12439-12443.

31. S. S. Chhatre, W. Choi, A. Tuteja, K. C. Park, J. M. Mabry, G. H. McKinley and R. E. Cohen, *Langmuir*, 2010, **26**, 4027-4035.

32. R. J. Vrancken, M. L. Blow, H. Kusumaatmaja, K. Hermans, A. M. Prenen, C. W. M. Bastiaansen, D. J. Broer and J. M. Yeomans, *Soft Matter*, 2013, **9**, 674-683.

33. C. Q. Lai, C. V. Thompson and W. K. Choi, *Langmuir*, 2012, **28**, 11048-11055.

34. N. Obara and K. Okumura, *Phys. Rev. E*, 2012, **86**, 020601.

35. D. Y. Xia, L. M. Johnson and G. P. Lopez, *Adv. Mater.*, 2012, **24**, 1287-1302.

36. J. Y. Chung, J. P. Youngblood and C. M. Stafford, *Soft Matter*, 2007, **3**, 1163-1169.

37. K. Khare, J. H. Zhou and S. Yang, *Langmuir*, 2009, **25**, 12794-12799.

38. P. C. Lin and S. Yang, *Soft Matter*, 2009, **5**, 1011-1018.

39. T. I. Kim and K. Y. Suh, *Soft Matter*, 2009, **5**, 4131-4135.

40. K. H. Chu, R. Xiao and E. N. Wang, *Nat. Mater.*, 2010, **9**, 413-417.

41. C.-M. Chen, C.-L. Chiang, C.-L. Lai, T. Xie and S. Yang, *Adv. Funct. Mater.*, 2013, In Press. DOI:10.1002/adfm.201300052.

42. W. Small, P. Singhal, T. S. Wilson and D. J. Maitland, *J. Mater. Chem.*, 2010, **20**, 3356-3366.

43. J. Kunzelman, T. Chung, P. T. Mather and C. Weder, *J. Mater. Chem.*, 2008, **18**, 1082-1086.

44. J. Li, J. M. Shim, J. Deng, J. T. B. Overvelde, X. L. Zhu, K. Bertoldi and S. Yang, *Soft Matter*, 2012, **8**, 10322-10328.

45. T. Xie, X. C. Xiao, J. J. Li and R. M. Wang, *Adv. Mater.*, 2010, **22**, 4390-4394.

46. H. Xu, C. Yu, S. Wang, V. Malyarchuk, T. Xie and J. A. Rogers, *Adv. Funct. Mater.*, 2013, In press. DOI:10.1002/adfm.201203396.

47. Z. Wang, C. Hansen, Q. Ge, S. H. Maruf, D. U. Ahn, H. J. Qi and Y. F. Ding, *Adv. Mater.*, 2011, **23**, 3669-3673.

48. S. Reddy, E. Arzt and A. del Campo, *Adv. Mater.*, 2007, **19**, 3833-3837.

49. S. Kim, M. Sitti, T. Xie and X. C. Xia, *Soft Matter*, 2009, **5**, 3689-3693.

50. T. Xie and X. C. Xiao, *Chem. Mater.*, 2008, **20**, 2866-2868.

51. C. Liu, H. Qin and P. T. Mather, *J. Mater. Chem.*, 2007, **17**, 1543-1558.

52. A. Lendlein and S. Kelch, *Angew. Chem.-Int. Edit.*, 2002, **41**, 2034-2057.

53. T. Xie, *Polymer*, 2011, **52**, 4985-5000.

54. C. M. Yakacki, S. Willis, C. Luders and K. Gall, *Adv. Eng. Mater.*, 2008, **10**, 112-119.

55. H. J. Qi, T. D. Nguyen, F. Castroa, C. M. Yakacki and R. ShandaSa, *J. Mech. Phys. Solids*, 2008, **56**, 1730-1751.

56. V. Srivastava, S. A. Chester and L. Anand, *J. Mech. Phys. Solids*, 2010, **58**, 1100-1124.

57. B. A. Nelson, W. P. King and K. Gall, *Appl. Phys. Lett.*, 2005, **86**, 103108.

58. Y. M. Zheng, X. F. Gao and L. Jiang, *Soft Matter*, 2007, **3**, 178-182.

59. C. W. Wu, X. Q. Kong and D. Wu, *Phys. Rev. E*, 2007, **76**, 017301.

60. A. B. D. Cassie and S. Baxter, *Trans. Faraday Soc.*, 1944, **40**, 546-551.

61. A. J. B. Milne and A. Amirfazli, *Adv. Colloid Interface Sci.*, 2012, **170**, 48-55.

62. R. N. Wenzel, *Ind. Eng. Chem.*, 1936, **28**, 988-994.

63. C. J. Lv, C. W. Yang, P. F. Hao, F. He and Q. S. Zheng, *Langmuir*, 2010, **26**, 8704-8708.

64. P. Jiang and M. J. McFarland, *J. Am. Chem. Soc.*, 2004, **126**, 13778-13786.

65. J. H. Moon and S. Yang, *Chem. Rev.*, 2010, **110**, 547-574.

66. S. Wong, V. Kitaev and G. A. Ozin, *J. Am. Chem. Soc.*, 2003, **125**, 15589-15598.

67. C. B. Murray, C. R. Kagan and M. G. Bawendi, *Science*, 1995, **270**, 1335-1338.

68. R. Mayoral, J. Requena, J. S. Moya, C. Lopez, A. Cintas, H. Miguez, F. Meseguer, L. Vazquez, M. Holgado and A. Blanco, *Adv. Mater.*, 1997, **9**, 257-260.

69. P. Jiang, J. F. Bertone, K. S. Hwang and V. L. Colvin, *Chem. Mater.*, 1999, **11**, 2132-2140.

70. A. Mihi, M. Ocana and H. Miguez, *Adv. Mater.*, 2006, **18**, 2244-2249.

71. X. Yan, J. M. Yao, G. A. Lu, X. Chen, K. Zhang and B. Yang, *J. Am. Chem. Soc.*, 2004, **126**, 10510-10511.

72. J. M. Yao, X. Yan, G. Lu, K. Zhang, X. Chen, L. Jiang and B. Yang, *Adv. Mater.*, 2004, **16**, 81-84.

73. J. H. Zhang, Y. F. Li, X. M. Zhang and B. Yang, *Adv. Mater.*, 2010, **22**, 4249-4269.

74. M. D. McConnell, A. W. Bassani, S. Yang and R. J. Composto, *Langmuir*, 2009, **25**, 11014-11020.

75. L. C. Gao and T. J. McCarthy, *Langmuir*, 2006, **22**, 2966-2967.

76. N. J. Shirtcliffe, G. McHale, M. I. Newton, G. Chabrol and C. C. Perry, *Adv. Mater.*, 2004, **16**, 1929-1932.

77. R. G. Karunakaran, C. H. Lu, Z. H. Zhang and S. Yang, *Langmuir*, 2011, **27**, 4594-4602.

78. J. Li, G. Q. Liang, X. L. Zhu and S. Yang, *Adv. Funct. Mater.*, 2012, **22**, 2980-2986.

79. M. K. Kwak, H. E. Jeong, T. I. Kim, H. Yoon and K. Y. Suh, *Soft Matter*, 2010, **6**, 1849-1857.

80. M. Ohring, *The materials science of thin films*, Academic Press, Boston, 1992.

81. N. A. Malvadkar, M. J. Hancock, K. Sekeroglu, W. J. Dressick and M. C. Demirel, *Nat. Mater.*, 2010, **9**, 1023-1028.

Chapter 5

Summary and Outlook

5.1 Summary

In this dissertation we studied the mechanical instability and large deformation of structured soft material to tune surface properties. On a low aspect ratio channel-type surface structure, we investigated the alignment of wrinkle morphology in the presence of these surface patterns on a photoresist with depth-wise gradient crosslinking density. Using high aspect ratio shape memory polymer (SMP) pillar arrays, we designed a dry adhesive based on mechanical interlocking if buckled pillars to gain strong jointing force whose magnitude can be tuned by geometry and temperature. We fine-tuned the deformation/recovery behaviors of SMP pillars as a reconfigurable surface for manipulation of wettability and its anisotropy, as well as sticky fingers to grab nanoparticles for fabrication of hierarchical structures.

We started our investigation from the size effect of low aspect ratio 1-D patterns on the thin film wrinkling instability. We developed a new wrinkling system based on dyed SU-8 photoresist, which formed a gradient crosslinking density UV exposure. By combining thermoplasticity and photopatternability of SU-8, we investigated physical confinement of wrinkling using the 1-D pre-patterns. The size ratio of the pre-patterns to the intrinsic wrinkles (r_p: pre-pattern pitch to wrinkle wavelength; r_h: pre-pattern height to wrinkle amplitude) was carefully chosen so that both r_p and r_h lied in the order of ~ 0.1-10. At r_p ~ 10, it was found that the wrinkles remained anisotropic but confined, primary on the mountain region of the SU-8 pre-pattern. By lowering r_p to ~ 1, the

wrinkles were fully confined to form 1-D bumps with out-of-phase alignment to the neighboring mountain regions. At the smallest $r_p \sim 0.1$, the wrinkle morphology was found highly sensitive to r_h. For r_h on the order of ~ 1, the wrinkle aligned perpendicularly to the pre-patterns, showing a long-range and in-phase order. Decreasing r_h to ~ 0.1 led to dual-orientational alignment, with one set of wrinkling still grow perpendicularly to the pre-patterns, the other set of high amplitude localized fold form in parallel to the pre-patterns. Further decreasing r_h recovers the isotropic wrinkles. We constructed a morphological diagram based on these findings, which should pave the way to fully control wrinkles via design of the surface pre-patterns.

Separately, we studied the instability and large deformation of high aspect ratio pillar arrays. In particular, we designed a new dry adhesive, whose adhesion force originated from interlocking of mutually buckled pillar arrays (hexagonal array, 1μm diameter, 1 μm spacing and aspect ratio 4) under a load. We used thermally activated SMP, whose Young's modulus could be greatly reduced by three orders of magnitude from room temperature to 80 °C, above its glass transition temperature. The tunable mechanical strength endowed low buckling threshold and easy adhesive engagement at 80 °C but high stiffness and high adhesion force after engagement by cooling the pillars back to the room temperature. Microscopically, we found that the pillars mainly interweaved with each other with some contribution to the adhesion strength from pillar indentation to each other. The latter is similar to the gecko-like fibrillar contact, whose effective adhesion is shown experimentally and theoretically to be lower than the interweaving state. A Moiré pattern was revealed as a result of periodic contact and misalignment between two pillar arrays. The total pillar-to-pillar adhesion force reached

~ 54 N/cm^2 and ~ 72 N/cm^2 in normal and shear direction, respectively, much higher than the pillar-to-flat (~ 12 N/cm^2 in normal and ~ 15 N/cm^2 in shear) and flat-to-flat (~ 7 N/cm^2 in normal and ~ 16 N/cm^2 in shear) counterparts. We further showed that the adhesion anisotropy ψ, defined as the ratio of shear to normal adhesion force, can be tuned by changing the pillar spacing, going from ~ 1.3 dramatically to ~ 5.4 as the spacing doubled. Despite of the strong adhesive force obtained at room temperature after engagement, the adhesive could be effortlessly separated on demand by reheating back to 80 °C.

Under the applied preload with complex pillar-pillar interaction and prolonged heating under deformation, the SMP pillars could not be recovered to the original shapes. However, the SMP pillars were fully recoverable under uniform shearing and collapsing. We utilized this behavior to create a reconfigurable surface for wettability control and advanced patterning. Specifically, the original/recovered pillars exhibited Cassie wetting state with a high droplet contact angle and low sliding angle. The fully deformed surfaces, on the other hand, displayed Wenzel wetting state, where the droplet was fully pinned with anisotropic droplet shape at large pillar spacing. We demonstrated that such high wetting contrast can be employed for liquid collection. We also applied the original or deformed pillars to pick up nanoparticles on to a selected location of pillars (top vs. the side walls) as a facile method to fabricate hierarchical structures. Moreover, we showed that it was possible to precisely control SMP deformation by depositing a thin metal layer onto the deformed structures, limiting the SMP pillars from full recovery. This allowed us to access SMP pillars at different tilting angle with high precision. More intriguingly,

the tilted composite structure possessed a unique unidirectional liquid propagation opposite to the pillar tilting direction.

5.2 Outlook

This thesis demonstrated novel approaches to harness mechanical instability and large deformation, providing important physical insight for the mechanistic understanding of pattern-instability interaction and tailoring instabilities and deformation to surface properties and applications. The extension of our studies can bring in advanced surface control and applications to soft material systems.

We showed in Chapter 2 that 1-D surface pre-patterns alone were able to transform isotropic wrinkle morphology to a rich library of alignments by adjusting the pre-pattern size relative to the intrinsic wrinkle dimensions. However, there is little knowledge regarding the size effect of 2-D pre-patterns on isotropic wrinkles, especially those with feature size smaller than the wrinkle dimensions (wavelength and amplitude). Prior studies showed that 2-D array of bumps were able to induce wrinkle ordering with comparable periodicity.[1] It will be interesting to vary the pattern size, shape and lattice symmetry of 1-D and 2-D pre-patterns systematically for a full control of wrinkle morphology and size. Here our photoresist based wrinkling system is an ideal platform for this purpose. We only demonstrate the patterning by capillary force lithography. As a photoresist, the dyed SU-8 can be directly photo-patterned using photolithography, which will create patterns with chemical contrast of different crosslinking density in selected regions. Our preliminary results showed that not only the wrinkles could be confined in this manner but other types of mechanical instability, such as delamination, could also be guided. We believe that the wrinkle in a graded thin film system together with

photopatterning may be applicable to fabricate complex patterns for dynamic tuning of optical properties and wettability.

In the SMP pillar system, we have developed a new type of buckling-based dry adhesive, showing strong adhesion force by pillar interweaving and indenting. In our investigation, we explored the adhesion property as a function of the pillar spacing (2 versus 3 μm), pillar length scale (1 versus 10 μm in diameter) and operating temperature (room temperature versus 80 °C). Other geometrical parameters such as pillar aspect ratio, pillar and tip shape could also be changed to probe the optimal adhesion force. As the pillar aspect ratio is increased, the possibility that the pillars interweave with each other is expected to increase if the spacing is held constant. At the same time, such surface is more vulnerable to instability-induced collapse even before engagement. A balance between these two factors should thus be considered in search for the ideal aspect ratio. While it is impossible to examine the adhesion force of all possible geometries, one can borrow the attachment concepts from biological systems as a starting guideline.[2] For example, it is shown that conical shape structures, mimicking the head arrester on the dragonflies, can be utilized as friction based adhesive. Such system, however, suffers from low adhesion force to preload ratio.[3] This problem can potentially be solved by adapting our SMP system which can be softened before engagement to greatly reduce the required preload. It is also intriguing to investigate how interweaving and indenting contact would play the roles in such device. Furthermore, as mentioned in Chapter 3, the shape memory polymer pillars were not recoverable after engaging as an adhesive. In principle, the shape recovery property can be tailored by optimizing the deformation/recovery temperature[4] or preload time under the same chemical

formulation.[5] Alternatively, shape memory polymers capable of withstanding extreme strain condition can also be employed.[6]

In our study, we changed the geometry to stabilize the pillar recovery for wettability manipulation and patterning, as shown in Chapter 4. We demonstrated that the static contact angle and the sliding angle can be controlled simply by deforming and recovering the SMP pillar arrays. At the same time, anisotropic droplet shape was observed for large spacing patterns. In this aspect, it is interesting to investigate how the orientation of deformation, which is always fixed to the lattice vector direction in our study, would impact the shape of the droplet. Especially, we mentioned that for smaller spacing patterns, saw-tooth exists as the pillar overlaps where the droplets atop are circular in shape. Conversely, if the SMP pillars are deformed along the diagonal or other orientation, where the spacing along the chosen direction is larger than the pillar height, the deformed pillars should also form channel-like structures, inducing the formation of anisotropic droplet. Varying the deformation direction can thus control the morphology of the droplet. On the other hand, the anisotropic liquid spreading behavior on metal-tilted SMP pillars deserves a systematic study, exploring the spreading speed, droplet retention force and spreading dynamics as a function of tilting angle and comparing to existing systems.[7, 8] Lastly, while the hierarchical structures were fabricated by selective picking up of silica nanoparticles onto the SMP, there are a variety of particles of different size,[9, 10] type[9, 11, 12] and shape[12] can be used, which could lead to novel wetting and optical properties.

5.3 References

1. T. Ohzono, H. Watanabe, R. Vendamme, C. Kamaga, T. Kunitake, T. Ishihara and M. Shimomura, *Adv. Mater.*, 2007, **19**, 3229-3232.
2. S. N. Gorb, *Philos. Trans. R. Soc. A-Math. Phys. Eng. Sci.*, 2008, **366**, 1557-1574.
3. S. N. Gorb and V. L. Popov, *Philos. Trans. R. Soc. Lond. Ser. A-Math. Phys. Eng. Sci.*, 2002, **360**, 211-225.
4. C. M. Yakacki, S. Willis, C. Luders and K. Gall, *Adv. Eng. Mater.*, 2008, **10**, 112-119.
5. K. Dasharathi and J. A. Shaw, Behavior and Mechanics of Multifunctional Materials and Composites 2013, San Diego, California, United States, 2013.
6. W. Voit, T. Ware, R. R. Dasari, P. Smith, L. Danz, D. Simon, S. Barlow, S. R. Marder and K. Gall, *Adv. Funct. Mater.*, 2010, **20**, 162-171.
7. T. I. Kim and K. Y. Suh, *Soft Matter*, 2009, **5**, 4131-4135.
8. K. H. Chu, R. Xiao and E. N. Wang, *Nat. Mater.*, 2010, **9**, 413-417.
9. A. Mihi, M. Ocana and H. Miguez, *Adv. Mater.*, 2006, **18**, 2244-2249.
10. P. Jiang and M. J. McFarland, *J. Am. Chem. Soc.*, 2004, **126**, 13778-13786.
11. C. B. Murray, C. R. Kagan and M. G. Bawendi, *Science*, 1995, **270**, 1335-1338.
12. J. A. Champion, Y. K. Katare and S. Mitragotri, *Proc. Natl. Acad. Sci. U. S. A.*, 2007, **104**, 11901-11904.

Appendix A

List of Publications

1. **Chen C.-M.**, and Yang S., "Wrinkling Instabilities in Polymer Films and their Applications", *Polymer International*, 2012, 61, 1041-1047
2. Zhu X., Wu G., Dong R., **Chen C.-M.**, and Yang S., "Capillarity induced instability in responsive hydrogel membranes with periodic hole array", Soft Matter, 2012, 8, 8088-8093
3. Hsieh W.-T., Hsu C.-J., Capraro B. R., Wu T., **Chen C.-M.**, Yang S., and Tobias Baumgart, "Curvature Sorting of Peripheral Proteins on Solid-Supported Wavy Membranes", Langmuir, 2012, 28, 12838-12843
4. **Chen C.-M.**, Chiang C.-L., Lai C.-L., Xie T., and Yang S., "Buckling-based strong dry adhesives", Advanced Functional Materials, in press, DOI: 10.1002/adfm.201300052
5. **Chen C.-M.**, Reed J. C, and Yang S., "Guided wrinkling in osmotic swollen, pre-patterned photoresist thin films", Soft Matter, in revision
6. **Chen C.-M.** and Yang S., "Directed water shedding on high aspect ratio shape memory polymer micropillar arrays", submitted